TECHNISCHE UNIVERSITÄT MÜNCHEN

Friedrich-Schiedel Institut für Neurowissenschaften

Dendritic organization of sensory inputs in cortical neurons *in vivo*

Hongbo Jia

Vollständiger Abdruck der von der Fakultät für Medizin der Technischen Universität München zur Erlangung des akademischen Grades eines

Doctor of Philosophy (Ph.D.)

genehmigten Dissertation.

Vorsitzender: Univ.-Prof. Dr. Thomas Misgeld

Prüfer der Dissertation:

1. Univ.-Prof. Dr. Arthur Konnerth

2. Prof. Dr. Bert Sakmann

Die Dissertation wurde am 09.08.2011 bei der Fakultät für Medizin der Technischen Universität München eingereicht und durch die Fakultät für Medizin am 02.11.2011 angenommen.

Abstract

Mammalian cortical neurons compute sensory information that arrives through numerous synaptic inputs located on their dendrites. These inputs are essential for various computational functions of neurons. However, it has long been a major challenge to identify sensory stimulation-activated individual synaptic inputs in cortical neurons *in vivo*. I have implemented and applied the combined method of two-photon calcium imaging and whole-cell patch-clamp recording to study layer 2/3 cortical neurons in mouse visual cortex and identified orientation-specific dendritic input sites for the first time. When the neuron was slightly hyperpolarized just below action potential firing threshold, multiple dendritic calcium hotspots could be observed upon visual stimulation of a given orientation. These hotspots were spatially restricted to small dendritic domains and sensitive to NMDA receptor antagonist, thus representing sensory evoked synaptic input sites. An important finding was that input sites with different orientation preference were intermingled throughout the dendritic tree. Furthermore, all neurons received multiple inputs of different orientation preferences, regardless whether the action potential output had a specific preference or not.

Overall, I have established the combined method of *in vivo* whole-cell recording and two-photon calcium imaging and implemented efficient data analysis algorithms for studying sensory evoked dendritic inputs in mammalian cortical neurons *in vivo*. Articles involving these major findings have been published or accepted by peer-reviewed journals. As a result, this dissertation is composed of the accumulation of related articles together with brief summary and specification of personal contributions.

Table of Contents

Personal considerations

As one of the 80s' generation, I have always been fascinated by the intelligent robots that appeared in Hollywood movies like Star Wars, Terminator, etc. But in reality, would it possible to build such machines?

In fact the key issue is not how to build a self-moving robot, but rather, what is intelligence? If we (=humans) acknowledge that the creation of steam engines was based on the knowledge of physics, we can as well say that the creation of intelligent robots should be based on the knowledge of brain. Apparently our knowledge of physics is quite advanced at the moment, and in fact has greatly helped the understanding of brain. However, our knowledge of brain, fairly speaking, is still quite modest. In contrast to the systematic theories of physics, theories of neuroscience, although numerous, were rather like scattered stars in the sky. The main problem was the fact that each measurement of brain could only acquire very little information from all that a brain holds, typically, recording from 1 to 10^3 neurons out of total 10^6 to 10^{12} in animals that are considered to be "intelligent".

However, thanks to the development of electronic computers, we can simulate more number of neurons than that we could record from a real brain. But have that created intelligence? Unfortunately, not yet. Perhaps what matters more are not the numbers, but something else, for example, rules. What rules then? Conventional intuition of rules, as well as classical physics, tells us that everything should be exactly predicted by the rules, well, not really like living animals would normally behave.

No worries, physics also tells us that even simple and fixed rules can generate complex and unpredictable behaviors, i.e., the "chaos". But do not yet draw equality between "intelligence" and "chaos", since we have not known what the specific underlying rules are. What we can do is to try our best to get as much information as possible from measurements of brain, and then think on mathematical rules that would describe them properly. Such rules must be consistent with each other, and more importantly, also consistent with existing rules of physics. Only by doing so would allow us to "create" intelligence *ab initio* on a machine instead of "simulate" intelligence with a machine. The difference is that, if we leave that machine alone,

whether it remains intelligent or not.

So, it is clear that we must now focus on measuring the brain. What should we measure then, weight, color, or shape? Apparently we know that these properties do not have much to do with intelligence. Electricity is the answer, or at least, the belief of most neuroscientists. Electricity can be measured from objects at various scales depending on where and how the electrodes are placed: the whole brain, or a small volume of brain, a bunch of cells, a single cell, or a part of a cell.

Actually one of the most basic and famous measurements were just about a few protein molecules which could let ions flow through membranes of neurons. Unfortunately, such measurements cannot be performed in a living brain because the molecules to be measured must be isolated from the rest of their host cell and the brain. Nevertheless, the results of these measurements formed the ground level rules that support the other rules which would be concluded from measurements of larger objects.

Therefore we go one level up, to the parts of a cell. Is it possible to simultaneously measure different parts of a cell in a living animal's brain without isolating them from the brain? As I present in this dissertation, yes. But I used a different measurement method, that the fine processes of the cell were measured by fluorescence indicators for a fraction of Ca^{2+} ions. However, thanks to the ground level rules we were able to use these fluorescence signals to represent specific electrical activities.

One may ask, why not measure at the other scales? The straightforward answer is that, other people had done many measurements at those scales, while my advisor needed to get me something new to do so that I could get food in the future if I would still work on neuroscience. However, what I have begun to understand later on after my measurements was that, measuring parts of a cell is not only measuring for this cell, but simultaneously measuring some other cells who connects to this cell at the measured locations.

Connectivity, especially long-range connectivity is one of the most important features of brain. As a contrast, cells in other organs interact mostly with their nearest neighbours. The enormous amount of interconnections in a brain made it almost impossible to capture all of

them, but we now have a simple scenario: one node of the network with a fraction of connections to that node. We could study how this single node of network represents the external physical world and/or other parts of the neuronal network that are related to it, which was my little contribution to the entire human knowledge of brain.

For most time of my dissertation research, I built measurement machines, measured a few neurons in mice brains and reported the results by electronic computers. Thanks to the new rules of the graduate school, I would not spend much time in re-organizing my old knowledge that had already been published in peer-reviewed journals. I will organize the entire papers (permissions have been acquired) in individual chapters, provide brief introduction to the background of each study, and then give general overview and summary chapters. The time being saved in this way can be then used for further experimental works on the neuronal organization of brain as well as thinking on a physical theory of describing brain function, which perhaps can eventually lead to realization of the dream of creating intelligent machines.

Hongbo Jia

22/07/2011 at Munich

1 Overview: Dendritic mapping of sensory inputs *in vivo*

As a canonical viewpoint of neuroscience, brain function relies on the network of synaptically interconnected neurons. Neurons of the mammalian brain communicate with each other mostly though chemical synapses. Excitatory synapses using glutamate as a transmitter form many of their contacts with fine dendritic protrusions, the so-called spines (1). In the cortex, for example, single pyramidal neurons receive thousands of synaptic inputs on such spines (2). An understanding of the dendritic organization of the synaptic inputs is important because of the great potential of signal integration and computation (3, 4). In recent years there had been substantial progress in our understanding of the local connectivity in selected brain regions (5-7). However, despite many years of detailed anatomical studies (8) and more recent efforts of revealing the brain's connectome (9), the functional organization of the synaptic connectivity *in vivo*, in relation to defined sensory stimuli, is still largely unknown. One important question, for example, is how are sensory stimulation activated dendritic input sites organized in single cortical neurons *in vivo* (10).

One common way of studying synaptic function in dendrites consists in the analysis of postsynaptic signals, for example the calcium transients induced by synaptic activity (11). Such studies under *in vitro* conditions were usually performed by imaging with fluorescent calcium indicators near the site of focal extracellular synaptic stimulation (12). However, for mammalian cortical neurons, the anatomical knowledge acquired from brain slices has not yet been sufficient to determine *a priori* which input sites would actually be activated by given sensory stimulation under *in vivo* condition. Therefore, in order to be able to identify the stimulation activated synaptic calcium signaling sites *in vivo*, one challenge was to simultaneously image as many dendrites as possible while having sufficient temporal resolution to resolve calcium transients. Yet another difficulty came after that sensory stimuli are likely to trigger action potential firing. Action potentials are back-propagated to dendrites in widespread manner (13, 14), interact with synaptic activity and result in compound calcium signals (15). Although it was possible to correlate the compound dendritic signals with sensory stimuli in lower vertebrates (16), such analysis had not yet been unambiguously established for mammalian cortical neurons *in vivo*. In contrast, for some specific type of non-spiking neurons (17-19) it was feasible to

directly map dendritic calcium signals to specific sensory stimuli. Therefore, the prevention of action potential firing is important for the revelation of sensory activated synaptic calcium signaling sites in cortical neurons *in vivo*.

To overcome these challenges for identifying sensory stimuli activated dendritic input sites in cortical neurons, I have employed the combined method of whole-cell recording and rapid full-frame two-photon calcium imaging. Whole-cell recording could provide efficient hyperpolarization to prevent action potential firing, while rapid full-frame scanning allowed simultaneous imaging of multiple dendrites in the focal plane. Furthermore, significant improvements in experimental procedures (20) enabled long-lasting recording of sensory evoked local dendritic calcium signals in mammalian cortical neurons *in vivo*. With these advantages, this method had enabled the mapping of visual stimulation evoked dendritic input sites in layer 2/3 neurons of mouse primary visual cortex (21).

Furthermore, the combined method of *in vivo* whole-cell recording and two-photon calcium imaging has been applied in subsequent experimental studies in the auditory cortex and barrel cortex (22, 23). The basic numerical analysis tools which were developed during the first study were also applied in these studies. Specifically, for the dendritic mapping of individual whiskers in barrel cortex (chapter 4), an automatic pattern recognition algorithm was employed that successfully distinguished the dendritic activation patterns of different whiskers for each single trial at high accuracy. In combination, a theoretical model was also devised to verify the analysis on experimental data.

In the next chapters, the published research articles for which I had significant contributions will be presented with brief background introductions respectively. Besides, since calcium imaging alone is a widely applied method to study brain function and disease, a literature review on calcium imaging will be also attached. Additionally, the technical features of the two-photon microscopy setup on which the experiments had been performed will be demonstrated. Finally, I will specify my personal contributions in the related published/accepted articles.

References

1. Purves, D., Augustine, G. J., Fitzpatrick, D., Hall, W. C., LaMantia, A.-S., McNamara, J. O., & White, L. E. (2008) *Neuroscience* (Sinauer Associates).
2. Ballesteros-Yanez, I., Benavides-Piccione, R., Elston, G. N., Yuste, R., & DeFelipe, J. (2006) Density and morphology of dendritic spines in mouse neocortex. *Neuroscience* **138,** 403-409.
3. Silver, R. A. (2010) Neuronal arithmetic. *Nature reviews* **11,** 474-489.
4. Branco, T. & Hausser, M. (2010) The single dendritic branch as a fundamental functional unit in the nervous system. *Current opinion in neurobiology* **20,** 494-502.
5. Katz, L. C. & Dalva, M. B. (1994) Scanning laser photostimulation: a new approach for analyzing brain circuits. *Journal of neuroscience methods* **54,** 205-218.
6. Nikolenko, V., Poskanzer, K. E., & Yuste, R. (2007) Two-photon photostimulation and imaging of neural circuits. *Nature methods* **4,** 943-950.
7. Petreanu, L., Mao, T., Sternson, S. M., & Svoboda, K. (2009) The subcellular organization of neocortical excitatory connections. *Nature* **457,** 1142-1145.
8. Cajal, S. R. y. (1995) *Histology of the Nervous System of Man and Vertebrates* (Oxford University Press).
9. Lichtman, J. W., Livet, J., & Sanes, J. R. (2008) A technicolour approach to the connectome. *Nature reviews* **9,** 417-422.
10. Priebe, N. J. & Ferster, D. (2010) Neuroscience: Each synapse to its own. *Nature* **464,** 1290-1291.
11. Sabatini, B. L., Maravall, M., & Svoboda, K. (2001) Ca(2+) signaling in dendritic spines. *Current opinion in neurobiology* **11,** 349-356.
12. Yuste, R. & Denk, W. (1995) Dendritic spines as basic functional units of neuronal integration. *Nature* **375,** 682-684.
13. Helmchen, F., Svoboda, K., Denk, W., & Tank, D. W. (1999) In vivo dendritic calcium dynamics in deep-layer cortical pyramidal neurons. *Nature neuroscience* **2,** 989-996.
14. Svoboda, K., Helmchen, F., Denk, W., & Tank, D. W. (1999) Spread of dendritic excitation in layer 2/3 pyramidal neurons in rat barrel cortex in vivo. *Nature neuroscience* **2,** 65-73.

15. Waters, J., Larkum, M., Sakmann, B., & Helmchen, F. (2003) Supralinear Ca2+ influx into dendritic tufts of layer 2/3 neocortical pyramidal neurons in vitro and in vivo. *J Neurosci* **23,** 8558-8567.
16. Bollmann, J. H. & Engert, F. (2009) Subcellular topography of visually driven dendritic activity in the vertebrate visual system. *Neuron* **61,** 895-905.
17. Euler, T., Detwiler, P. B., & Denk, W. (2002) Directionally selective calcium signals in dendrites of starburst amacrine cells. *Nature* **418,** 845-852.
18. Briggman, K. L., Helmstaedter, M., & Denk, W. (2011) Wiring specificity in the direction-selectivity circuit of the retina. *Nature* **471,** 183-188.
19. Elyada, Y. M., Haag, J., & Borst, A. (2009) Different receptive fields in axons and dendrites underlie robust coding in motion-sensitive neurons. *Nature neuroscience* **12,** 327-332.
20. Jia, H., Rochefort, N. L., Chen, X., & Konnerth, A. (2011) In vivo two-photon imaging of sensory-evoked dendritic calcium signals in cortical neurons. *Nature protocols* **6,** 28-35.
21. Jia, H., Rochefort, N. L., Chen, X., & Konnerth, A. (2010) Dendritic organization of sensory input to cortical neurons in vivo. *Nature* **464,** 1307-1312.
22. Chen, X., Leischner, U., Rochefort, N. L., Nelken, I., & Konnerth, A. (2011) Functional mapping of single spines in cortical neurons in vivo. *Nature*.
23. Varga, Z., Jia, H., Sakmann, B., & Konnerth, A. (2011) Dendritic coding of multiple sensory inputs in single cortical neurons in vivo. *Proc Natl Acad Sci U S A (accepted)*.

2 Dendritic organization of sensory input to cortical neurons *in vivo*

Background

This article included the major results of my thesis work, and was the first report of *in vivo* dendritic input mapping in cortical neurons. Before having achieved these results, many preliminary experiments had been performed with various methods. One series of those experiments, for example, involved two-photon imaging of single layer 2/3 visual cortical neuron after electroporation of calcium dye. In both basal and oblique dendrites, the dominant type of signals found were the widespread global calcium transients that were either spontaneous or visually evoked. Loose cell-attach recordings on the electroporated neuron showed that these widespread dendritic calcium signals were correlated with action potential firings. Thus, these widespread calcium signals on basal and oblique dendrites were likely to be induced by back-propagation of action potentials (bAPs), similar to previously reported (as ref #7, 9 in the original paper) recordings on the apical trunk dendrites. Therefore, whole-cell recording was employed, with the idea to use depolarizing current pulse to induce action potentials and thus testing their causality in the global dendritic calcium signals. However, it turned out to be not easy to precisely induce a fixed number of action potentials due to large fluctuations of synaptic current of the neuron itself. Then the strategy was changed to the prevention of action potential firing, which was easily achieved by hyperpolarizing the neuron until sufficient level. When the widespread bAPs-related dendritic calcium signals were abolished under this condition, the sensory input related local dendritic calcium signals could be detected. With this key rendered by the combination of whole-cell recording and two-photon calcium imaging, the gate to the mapping of sensory input to cortical neurons *in vivo* was eventually opened.

ARTICLES

Dendritic organization of sensory input to cortical neurons *in vivo*

Hongbo Jia[1]*, Nathalie L. Rochefort[1]*, Xiaowei Chen[1] & Arthur Konnerth[1]

In sensory cortex regions, neurons are tuned to specific stimulus features. For example, in the visual cortex, many neurons fire predominantly in response to moving objects of a preferred orientation. However, the characteristics of the synaptic input that cortical neurons receive to generate their output firing pattern remain unclear. Here we report a novel approach for the visualization and functional mapping of sensory inputs to the dendrites of cortical neurons *in vivo*. By combining high-speed two-photon imaging with electrophysiological recordings, we identify local subthreshold calcium signals that correspond to orientation-specific synaptic inputs. We find that even inputs that share the same orientation preference are widely distributed throughout the dendritic tree. At the same time, inputs of different orientation preference are interspersed, so that adjacent dendritic segments are tuned to distinct orientations. Thus, orientation-tuned neurons can compute their characteristic firing pattern by integrating spatially distributed synaptic inputs coding for multiple stimulus orientations.

A growing amount of evidence indicates that information processing in the brain involves the computation of electrical and chemical signals in neuronal dendrites (for a review, see ref. 1). One of the most effective ways for the analysis of these dendritic signals relies on the imaging of the dynamics of intracellular Ca^{2+} concentration (reviewed in ref. 2). Thus, synaptic input-related dendritic Ca^{2+} transients have been identified and studied in detail *in vitro*[3–6], while *in vivo* work has explored action-potential-related dendritic Ca^{2+} signals[7–9]. However, nothing is known about the nature of subthreshold sensory evoked input signals in the dendrites of mammalian cortical neurons. A detailed knowledge of sensory input signals would represent an important step forward in the understanding of dendritic computation[1,10–13]. An intriguing open question is whether sensory inputs with similar features are clustered on the same dendrite of a neuron or dispersed throughout the dendritic tree. Clustered inputs are capable of generating dendritic spikes (reviewed in ref. 11) and may form neuronal computational subunits *in vivo*, as they do under certain experimental conditions *in vitro*[14]. Alternatively, sensory inputs that are not clustered, but widely distributed, may underlie different rules of integration and formation of neuronal output signals—like, for example, the linear summation of excitatory inputs[15].

Visually evoked supra- and subthreshold activity

For the functional analysis of spiny dendrites *in vivo* by means of two-photon calcium imaging, we selected as an experimental model neurons in layer 2/3 of the mouse primary visual cortex (Fig. 1a–c). The somata of the neurons were located approximately between 140 and 200 μm below the cortical surface. Their dendritic trees had a characteristic pattern, consisting of numerous basal and oblique dendrites but no pronounced apical trunk[16–18] (Fig. 1a). As in many other mammalian species[19–21], layer 2/3 neurons of the mouse primary visual cortex respond selectively to drifting gratings or bars with action potential firing[22–24]. By performing whole-cell recordings involving the 'shadow-patching' approach[25], we found that stimulation with drifting gratings shifted the membrane potential to the 'up-state'[26] for the entire duration of the stimulus. An increased probability of up-states during drifting grating stimulation was previously observed in the cat visual cortex[27]. The neuron illustrated in Fig. 1d fired action potentials preferentially during the presentation of specifically oriented drifting gratings and was identified as a 'highly-tuned' neuron (Fig. 1e left) on the basis of its orientation selectivity index (OSI), which was higher than 0.5 (Methods). In our recordings, 6 out of 17 neurons were highly tuned for a preferred orientation (Fig. 1f left), 6/17 neurons were poorly tuned, while the rest of 5/17 neurons did not respond reliably to visual stimulation. For a better assessment of the stimulus-evoked subthreshold depolarization in highly tuned neurons, we hyperpolarized them to subthreshold membrane potentials. In the example shown in Fig. 1d, the neuron was hyperpolarized from its resting level of −64 mV to −70 mV. In contrast to the highly tuned action potential pattern (Fig. 1e left), the stimulus-evoked subthreshold depolarizing responses were broadly tuned in this (Fig. 1e right) as well as in all other highly tuned neurons (Fig. 1f right). Thus, in mouse visual cortex, as in cat visual cortex[28,29], the high tuning level of action potential firing, the neuronal output signal, contrasts with the low tuning level of the afferent subthreshold input signals.

These observations prompted us to combine whole-cell recordings with two-photon calcium imaging to search for dendritic signals associated with the afferent activity. We performed high-speed two-photon imaging at 30 full frames per second or 60 half frames per second using resonant galvo-scanners[30] and, initially, focused on the dendrites that were visible in the plane of focus containing the cell body (Fig. 1g). When stimulated with their preferred orientation, neurons responded with action potential firing that was associated with global dendritic calcium transients in all imaged dendrites. In the neuron illustrated in Fig. 1g, all five visible dendrites displayed calcium transients that were larger when the neuron fired four action potentials (Fig. 1h left) than when it fired two action potentials (Fig. 1h right). The dependence of the calcium transient amplitude on the number of action potentials and the observation that similar calcium transients were evoked by direct neuronal depolarization through the recording pipette (Supplementary Fig. 1a–c) indicate

[1]Institute of Neuroscience and Center for Integrated Protein Science, Technical University Munich, Biedersteinerstrasse 29, 80802 Munich, Germany.
*These authors contributed equally to this work.

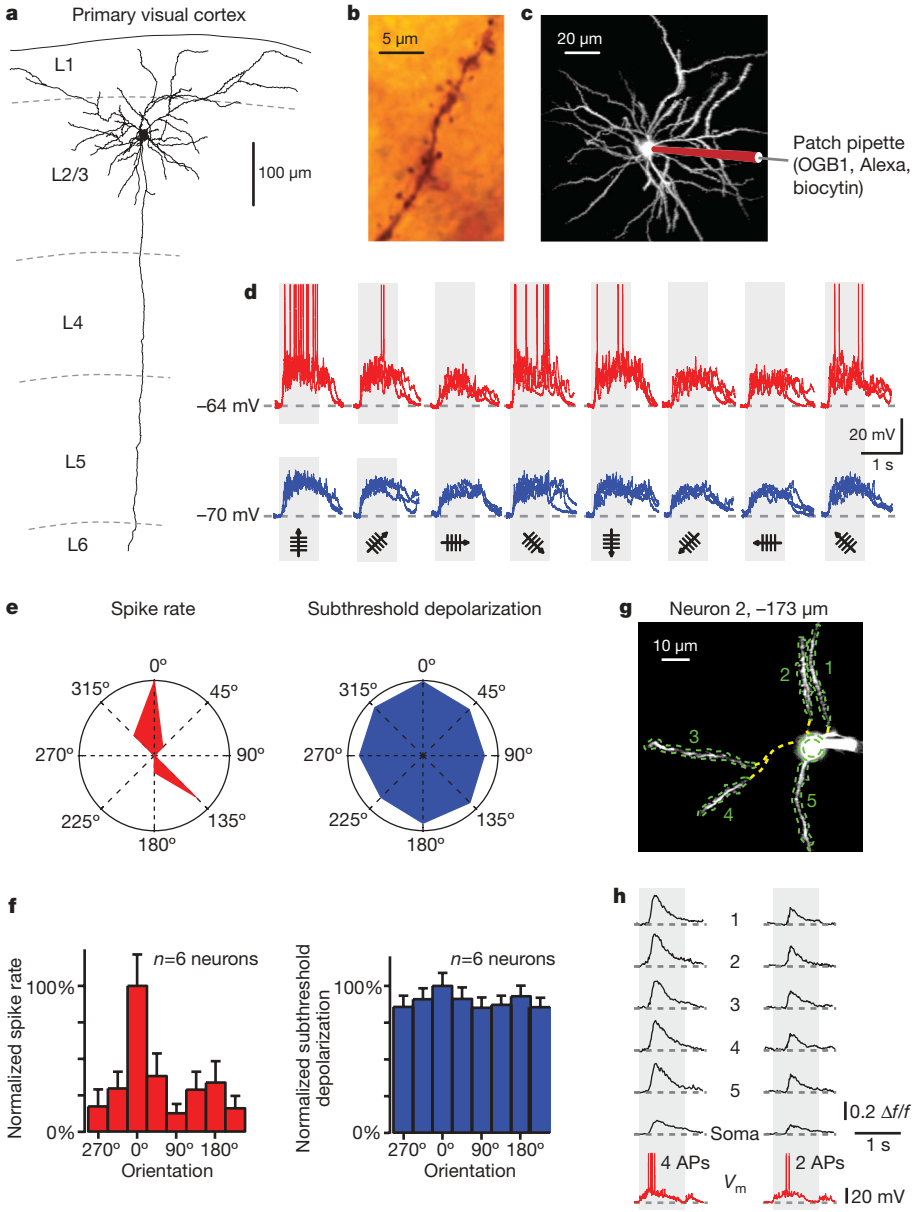

Figure 1 | Visually evoked action potentials, subthreshold depolarizations and global dendritic calcium signals. **a**, Reconstruction of a biocytin-filled layer 2/3 (L2/3) neuron in mouse primary visual cortex (projection along the antero-posterior axis). Data from the same neuron are presented in **b**–**e**. **b**, Microphotograph of a spiny basal dendrite. **c**, Projection along the dorso-ventral axis obtained *in vivo* from 469 sections (step size 0.5 µm) from Alexa fluorescence. **d**, Whole-cell current-clamp recordings of responses to drifting gratings of different orientations. Three trials were superimposed. Upper red traces, action potential responses at resting potential (indicated on the left); lower blue traces, subthreshold responses obtained after hyperpolarizing the neuron to −70 mV. **e**, Polar plots of visually evoked responses, average of eight trials. Red plot, spike rate; blue plot, amplitude of subthreshold depolarization. **f**, Tuning properties of spiking and subthreshold responses for six orientation-selective neurons, each normalized to their preferred orientation (noted as 0°). Error bars, +s.d. **g**, **h**, Two-photon imaging of dendritic calcium signals in basal and oblique dendrites of another layer 2/3 neuron during action potential firing (electrical recording lower red trace) evoked by drifting gratings. **g**, Average image of 100 frames recorded at 173 µm below the cortical surface. Yellow dashed lines indicate out-of-focus portions of the dendrites. Green dashed lines indicate the regions of interest (ROIs). **h**, Ca^{2+}-dependent fluorescence changes (black traces) recorded in the soma and in five dendrites (indicated by numbers in **g**) and the corresponding membrane potential (V_m, red traces) recordings, during two separate trials. Light grey bars indicate the stimulation period with oriented gratings. AP, action potential.

that such global dendritic signals are largely due to the activation of voltage-gated calcium channels by back-propagating action potentials; this has previously been shown for basal dendrites in *in vitro* recordings from layer 2/3 neurons[31,32]. The amplitude of the Ca^{2+} transients at different dendritic sites showed attenuation along a given dendrite (Supplementary Fig. 1d, e) and variations from trial to trial, but we were unable to obtain unambiguous evidence for signal peaks that would correspond to specific synaptic inputs, as found in tectal neurons of the tadpole[33]. Therefore, we decided to search for calcium signals associated with subthreshold synaptic calcium signalling in conditions in which we actively hyperpolarized the neurons.

Subthreshold calcium signals in dendritic hotspots

Figure 2 illustrates the results of an experiment in which a neuron was hyperpolarized to −70 mV to prevent action potential firing. In these conditions, a calcium transient was evoked in a subregion of 'dendrite 3' (Fig. 2a, b) by visual stimulation (drifting grating), but not detected in the other dendrites or in the soma. To assess the spatial dimensions of such local calcium transients, we analysed experiments

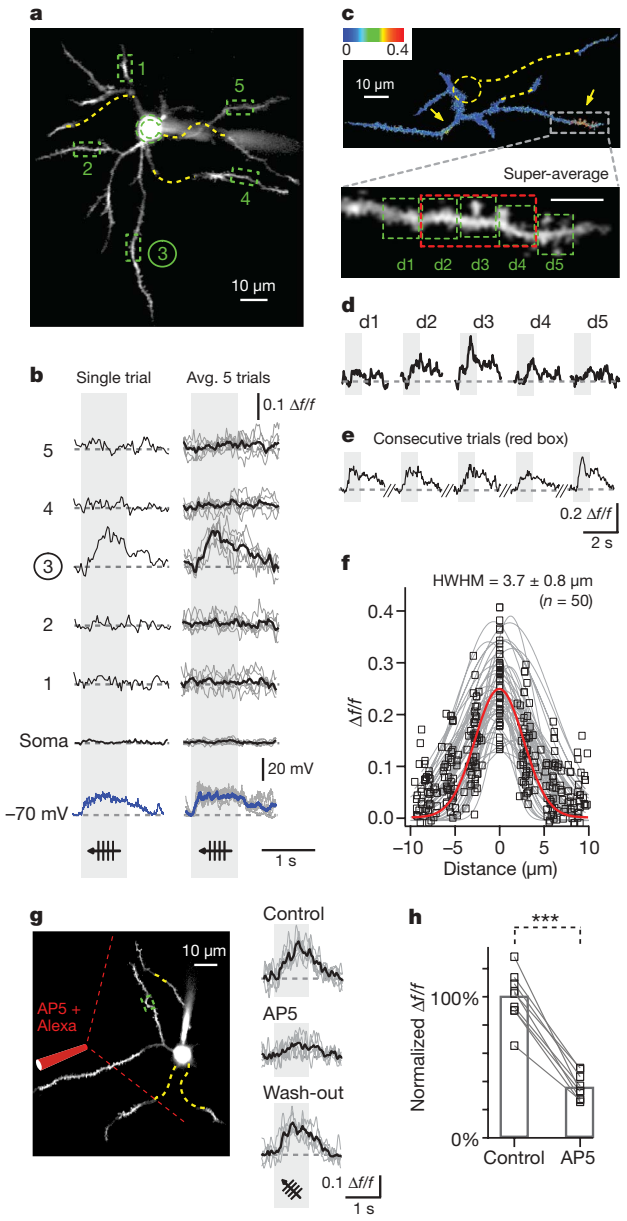

Figure 2 | Subthreshold local dendritic calcium signals evoked by drifting grating stimulation. **a**, Two-photon image used for calcium recordings in **b**. The image is an average of 100 frames. Five ROIs are indicated by green dashed rectangles. **b**, Subthreshold Ca^{2+} transients (black traces) and corresponding depolarization (blue traces) evoked by drifting grating stimulation. Note the prominent Ca^{2+} signal in dendrite 3. Left traces, single trials; right traces, average (black trace) of five individual trials (grey traces) from various dendritic sites and soma, as indicated. **c**, Upper panel, pseudo-colour image of local dendritic Ca^{2+} signals. Ratio of the averages of 30 frames before and 30 frames during stimulation. Yellow arrows indicate two sites of local dendritic calcium signals. Lower panel, enlarged view of the dashed box indicated in the upper image, 'super-average' obtained from 500 frames. **d**, Calcium recordings from five neighbouring dendritic regions of 3 µm length (d1–d5, ROIs shown in **c**), average of five trials. **e**, Calcium signals evoked during five consecutive trials within the ROI indicated by the red dashed line in **c**. **f**, Amplitude distribution of calcium signals within dendritic hotspots ($n = 50$ hotspots, 17 neurons). Grey dashed lines indicate the Gaussian fitting to the amplitude distribution of calcium signals within individual hotspots. Red line indicates the Gaussian fit to all points. Average half-width at half-maximum (HWHM) with standard deviation (±) is indicated. **g**, Left, two-photon image of a neuron (average $n = 100$ frames) and schematic representation of drug application pipette containing AP5 and Alexa-594. The red dashed lines indicate the approximate area of drug application. The green dashed box is the ROI for calcium monitoring. Right, Ca^{2+} recordings before, during and after the application of AP5. Average trace (black line) of five individual trials (grey lines). **h**, Amplitude of calcium signals before and during the application of AP5 obtained from $n = 9$ local calcium signals in four neurons. The amplitude of each Ca^{2+} signal was normalized to the mean amplitude of all signals in control condition. Paired *t*-test, $***P < 0.0001$.

in which long portions of the same dendrite were discernible in the plane of focus of our recordings. In the neuron shown in Fig. 2c, we identified two dendritic hotspots of visually evoked local calcium transients. The systematic analysis of segments with a length of 3 µm along the dendrite showed that the calcium signal was present in three neighbouring segments with a clear peak in the middle segment (Fig. 2c, d). Repetitive visual stimulation reliably evoked local dendritic calcium signals (Fig. 2e; mean failure rate 22 ± 18%, 61 hotspots in 17 neurons). The spatial extent of these dendritic hotspots had an average half-width at half-maximum (HWHM) of 3.7 ± 0.8 µm ($n = 50$) (Fig. 2f).

What is the mechanism underlying these calcium signals? First, we noticed that the NMDA (*N*-methyl-D-aspartate) receptor antagonist D(−)-2-amino-5-phosphonovaleric acid (AP5) caused a major attenuation of the calcium transients, indicating their synaptic origin (Fig. 2g, h). Second, the dimensions of the hotspots were quite similar to the active dendritic shaft segments of pyramidal neurons *in vitro* displaying calcium transients as a result of the spread of calcium from single active spines[34,35]. In line with this possibility, we also identified spines at the hotspot region when constructing post hoc 'super-average' images (Fig. 2c bottom). Furthermore, previous recordings performed in basal dendrites of neocortical neurons *in vitro* demonstrated that focally evoked subthreshold excitatory post-synaptic potentials induce calcium transients in dendritic compartments of comparable dimensions[14]. In our recordings, the mean amplitude of hotspot calcium transients (Methods) was $\Delta f/f = 0.25 \pm 0.07$ ($n = 50$). This value is comparable to the amplitudes of back-propagating action-potentials-dependent dendritic calcium transients evoked by the preferred orientation ($\Delta f/f = 0.37 \pm 0.13$, mean number of action potentials 3.1 ± 1.1, $n = 50$; Supplementary Fig. 1c). Thus, the amplitude and the spatial extent of these visually evoked calcium transients resemble those generated by individual synaptic inputs, but not those evoked by dendritic NMDA spikes, which produce calcium transients that cover larger dendritic domains and have manifold larger amplitudes[31,36,37].

Mapping dendritic distribution of sensory inputs

To determine the spatial distribution of the dendritic hotspots reflecting sensory inputs, we performed experiments in which we attempted to image as many focal planes as possible in every neuron, requiring 1–2 h of whole-cell recording. In each focal plane, we determined the orientation preference of the local calcium signals by presenting drifting gratings (Methods). Figure 3a illustrates an experiment in which four focal planes were imaged at various depths under the cortical surface. A total of 13 hotspots were identified in this neuron. Figure 3b shows the response from three selected hotspots (numbered 4, 12 and 7 in Fig. 3a) obtained during presentation of eight directions of drifting gratings. From these averaged calcium transients ($n = 6$ trials), we constructed polar plots for each hotspot (Fig. 3c). A closer inspection of the polar plots revealed the presence of multiple orientation preferences in this and all other neurons. The dendritic distribution of the orientation preferences did not appear to follow any strict rule, but seemed to be randomly distributed throughout the dendritic tree. Another remarkable finding is that the calcium transients of most local dendritic hotspots displayed a pronounced orientation preference. In order to quantify the tuning level, we calculated the OSI for each hotspot and found that the majority of hotspots (72%, $n = 102$) were highly tuned for a particular orientation (OSI > 0.5). The average OSI value for all hotspots of the neuron shown in Fig. 3 was 0.63. Comparable results were obtained from 16 additional neurons (mean OSI = 0.59; $n = 102$

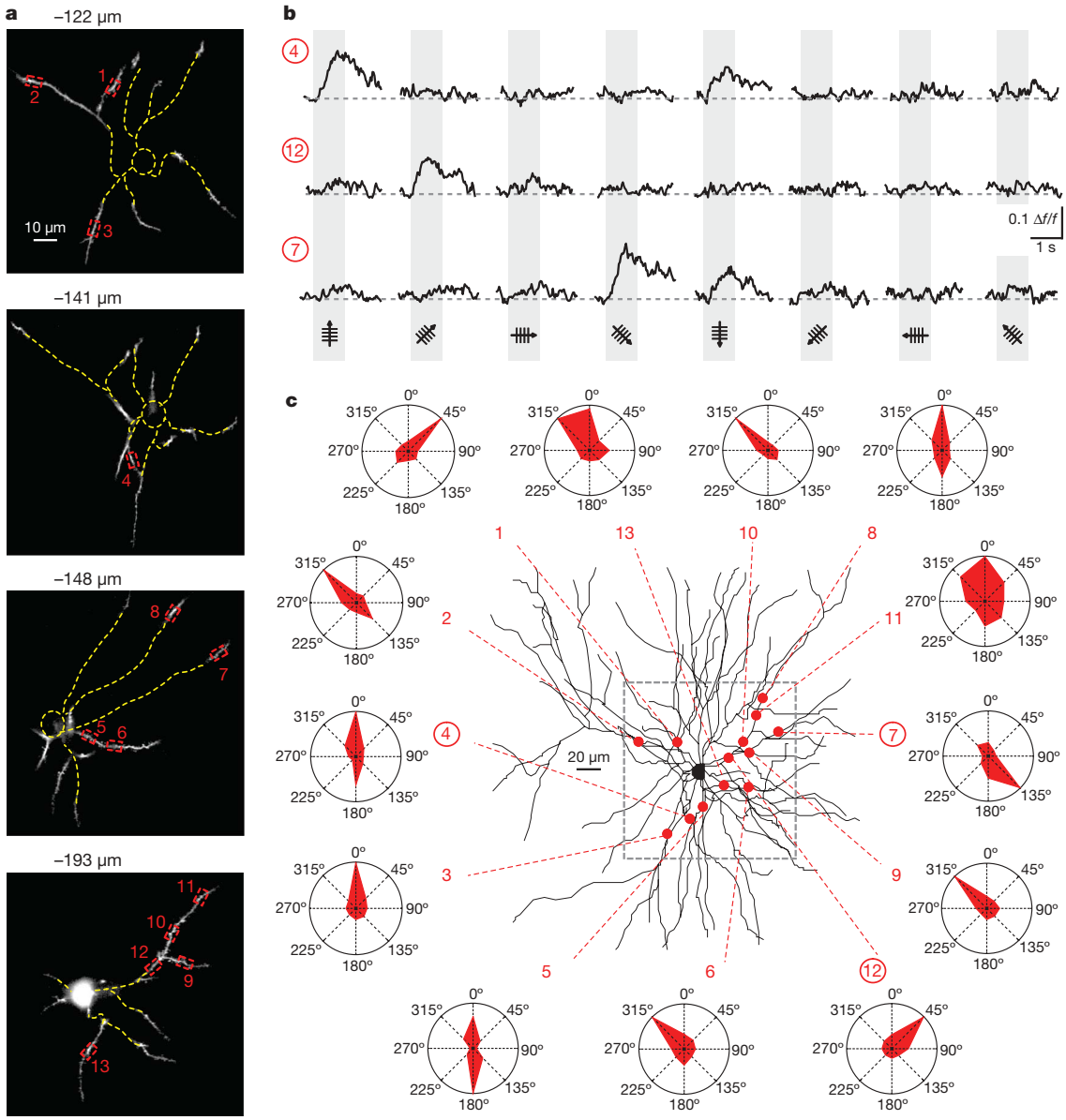

Figure 3 | Heterogeneity and distribution pattern of orientation-tuned dendritic hotspots. **a**, Four two-photon images (each an average of $n = 100$ frames) of a layer 2/3 neuron obtained at different depths under the cortical surface as indicated. Red dashed boxes indicate hotspots of local dendritic calcium signalling. **b**, Local dendritic calcium signals evoked by drifting gratings of different orientations (average of six trials) at three different dendritic sites indicated in **a**. **c**, Location of each hotspot indicated as a red dot on the *Z*-projection of the reconstructed dendritic tree. Red dashed lines point to the polar plot obtained for the corresponding local Ca^{2+} signals. The frame (grey dashed line) indicates the area of imaging. The output signal of the neuron was tuned for the vertical orientation.

hotspots). An important finding was that dendritic hotspots were found in each of the recorded neurons (17/17), regardless of the tuning level of action potential firing and even in the neurons that were not reliably firing in response to drifting gratings. This suggests that these hotspots represent a general and highly reliable feature of layer 2/3 neurons of the primary visual cortex.

Hotspots of the same orientation preference in a given neuron were found widely dispersed over various dendrites. For example, in the neuron shown in Fig. 4a left, we identified six hotspots for the stimulus orientation indicated in the figure and, remarkably, each hotspot was on a different dendritic branch. The analysis of a larger set of neurons ($n = 8$, Fig. 4a right) confirmed this widespread distribution and emphasized the absence of any clustering of inputs on single dendrites. Furthermore, hotspots coding for the same orientation were found throughout the entire three-dimensional space surrounding the cell body. A similar wide distribution was observed for all four orientations tested (Supplementary Fig. 2). The absence of input clustering became particularly obvious when we analysed the inputs to individual dendritic branches. Figure 4b shows three examples of dendritic branches with neighbouring hotspots that have different orientation preferences. In 9/10 dendritic branch segments, localized between two branching points, we encountered two or three hotspots tuned for different orientation preferences. In just one out of these 10 cases, neighbouring hotspots coded for the same orientation. The graph in Fig. 4c right summarizes these results. The left panel of Fig. 4c shows that all 'full dendrites', that is, individual dendrites together with all their higher order branches, received inputs for multiple orientations. Finally, we compared in 12 neurons the tuning levels of the firing pattern, representing the output signal, with the tuning levels of local dendritic calcium responses, representing the synaptic input signals. Experimentally, the orientation preference of spike firing in these neurons was determined during the initial 25–30 min of whole-cell recording during which the calcium indicator dye was allowed to equilibrate in the dendrites. Then, the neurons

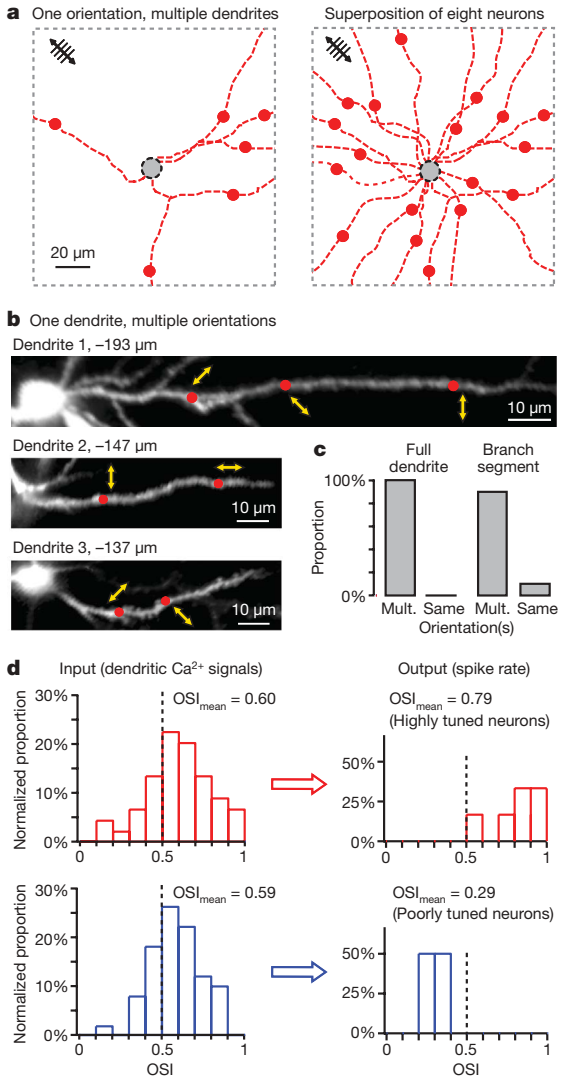

Figure 4 | Spatial arrangement of dendritic hotspots and input–output relation. a, Distribution of dendritic hotspots (red dots) tuned for the orientation preference indicated in the upper left corner, in the dendritic tree of a neuron (left panel). Right panel, summary of the results obtained for the same orientation in eight neurons. Cell bodies are indicated by the grey-filled dashed circles (black), dendrites are indicated by dashed red lines (*Z*-projections reconstructed from stacks). **b**, Three two-photon images of dendrites (each an average of $n = 100$ frames) at higher magnification with hotspots as indicated. Yellow arrows indicate the preferred orientation of local calcium signal in the corresponding hotspot. Note that the hotspots in dendrites 2 and 3 as well as the two distal hotspots in dendrite 1 were located in branch point-delimited segments. **c**, Summary graphs. Left panel, the proportion of full dendrites ($n = 12$) with hotspots coding for multiple orientations versus those with just one and the same orientation (≥3 hotspots per full dendrite). Right panel, the proportion of branch segments (between two branching points) with hotspots coding for multiple orientations versus those with the same orientation (≥2 hotspots per branch, $n = 10$). **d**, Input–output relations in highly tuned (upper) and poorly tuned (lower) neurons. The red and blue histograms show orientation selectivity indices (OSIs as indicated) for the input (Ca^{2+} signals in dendritic hotspots) and the output (spiking rate) of highly and poorly tuned neurons ($n = 6$ for each group), respectively.

were hyperpolarized and we determined the orientation preference of local dendritic calcium signals. We compared six highly tuned neurons (mean OSI = 0.79) with six broadly tuned ones (mean OSI = 0.29) (Fig. 4d right). Unexpectedly, the input signals had very similar tuning levels for the two neuronal groups, with mean OSI values of 0.60 and 0.59, for highly and broadly tuned firing patterns, respectively. This disparity between input and output signals, combined with the above-mentioned observation that all neurons had input signals coding for multiple orientations, indicates that the orientation preference of the output signal is the result of a computational process taking place on the level of individual neurons.

Conclusions

Our results reveal basic insights into the dendritic organization of sensory inputs to neurons of the visual cortex *in vivo*. First, we identified discrete dendritic hotspots as synaptic entry sites for specific sensory features. These hotspots represent novel dendritic calcium signals *in vivo* and were found in all layer 2/3 neurons, irrespective of their output firing pattern. Second, we showed that afferent sensory inputs with the same orientation preference are widely dispersed over the dendritic tree and do not converge on single dendrites, as repeatedly proposed in recent years (see review in ref. 11 and references therein). Third, we found that even neurons with a highly tuned output signal receive input signals that are heterogeneous and code for multiple orientations and/or directions. Thus, taken together, our results support a neuronal integration model involving summation of distributed inputs, rather than models that stress the role of convergent inputs to single dendrites[6,15]. However, it is certainly possible that other types of cortical neurons, especially those with pronounced apical tufts[38] or neurons in other species with a columnar organization of the visual cortex[17,19–21], have more clustered sensory inputs to the same dendrite, capable of generating large amplitude dendritic spikes[6,11]. The approach introduced in this study opens the way to a detailed analysis of various types of neurons followed by the construction of functional wiring diagrams of sensory pathways with single input resolution *in vivo*.

METHODS SUMMARY

C57BL/6 mice (postnatal day (P)28–P34) were prepared for *in vivo* two-photon calcium imaging and whole-cell recordings under isoflurane anaesthesia as described previously[39]. Whole-cell patch-clamp recordings of layer 2/3 neurons of primary visual cortex (monocular region) were performed by 'shadow-patching'[25]. Neurons were dialysed with a pipette solution containing the fluorescent Ca^{2+} indicator Oregon green BAPTA-1 hexapotassium (OGB-1; 100 µM), Alexa-594 (25 µM) and biocytin (2 mg ml^{-1}). Basal and oblique dendrites that appeared on the same focal plane were imaged by high-speed two-photon microscopy involving a resonant galvo-scanner[30]. Membrane potential changes and Ca^{2+} signals were simultaneously recorded. The focal plane depth and the imaged area were chosen to contain as many dendrites as possible. At each focal plane, we imaged the activity evoked by drifting square wave gratings (0.03 cycles per degree, 1 Hz, eight directions, standing phase 2 s, drifting phase 1 s). Transient changes in Ca^{2+} fluorescence ($\Delta f/f$) were systematically examined by an adaptive algorithm, which involved small regions of interest (ROIs) of 3×4 µm, noise filtering and pattern matching. The NMDA receptor antagonist AP5 (together with Alexa-594) was locally applied by pressure ejection close to the imaged dendrites. The spread of the ejected solution was monitored by imaging Alexa fluorescence. The tuning level of local dendritic calcium signals with regard to the orientation of the drifting grating was quantified by an OSI[24].

Received 14 October 2009; accepted 24 February 2010.

1. London, M. & Häusser, M. Dendritic computation. *Annu. Rev. Neurosci.* **28,** 503–532 (2005).
2. Bloodgood, B. L. & Sabatini, B. L. Ca^{2+} signaling in dendritic spines. *Curr. Opin. Neurobiol.* **17,** 345–351 (2007).
3. Markram, H. & Sakmann, B. Calcium transients in dendrites of neocortical neurons evoked by single subthreshold excitatory postsynaptic potentials via low-voltage-activated calcium channels. *Proc. Natl Acad. Sci. USA* **91,** 5207–5211 (1994).
4. Nevian, T. & Sakmann, B. Spine Ca^{2+} signaling in spike-timing-dependent plasticity. *J. Neurosci.* **26,** 11001–11013 (2006).
5. Yuste, R. & Denk, W. Dendritic spines as basic functional units of neuronal integration. *Nature* **375,** 682–684 (1995).
6. Häusser, M. & Mel, B. Dendrites: bug or feature? *Curr. Opin. Neurobiol.* **13,** 372–383 (2003).
7. Helmchen, F., Svoboda, K., Denk, W. & Tank, D. W. *In vivo* dendritic calcium dynamics in deep-layer cortical pyramidal neurons. *Nature Neurosci.* **2,** 989–996 (1999).
8. Murayama, M. *et al.* Dendritic encoding of sensory stimuli controlled by deep cortical interneurons. *Nature* **457,** 1137–1141 (2009).

9. Svoboda, K., Denk, W., Kleinfeld, D. & Tank, D. W. *In vivo* dendritic calcium dynamics in neocortical pyramidal neurons. *Nature* **385,** 161–165 (1997).
10. Johnston, D. & Narayanan, R. Active dendrites: colorful wings of the mysterious butterflies. *Trends Neurosci.* **31,** 309–316 (2008).
11. Larkum, M. E. & Nevian, T. Synaptic clustering by dendritic signalling mechanisms. *Curr. Opin. Neurobiol.* **18,** 321–331 (2008).
12. Ohki, K. & Reid, R. C. Specificity and randomness in the visual cortex. *Curr. Opin. Neurobiol.* **17,** 401–407 (2007).
13. Magee, J. C. Dendritic integration of excitatory synaptic input. *Nature Rev. Neurosci.* **1,** 181–190 (2000).
14. Polsky, A., Mel, B. W. & Schiller, J. Computational subunits in thin dendrites of pyramidal cells. *Nature Neurosci.* **7,** 621–627 (2004).
15. Cash, S. & Yuste, R. Linear summation of excitatory inputs by CA1 pyramidal neurons. *Neuron* **22,** 383–394 (1999).
16. Bannister, A. P. Inter- and intra-laminar connections of pyramidal cells in the neocortex. *Neurosci. Res.* **53,** 95–103 (2005).
17. Hirsch, J. A. & Martinez, L. M. Laminar processing in the visual cortical column. *Curr. Opin. Neurobiol.* **16,** 377–384 (2006).
18. Svoboda, K., Helmchen, F., Denk, W. & Tank, D. W. Spread of dendritic excitation in layer 2/3 pyramidal neurons in rat barrel cortex *in vivo*. *Nature Neurosci.* **2,** 65–73 (1999).
19. Hubel, D. H. & Wiesel, T. N. Receptive fields, binocular interaction and functional architecture in the cat's visual cortex. *J. Physiol. (Lond.)* **160,** 106–154 (1962).
20. Hubel, D. H. & Wiesel, T. N. Receptive fields and functional architecture of monkey striate cortex. *J. Physiol. (Lond.)* **195,** 215–243 (1968).
21. White, L. E. & Fitzpatrick, D. Vision and cortical map development. *Neuron* **56,** 327–338 (2007).
22. Dräger, U. C. Receptive fields of single cells and topography in mouse visual cortex. *J. Comp. Neurol.* **160,** 269–290 (1975).
23. Métin, C., Godement, P. & Imbert, M. The primary visual cortex in the mouse: receptive field properties and functional organization. *Exp. Brain Res.* **69,** 594–612 (1988).
24. Niell, C. M. & Stryker, M. P. Highly selective receptive fields in mouse visual cortex. *J. Neurosci.* **28,** 7520–7536 (2008).
25. Kitamura, K., Judkewitz, B., Kano, M., Denk, W. & Häusser, M. Targeted patch-clamp recordings and single-cell electroporation of unlabeled neurons *in vivo*. *Nature Methods* **5,** 61–67 (2008).
26. Kerr, J. N., Greenberg, D. & Helmchen, F. Imaging input and output of neocortical networks *in vivo*. *Proc. Natl Acad. Sci. USA* **102,** 14063–14068 (2005).
27. Anderson, J., Lampl, I., Reichova, I., Carandini, M. & Ferster, D. Stimulus dependence of two-state fluctuations of membrane potential in cat visual cortex. *Nature Neurosci.* **3,** 617–621 (2000).
28. Carandini, M. & Ferster, D. Membrane potential and firing rate in cat primary visual cortex. *J. Neurosci.* **20,** 470–484 (2000).
29. Bringuier, V., Chavane, F., Glaeser, L. & Fregnac, Y. Horizontal propagation of visual activity in the synaptic integration field of area 17 neurons. *Science* **283,** 695–699 (1999).
30. Rochefort, N. L. *et al.* Sparsification of neuronal activity in the visual cortex at eye-opening. *Proc. Natl Acad. Sci. USA* **106,** 15049–15054 (2009).
31. Gordon, U., Polsky, A. & Schiller, J. Plasticity compartments in basal dendrites of neocortical pyramidal neurons. *J. Neurosci.* **26,** 12717–12726 (2006).
32. Koester, H. J. & Sakmann, B. Calcium dynamics associated with action potentials in single nerve terminals of pyramidal cells in layer 2/3 of the young rat neocortex. *J. Physiol. (Lond.)* **529,** 625–646 (2000).
33. Bollmann, J. H. & Engert, F. Subcellular topography of visually driven dendritic activity in the vertebrate visual system. *Neuron* **61,** 895–905 (2009).
34. Kovalchuk, Y., Eilers, J., Lisman, J. & Konnerth, A. NMDA receptor-mediated subthreshold Ca^{2+} signals in spines of hippocampal neurons. *J. Neurosci.* **20,** 1791–1799 (2000).
35. Noguchi, J., Matsuzaki, M., Ellis-Davies, G. C. & Kasai, H. Spine-neck geometry determines NMDA receptor-dependent Ca^{2+} signaling in dendrites. *Neuron* **46,** 609–622 (2005).
36. Holthoff, K., Kovalchuk, Y., Yuste, R. & Konnerth, A. Single-shock LTD by local dendritic spikes in pyramidal neurons of mouse visual cortex. *J. Physiol. (Lond.)* **560,** 27–36 (2004).
37. Major, G., Polsky, A., Denk, W., Schiller, J. & Tank, D. W. Spatiotemporally graded NMDA spike/plateau potentials in basal dendrites of neocortical pyramidal neurons. *J. Neurophysiol.* **99,** 2584–2601 (2008).
38. Larkum, M. E., Nevian, T., Sandler, M., Polsky, A. & Schiller, J. Synaptic integration in tuft dendrites of layer 5 pyramidal neurons: a new unifying principle. *Science* **325,** 756–760 (2009).
39. Stosiek, C., Garaschuk, O., Holthoff, K. & Konnerth, A. *In vivo* two-photon calcium imaging of neuronal networks. *Proc. Natl Acad. Sci. USA* **100,** 7319–7324 (2003).

Supplementary Information is linked to the online version of the paper at www.nature.com/nature.

Acknowledgements We are grateful to B. Sakmann for discussions and to Y. Kovalchuk for help in the initial experiments. This work was supported by grants from the DFG (to A.K.) and the Friedrich Schiedel Foundation. A.K. is a Carl von Linde Senior Fellow of the Institute for Advanced Study of the TUM. H.J., N.L.R. and X.C. were supported by the DFG (IRTG 1373).

Author Contributions H.J., N.L.R. and X.C. carried out the experiments. H.J., N.L.R. and A.K. performed the analysis. A.K. designed the study and wrote the manuscript with the help of all authors.

Author Information Reprints and permissions information is available at www.nature.com/reprints. The authors declare no competing financial interests. Correspondence and requests for materials should be addressed to A.K. (arthur.konnerth@lrz.tum.de).

SUPPLEMENTARY INFORMATION

Supplementary Methods

Animals and surgery

All experimental procedures were performed in accordance with institutional animal welfare guidelines and were approved by the government of Bavaria, Germany. A total of 18 BL/6 mice (P28-P34) were prepared for *in vivo* experiments, as described previously[39]. Briefly, the mice were placed onto a warming plate (38°C) and anaesthetized by inhalation of 1.5% isoflurane (Curamed, Karlsruhe, Germany) in pure O_2. After removing the skin, a custom-made recording chamber[40] was then glued to the skull with cyanoacrylic glue (UHU, Buhl-Baden, Germany). The mouse was then transferred into the set-up, placed onto a warming plate (38° C) and continuously supplied with 0.8% isoflurane in pure O_2 (breathing rate 110-130 breaths per minute). A small craniotomy (~0.8×0.6 mm) was performed above the monocular region of primary visual cortex using a thin (30G) injection needle. The exposed region was subsequently covered by 2% agar (~1 mm thick) to reduce vibrations of brain tissue. The recording chamber was perfused with warm (37° C) extracellular perfusion saline containing (in mM): 125 NaCl, 4.5 KCl, 26 $NaHCO_3$, 1.25 NaH_2PO_4, 2 $CaCl_2$, 1 $MgCl_2$, 20 glucose, pH 7.4, when bubbled with 95% O_2 and 5% CO_2. Eye cream (Bepanthen, Bayer, Germany) was applied on both eyes to prevent dehydration during surgery. After surgery, the anaesthesia level was decreased to 0.8% isoflurane for recordings (breathing rate 110-130 breaths per minute).

Electrophysiology and drug application

The position of the primary visual cortex was located according to brain atlas coordinates (Bregma -3.5 to -4.5 mm, 2 to 2.5 mm lateral to the midline[41]). In all experiments the correct location of the recorded neurons was confirmed *in vivo* by their responses to visual stimuli and post-hoc by imaging of the stained brain area. *In vivo* whole-cell patch-clamp of layer 2/3 neurons was performed by using 'shadow patching'[25]. Borosilicate pipettes of 5 to 7 MΩ resistance were filled with a standard pipette solution (125 mM K-gluconate, 25 mM KCl, 12.5 mM HEPES, 5 mM Mg-ATP, 0.4 mM Na_2GTP, 12.5 mM Na-phosphocreatine) to which 100 µM Oregon Green BAPTA-1 Hexapotassium, 25 µM Alexa-594 and Biocytin (2 mg/ml; FLUKA), all dissolved in water, were added. Similar results were obtained in 3 experiments (3 neurons in 3 mice) when using a 'low chloride' pipette solution, containing 112 mM K-

gluconate, 8 mM KCl, 10 mM HEPES, 4 mM Mg-ATP, 0.375 mM Na_2GTP, 10 mM Na-Phosphocreatine, 100 µM Oregon Green BAPTA-1 Hexapotassium, 25 µM Alexa-594 (see Supplementary Fig. 3). Current-clamp recordings were made with an EPC-9 amplifier. Signals were filtered at 3 kHz and digitized at 10 kHz by the Pulse software (both from *HEKA*, Germany). Series resistances ranged from 15 to 40 MΩ. The resting membrane potentials ranged from – 67 to -62 mV. For the recordings of subthreshold activities, the neurons were hyperpolarized to membrane potentials below -70 mV. In the pharmacology experiments (n=4), a pipette filled with 5 mM d-AP5 and 25 µM Alexa-594 in standard extracellular saline solution was placed close to the imaged dendrites. The drug was delivered by gentle pressure injection. The area of diffusion was monitored at the beginning of each recording trial by imaging Alexa fluorescence.

High-speed two-photon Ca^{2+} imaging

In vivo Ca^{2+} imaging was performed by using a custom-built two-photon microscope based on Ti:Sapphire pulsing laser (model: Chameleon, repetition rate: 80 MHz, pulse width: 140 fs; Coherent, USA) and resonant galvo-mirror (8 kHz; GSI) system[42].

The scanner was mounted on an upright microscope (BX51WI, Olympus, Tokyo, Japan) equipped with a water-immersion objective (40x/0.8 Nikon, Japan). Emitted photons were detected by two detection channels equipped with photomultiplier tubes (H7422-40; Hamamatsu), a 'green' channel for OGB-1 dependent calcium recordings (480-560 nm) and a 'red' channel for the Alexa-594 generated fluorescence (580-680 nm). Full-frame images at 480×400 pixel resolution were acquired at 30 Hz or at a resolution of 480x180 pixels at 60 Hz by custom-programmed software based on LabVIEW™ (version 8.2; National Instruments, USA). Approximately 30 minutes after forming the whole-cell configuration, the basal and oblique dendrites were well labeled by OGB1. The focal plane was chosen to contain as many dendrites as possible. At each focal plane, we imaged spontaneous activity (for at least 2 min) as well as visually-evoked activity (6 to 10 trials of visual stimulation). At the end of each experiment, a Z-stack of the fluorescently labeled neuron was acquired (0.5 µm step size).

Visual stimulation

Visual stimuli were generated by Matlab™ (release 2007b; Mathworks Inc.) with the "Psychtoolbox" add-on package (http://psychtoolbox.org/wikka.php?wakka=HomePage). Visual stimuli were projected on a screen placed 30 cm from the contralateral eye, covering 80° x 67° of the visual field. Each trial of visual stimulation started with a gray screen (mean luminance) for 4 s, followed by a stationary square-wave grating for 2 s and the corresponding drifting phase for 1 s (0.03 cycle per degree, 1 Hz, 8 directions, contrast 80%, mean luminance 3.7 cd/m^2). At each focal plane, evoked activities were imaged during 6 to 10 trials.

Reconstruction of dendrites

For dendrite reconstructions, neurons were filled with Biocytin (2 mg/ml; FLUKA). At the end of the recordings, animals were transcardially perfused with phosphate buffer solution (0.1 M PBS) followed by 4 % paraformaldehyde (PFA) in 0.1 M PBS. Brains were kept in 4% PFA overnight and maintained in PBS thereafter. 100 µm-thin frontal sections were cut with a vibratome. Biocytin-labeled neurons were visualized using the avidin:biotinylated horseradish peroxidase complex (Vectastain ABC kit, Vector Laboratories, CA). Three neurons were completely reconstructed in 3D with the Neurolucida software (MicroBrightField, Colchester, VT, USA) using a up-right microscope (Zeiss, Germany) with an oil immersion x100/1.4 numerical aperture objective.

Data analysis

Electrophysiology and Ca^{2+} imaging data were analyzed off-line by using custom-written procedures in Igor™ and LabVIEW™. The amplitude of stimulus-evoked subthreshold depolarizing responses was calculated by subtracting the mean amplitude before the onset of drifting grating stimulation (0.2 s) from the mean value during the drifting period (1 s). Calcium-dependent changes in relative fluorescence (Δf/f) represent the mean fluorescence of all pixels within specified region-of-interests (ROIs). Local dendritic calcium signals were determined by analyzing the dendrites with consecutive small ROIs (rectangles of 3x4 µm) (e.g. Fig. 2c). All Δf/f traces were processed with an exponentially-averaging IIR filter (time constant 200 ms), then split according to the onset of drifting phase for each direction, and averaged over trials. Calcium transients were automatically detected with a template-

matching algorithm, taking into account the rise and decay times properties of the calcium signals. The amplitude of calcium transients was determined as the mean value in a time window around the peak response amplitude (1 frame before peak and 6 frames after). A calcium transient was accepted as a signal when its amplitude was greater than 3 times the standard deviation of the noise band. The tuning level of drifting grating-evoked responses was quantified by an orientation selectivity index (OSI)[24]. The OSI was defined as $(R_{pref} - R_{ortho})/(R_{pref} + R_{ortho})$, where R_{pref}, the response in the preferred orientation, was the response with the largest magnitude. For local dendritic calcium signals, R_{pref} was determined as the mean of the integral of the calcium transients for the two corresponding opposite directions. R_{ortho} was the similarly calculated response evoked by the orthogonal orientation. Highly and poorly tuned neurons were defined as neurons with an OSI>0.5 and OSI≤0.5 respectively. Polar plot representations of visually-evoked firing rates, of subthreshold depolarizations or of dendritic calcium transients were normalized with respect to the corresponding maximal responses.

References

40. Garaschuk, O., Milos, R. I. & Konnerth, A. Targeted bulk-loading of fluorescent indicators for two-photon brain imaging in vivo. *Nat Protoc.* **1**, 380-6 (2006).
41. Paxinos, G. & Franklin, K. B. J. The mouse brain in stereotaxic coordinates. Academic Press, San Diego, USA (2001).
42. Sanderson, M. J. & Parker, I. Video-rate confocal microscopy. *Methods Enzymol.* **360**, 447-81 (2003).

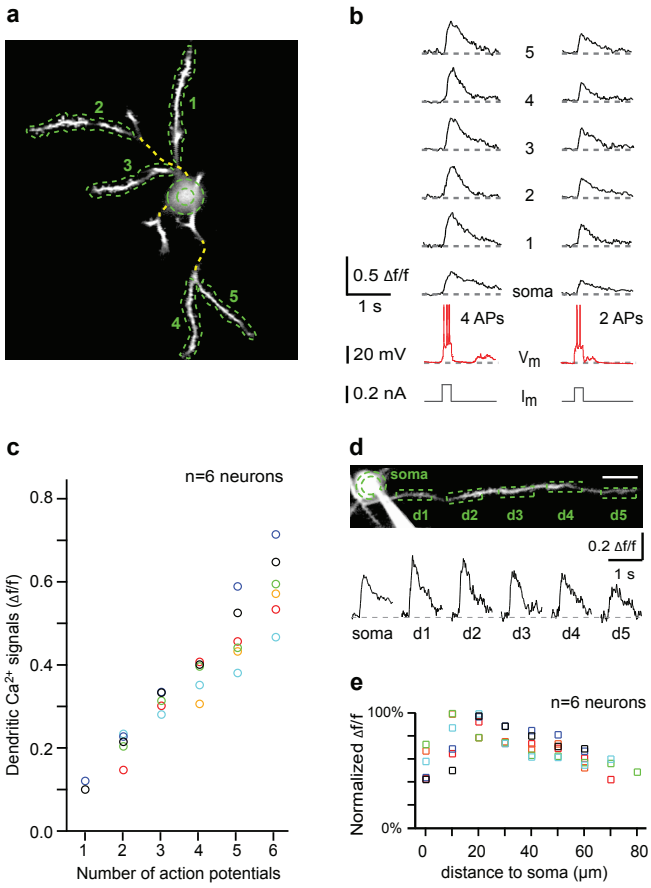

Supplementary Figure 1 | Global dendritic calcium signals are generated by back-propagating action potentials. a, Two-photon fluorescence image (average of 100 frames) of a layer 2/3 neuron in the mouse visual cortex. Yellow dotted lines indicate out-of-focus portions of dendrites. Green dotted lines indicate the region-of-interests (ROIs) for calcium recordings. **b**, Calcium transients (Δf/f) recorded in five dendrites and in the soma (indicated by numbers in panel a), during two trials in which 4 and 2 action potentials (APs) (V_m, lower red trace) were evoked by current injection (I_m, lowest gray trace). **c,** Amplitude of dendritic calcium transients versus the number of action potentials. Each color represents the mean value for a single neuron, recorded in dendritic ROIs of 50 µm length. **d-e,** Amplitudes of calcium transients plotted versus the distance from the soma. Recordings in panel d were obtained at the dendritic sites d1 through d5 and the soma, as indicated in the image (average of n=100 frames). The graph in panel e displays the amplitude of calcium transient at different dendritic distances for 6 neurons (marked in different colors). Each value represents the average amplitude obtained from 30 trials. For each trial, values were normalized with respect to the largest amplitude. Scale bar, 10 µm.

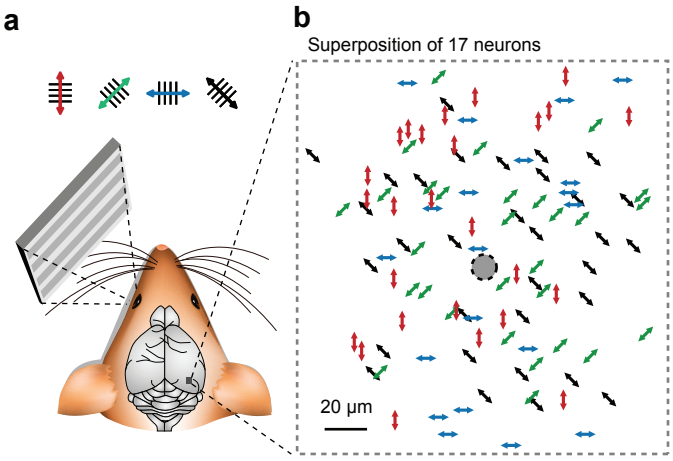

Supplementary Figure 2 | Highly heterogeneous distribution of orientation-tuned hot spots throughout the dendritic tree. a, Schematic of the experimental arrangement for visual stimulation. **b,** Superposition of orientation-tuned hot spots (Z-projection of n=107 sites) obtained from 17 layer 2/3 neurons. Each of the four orientations tested is displayed in a different color. The neurons' somata (gray filled black dotted circle) were superimposed. Note the salt-and-pepper distribution of the orientation-tuned hot spots.

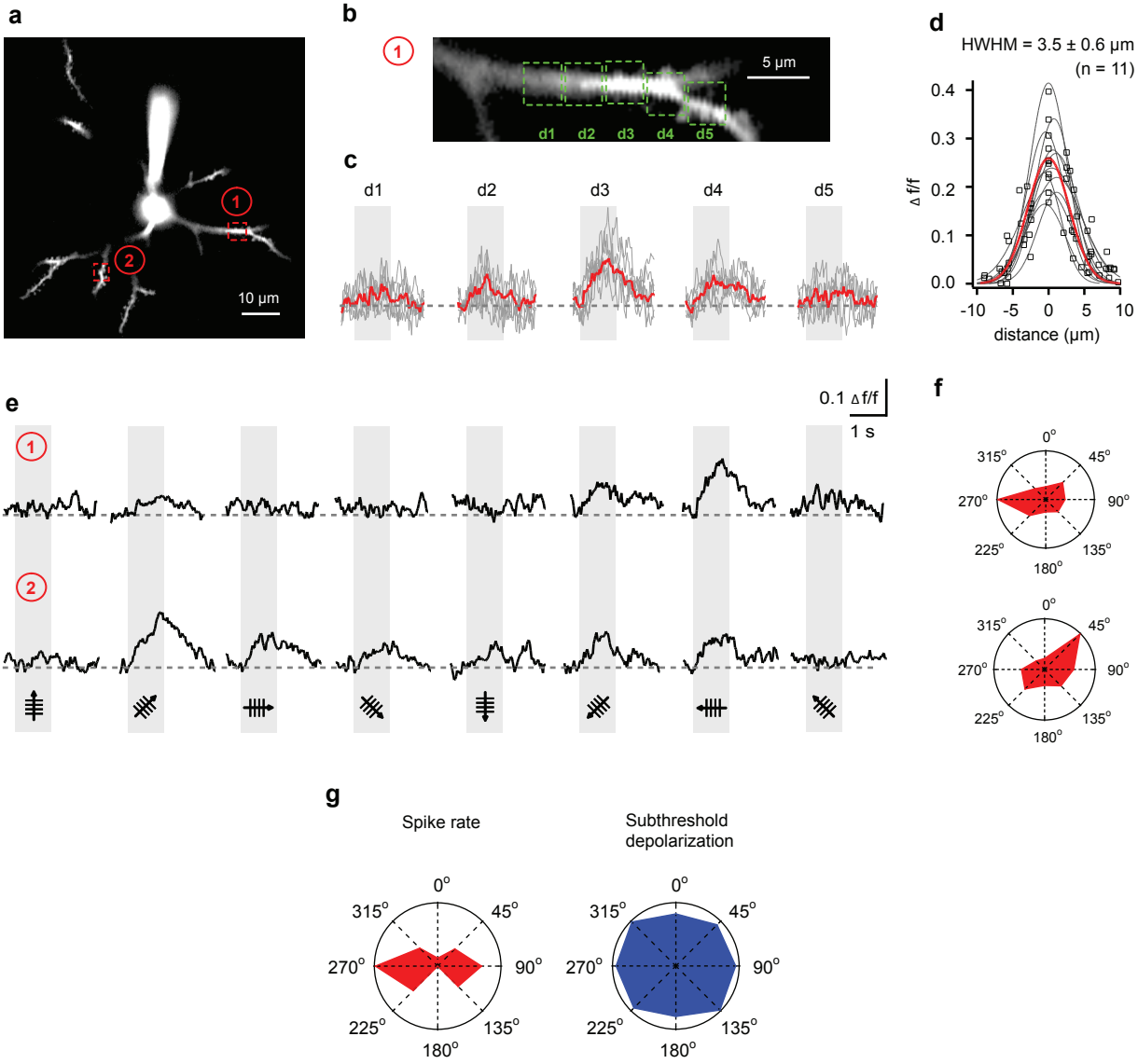

Supplementary Figure 3 | Subthreshold local dendritic calcium signals and membrane potential responses obtained with the 'low chloride' pipette solution Recordings from 3 neurons with a total of 11 hot spots.

a, Two-photon image (average of 500 frames) of a layer 2/3 neuron of the visual cortex of a 32-day-old mouse used for *in vivo* calcium recordings in panels c and e. Two hot spots are indicated by red dashed boxes. **b,** Enlarged view of the area near hot spot 1 as marked in panel a. The green dashed boxes d1 to d5 (3 µm length) indicate the regions of interest used for analysis. **c,** Superimposed 6 individual trials (gray traces) and the average (red traces) of calcium transients in d1 through d5. **d,** Amplitude distribution of calcium transients (n=11 hot spots, 3 neurons). Gray lines indicate the Gaussian fitting to the amplitude of calcium signals in dendritic regions at different distances from the center of each hotspot. Red line indicates the Gaussian fit to the pool of all data points. Average half-width at half-maximum (HWHM) with standard deviation as indicated. This HWHM value is not significantly different from that obtained with standard pipette solution (Fig. 2f). **e,** Local dendritic calcium signals evoked by drifting gratings of different orientations (average of 6 trials) for the two dendritic sites (as indicated in panel a). **f,** Polar plots obtained for the local calcium signals shown in panel e. Note the similarity to the results shown in Fig. 3c. **g,** Polar plots of visually-evoked electrical responses obtained with whole-cell recordings. Red plot: spike rate, average of 9 trials. Blue plot: amplitude of subthreshold depolarization, average of 25 trials. Note the similarity to the results shown in Fig. 1e.

3 *In vivo* two-photon imaging of sensory-evoked dendritic calcium signals in cortical neurons

Background

The combined method of two-photon calcium imaging and whole-cell recording has enabled the mapping of sensory evoked dendritic input sites in cortical neurons *in vivo*, as having been demonstrated in the previous chapter. Due to the publication style, many technical issues of the experiments were not explicitly described and discussed in the original paper. For example, how to perform a stable whole-cell recording for 2 hours in *vivo*? How to perform imaging on multiple dendrites? How to analyze the data? Therefore a step-by-step experimental protocol was required, as shown in this chapter. Note that it is not just an extension of the methods section of previous paper but also a stand-alone publication itself with new concepts. Specifically, at that time two parallel projects on the auditory cortex and barrel cortex using this method were in progress, providing much broader range of application of the method. The following paper illustrated the complete procedures of experiments in step-by-step manner, with the purpose that other labs could perform similar experiments by using this method.

PROTOCOL

In vivo two-photon imaging of sensory-evoked dendritic calcium signals in cortical neurons

Hongbo Jia[1,2], Nathalie L Rochefort[1,2], Xiaowei Chen[1] & Arthur Konnerth[1]

[1]Institute of Neuroscience and Center for Integrated Protein Science, Technische Universität München, München, Germany. [2]These authors contributed equally to this work. Correspondence should be addressed to A.K. (arthur.konnerth@lrz.tum.de).

Published online 9 December 2010; doi:10.1038/nprot.2010.169

Neurons in cortical sensory regions receive modality-specific information through synapses that are located on their dendrites. Recently, the use of two-photon microscopy combined with whole-cell recordings has helped to identify visually evoked dendritic calcium signals in mouse visual cortical neurons *in vivo*. The calcium signals are restricted to small dendritic domains ('hotspots') and they represent visual synaptic inputs that are highly tuned for orientation and direction. This protocol describes the experimental procedures for the recording and the analysis of these visually evoked dendritic calcium signals. The key points of this method include delivery of fluorescent calcium indicators through the recording patch pipette, selection of an appropriate optical plane with many dendrites, hyperpolarization of the membrane potential and two-photon imaging. The whole protocol can be completed in 5–6 h, including 1–2 h of two-photon calcium imaging in combination with stable whole-cell recordings.

INTRODUCTION

Mammalian cortical neurons compute sensory information that arrives through numerous synaptic inputs located on their dendrites[1]. To achieve a better understanding of dendritic computation *in vivo*[2–4], it is important to identify and characterize the input signals in the living brain. A fruitful approach to study synaptically evoked dendritic signals is based on the use of fluorescent calcium indicators and on appropriate imaging techniques that allow the recording of the dynamics of intracellular Ca^{2+} concentration in dendrites (reviewed in ref. 5). This approach has been used extensively *in vitro* and has helped to identify synaptically evoked dendritic calcium transients in neurons of many brain regions[5–9]. *In vivo* studies have been restricted mostly to the recording of action potential–related dendritic Ca^{2+} signals[10–16]. However, until recently, the nature of sensory-evoked synaptic input signals in the dendrites of mammalian cortical neurons remained unexplored.

Combined two-photon imaging and whole-cell recordings *in vivo*

Here we describe a protocol for recording visually evoked local dendritic calcium signals in layer 2 and 3 (layer 2/3) neurons of mouse visual cortex *in vivo*[17]. For this purpose, we first established the whole-cell recording configuration with the 'shadow patch' approach[18], using patch pipettes containing the calcium indicator dye Oregon Green BAPTA-1 (OGB-1). We first noticed that action potential firing produced global dendritic calcium signals that were evoked by back-propagating action potentials[13,17,18]. Synaptically evoked dendritic calcium transients, as found in tectal neurons of the tadpole[19], could not be unambiguously identified at normal resting potential involving action potential firing. However, when we hyperpolarized the neuron to prevent action potential firing, we were able to reliably detect localized calcium transients in response to visual stimulation by drifting gratings. Our results indicate that these sensory-evoked dendritic calcium transients are mediated by *N*-methyl-D-aspartate receptor-dependent glutamatergic synapses[17]. Compared with earlier studies involving the loading of calcium indicator dyes though sharp microelectrodes (50–100 MΩ resistance)[10,11], the approach used here is based on the use of whole-cell recordings with low-resistance patch electrodes (6–7 MΩ). Our procedure allows the direct visualization of the targeted cell body before recording[18], a rapid equilibration of the calcium indicator dye within the cell and a reliable control of the membrane potential[20]. A crucial advantage of *in vivo* whole-cell recordings is that they enable stable and long-lasting two-photon imaging of synaptically induced dendritic calcium signals. An alternative approach for imaging dendritic activity, not requiring simultaneous electrical recordings, involves calcium indicator dye loading through electroporation[21,22]. However, this approach does not allow the active hyperpolarization of the neurons, thus making it difficult to isolate the synaptic input–related subthreshold events.

Applications

Our method can be used to perform recordings not only in the visual cortex but also in other brain regions. We have also obtained preliminary results with this method in the auditory, the barrel and the motor cortices, as well as in the cerebellar cortex (Z. Varga, H.J., X.C., N.L.R., A.K., unpublished data). We have applied this method only to mice, but we are confident that it can also be used successfully in other species. Our recordings were all obtained in layer 2/3 cortical pyramidal neurons. However, the method can be adapted easily to other types of neurons (e.g., interneurons).

Current constraints

At present, the method is largely restricted to neurons that are located near the surface (i.e., at a depth of 100–300 μm) of the cortex. Improvements in two-photon microscopy, such as the use of regenerative amplifiers[23], may help for the investigation of dendrites in deeper cortical layers, whereas improved methods of multiphoton endoscopy[24] may provide access to dendrites of neurons in subcortical brain regions. An important open question concerns the precise nature of the sensory inputs to cortical neurons; namely, whether sensory inputs represent individual synapses or rather small clusters of synapses on a dendrite. Finally,

the wide application of the method will decisively benefit from the use of genetically encoded calcium indicators (GECIs)[25–29], although the presently available GECIs are not yet sufficiently sensitive[30] for the detection of calcium signals occurring in small dendritic domains. New GECIs with a higher affinity for calcium may be suitable for dendrite imaging *in vivo*.

MATERIALS

REAGENTS

- Experimental animals. So far, this protocol has been tested only in C57/BL6 mice at the age of postnatal days 28–35 **! CAUTION** All animal experiments must be performed in accordance with the guidelines and regulations of the relevant authorities.
- Isoflurane (Abbott) **! CAUTION** Use strictly in accordance with the specifications of the isoflurane apparatus and maintain proper room ventilation.
- Lidocaine hydrochloride (20 mg ml^{-1}; e.g., Xylocaine, AstraZeneca). Lidocaine HCl is a local anesthetic agent.
- Oregon Green 488 BAPTA-1 hexapotassium salt (OGB-1; Invitrogen, cat. no. O6806). It is a membrane impermeable, calcium sensitive fluorescent indicator.
- Alexa Fluor 594 (Invitrogen, cat. no. A10438). It is a membrane impermeable, inert fluorescent indicator.
- Chemicals for artificial cerebrospinal fluid (ACSF) and patch pipette solution (all from Sigma-Aldrich): NaCl, KCl, $NaHCO_3$, NaH_2PO_4, $CaCl_2$, $MgCl_2$, glucose, KOH, K-gluconate, HEPES, Mg-ATP, Na_2-ATP, Na-phosphocreatine and biocytin.
- Agarose powder (Invitrogen, cat. no. 16500500)
- Borosilicate capillaries (Hilgenberg, cat. no. 1807516)
- Eye protecting cream (Bepanthen, Bayer Vital)
- Cyanoacrylate glue (UHU, UHU)
- Distilled water
- Oxygen supply
- Carbon dioxide supply

EQUIPMENT

- Anesthesia-monitoring system (Powerlab, ADInstruments)
- Warming plate to keep the animal at normal body temperature (home-built; just a plastic plate with a heating wire powered by direct current)
- High-speed two-photon microscope (we use a home-built device. Similar systems are commercially available from several suppliers, including Leica, Nikon, Prairie Imaging and LaVision BioTec). See EQUIPMENT SETUP for details.
- Patch-clamp amplifier (EPC10, HEKA)
- Motorized micromanipulators ('Unit Junior', Luigs & Neumann)
- Pipette puller (PC-10, Narishige)
- Recording chamber with side-access opening: made from a standard tissue-culture dish (**Fig. 1a**)
- Video projector (LT-20, NEC)
- *Software for analysis*: We generated a program, DENDRITE-1, to define regions of interest (ROIs) and to extract calcium signals from these ROIs. This program is freely available on request. The program requires the run-time environment of LabVIEW 8.5 or higher versions. Similar programs may be generated by using other data analysis software packages such as, e.g., Matlab (release 2007b; Mathworks) or WCIF-ImageJ (open source, http://www.uhnresearch.ca/facilities/wcif/fdownload.html). Further statistical analyses are performed using IGOR software (WaveMetrics).
- Isoflurane vaporizer (Drägerwerk)
- Airflow meter (KOBOLD Messring)
- Titanium-sapphire pulsing laser (Chameleon, Coherent; pulse width 140 fs, repetition rate 80 MHz)
- Resonant scanner unit (8 KHz; CRS, Cambridge Technology)
- Commercial microscope chassis (BX51W1, Olympus)
- Photomultiplier tubes (H7422-40, Hamamatsu)
- Microscope objective (long working distance, water immersion, ×40/0.8, WD 3.5 mm; Nikon)

REAGENT SETUP

Artificial cerebrospinal fluid ACSF is composed of NaCl (125 mM), 4.5 mM KCl, 26 mM $NaHCO_3$, 1.25 mM NaH_2PO_4, 2 mM $CaCl_2$, 1 mM $MgCl_2$ and 20 mM glucose; bubble with carbogen (95% O_2 + 5% CO_2). All reagents are dissolved in distilled water, for a total volume of 1 liter. The solution without glucose can be stored for days at 4 °C. **▲ CRITICAL** Glucose is added just before the experiment.

Agarose solution Boil 20 mg of agarose powder in 1 ml of ACSF until it is fully dissolved. Cool the agarose solution to a temperature just below 38 °C before applying it to the cortex. **▲ CRITICAL** Freshly prepare agarose solution just before each experiment.

Patch pipette solution Patch pipette solution consists of K-gluconate (112 mM), 8 mM KCl, 10 mM HEPES, 4 mM Mg-ATP, 0.375 mM Na_2GTP, 10 mM Na-phosphocreatine, 100 µM OGB-1 and 25 µM Alexa-594; pH is adjusted to 7.4 by KOH. All the reagents are dissolved in distilled water.
▲ CRITICAL Freshly prepare the patch pipette solution for each experiment and keep the solution on ice throughout the experiment.

EQUIPMENT SETUP

Isoflurane anesthetic unit It consists of a pure medical oxygen supply, an isoflurane vaporizer, an airflow meter, tubing and a respiration mask.

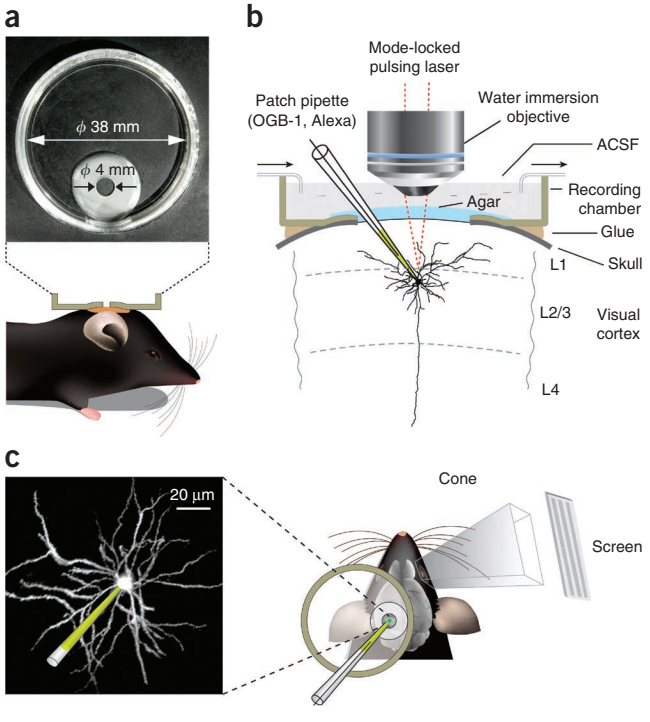

Figure 1 | Experimental arrangement for *in vivo* dendritic imaging in combination with whole-cell recordings. (**a**) Top view of the recording chamber (upper panel). The lower panel schematically shows the recording chamber (side view) fixed on the mouse skull. (**b**) Side view of the experimental arrangement. Note the positions of the dye-containing (OGB-1, Alexa) patch pipette, the water-immersion objective, the agar-covered exposed cortical surface and the recording chamber glued on the skull. Cortical layers 1, 2/3 and 4 are indicated as L1, L2/3 and L4. The arrows indicate the flow direction of the ACSF superfusing the cortical surface. (**c**) Left panel, *z*-projection (along the dorsoventral axis) of *in vivo* two-photon images (from Alexa Fluor 594 fluorescence) of a visual cortical layer 2/3 neuron. The tip of the patch pipette (green) is in contact with the cell body. Right panel, top view of the recording chamber mounted on the skull, the patch pipette and the screen displaying visual stimuli. A black paper cone to prevent stray light is placed between the eye and the screen.

High-speed two-photon laser scanning microscope setup We use a home-built setup that is derived from the designs of Parker/Sanderson (http://parkerlab.bio.uci.edu/microscopy_construction/build_your_own_twophoton_microscope.htm). Excitation light is provided by a titanium-sapphire pulsing laser at a wavelength of 800 nm. A resonant scanner unit is mounted on a commercial microscope chassis. Emitted photons are split into two channels and detected by photomultiplier tubes, i.e., into a 'green' channel for OGB-1 fluorescence (480–560 nm) and a 'red' channel for Alexa Fluor 594 fluorescence (580–680 nm). Standard scanning speed is 30 Hz for a pixel resolution of 480 × 400 or 60 Hz at a reduced frame of 480 × 180. This high scanning speed is beneficial, because it provides the information required for reducing heartbeat-related motion artifacts[16]. We use a long working distance, water immersion microscope objective. The starting trigger of image acquisition is synchronized with the patch-clamp recording and visual stimulation program. *Note*: Most two-photon microscopes equipped with standard galvanometric scanners can also be used for this protocol, because they allow, for smaller-sized frames, sampling rates that are similar to those used for our experiments. In addition, single line-scan imaging may be used, although scanning along the dendritic axis may pose alignment problems because of the unavoidable motions of the brain tissue under *in vivo* recording conditions.

Visual stimulation Visual stimuli are generated by a program written in Matlab with the 'Psychtoolbox' add-on package (http://psychtoolbox.org/wikka.php?wakka=HomePage). A video projector (pixel resolution 1,280 × 1,024; refresh rate 75 Hz) casts the stimuli onto a screen placed at 30 cm from the right eye, covering ~80° × 60° of the visual field. A black paper cone placed between the eye and the screen is used to prevent stray light. Each trial of visual stimulation sequence starts with a gray screen (mean luminance of black and white) for 4 s, followed by eight periods of square-wave grating stimulation, corresponding to eight directions with an angular interval of 45°. Each of these periods consists of a stationary pre-phase of 2 s followed by a drifting stimulation phase for 1 s (spatial frequency 0.03 cycles per degree, drifting speed 1 cycle per s, black/white contrast 80%, mean luminance 3.7 cd m^{-2}).

PROCEDURE

Surgery ● TIMING 60–80 min

1| Anesthetize the mouse with 1.5% isoflurane (vol/vol, in pure O_2).

2| Place the mouse onto a warming plate (38 °C).

3| Gently cover both eyes with eye protecting cream.

4| Inject ~50 µl of lidocaine hydrochloride s.c. above the skull.

5| Using fine scissors, remove the hair and skin above the skull from an area of ~1 cm in diameter above the visual cortex (left hemisphere).

6| Glue the recording chamber (see **Fig. 1**) onto the exposed skull with cyanoacrylate glue.

7| Perform a small rectangular craniotomy (~1 mm × 0.8 mm) above the monocular region of primary visual cortex (left hemisphere), centered at 2.2 mm lateral to the midline and 4 mm posterior to bregma. Be very careful not to damage the cortex.
▲ CRITICAL STEP Keep the dura as intact as possible. An intact dura helps to prevent motion artifacts.

8| Gently clean the exposed cortex with ACSF to remove blood. Usually, craniotomy-induced bleeding stops within 2–3 min.

9| Cover the exposed cortex with agar. First, remove the ACSF from the recording chamber and then put a drop of agarose solution (~38 °C) on top of the exposed cortex and the surrounding skull. Wait until the agarose solution solidifies and then fill the chamber with fresh ACSF.
▲ CRITICAL STEP The agar should form a compact sheet with a thickness of ~1 to 2 mm. For best results, avoid any cracks in the agar.

Preparation for recording ● TIMING 30–40 min

10| Transfer the animal to the recording setup on a warming plate.

11| Start perfusion of the recording chamber with warmed (37 °C) and gassed ACSF.

12| Reduce isoflurane concentration to 1.2% (vol/vol).

13| Remove the protecting cream from the right eye carefully.

14| Mount the black paper cone (for preventing stray light) between the eye and the screen (see EQUIPMENT SETUP and **Fig. 1**).
■ PAUSE POINT In practice, this is the only time point for the experimenter to take a break (~30 min; the subsequent steps (Steps 15–41) must be completed consecutively).

15| Prepare patch pipettes and pipette solution (see REAGENT SETUP for details). Pipette resistance should be 6–7 MΩ.

Shadow patching ● TIMING 10–15 min

16| Move the patch pipette, under visual control, vertically through the agar until it reaches the dura in an area devoid of large blood vessels.

17| Switch to the two-photon imaging mode of visualization, and monitor the pipette in the 'red' channel for Alexa Fluor 594 fluorescence.

▲ **CRITICAL STEP** Until Step 38, use two-photon visualization only when needed. Keep laser power as low as possible to prevent photo-damage of the tissue.

18| Verify that the pipette is not occluded by regularly applying brief and gentle pressure pulses (20–80 mbar). Proceed to the next step if the pipette is free, as indicated by pressure-induced small clouds of fluorescence at the tip. Otherwise, use a new pipette and restart the procedure from Step 16.

19| Penetrate the dura by axially moving the pipette stepwise (~50 μm).

20| Test again for pipette occlusion; if the tip is free, proceed to the next step. Otherwise, retract the pipette back to the surface while applying larger pressure pulses (100–200 mbar), and then repeat Step 19.

▲ **CRITICAL STEP** Do not blow out too much of the pipette solution and keep the pressure pulse short (<1 s). No more than four or five repetitions with a given pipette are recommended.

? TROUBLESHOOTING

21| Navigate through the cortex to layer 2/3: advance the pipette slowly with the guidance of two-photon imaging, and avoid hitting blood vessels and other cell bodies by small lateral movements until the desired depth is reached (150–200 μm).

▲ **CRITICAL STEP** During the intracortical navigation, periodically blow out small amounts of the fluorescent solution from the pipette just enough to see the shadows of cell bodies.

? TROUBLESHOOTING

22| Approach the soma of the closest layer 2/3 neuron from the side. Zoom in (two or three times) until the tip of the pipette and the edge of the cell body become clearly discernable.

23| Apply pressure (50–100 mbar) and advance the pipette tip into the center of cell body. If a 'pit' is seen on the cell body, proceed immediately to the next step; otherwise, retract the pipette and repeat from Step 22.

24| Apply constant negative pressure (−150 mbar) until the seal resistance goes up to >150 MΩ and then release the pressure. Wait until a GΩ seal contact is formed between the tip of the patch pipette and the somatic membrane.

▲ **CRITICAL STEP** In case of failure, slowly retract the pipette completely out of the brain and restart from Step 16. However, after five or six failures, the residual extracellular fluorescence becomes high and it is recommended to restart with a new cortical region.

? TROUBLESHOOTING

25| After the formation of the GΩ seal is complete, reposition the tip to its initial position on the side of cell body.

26| Compensate the pipette capacitance.

27| Establish whole-cell recording mode by applying brief negative pressure pulses in increasing order (from −20 mbar onward) until the patched membrane is ruptured.

28| Compensate the cell capacitance and the series resistance.

Dye loading and whole-cell recording ● TIMING 20–40 min

29| Reduce isoflurane concentration to ~0.8% (vol/vol), the threshold value for anesthesia (respiration rate in the range of 100–130 b.p.m.).

30| Check that series resistance is <40 MΩ and leak current amplitude is <200 pA. If these criteria are not fulfilled, restart from Step 16.

? TROUBLESHOOTING

31| Keep the neuron at resting membrane potential (approximately −65 mV) and switch to the current clamp recording mode.

32| Start the sequence of visual stimuli and record changes in membrane potential.

33| Repeat Step 32 for at least ten trials.

34| Check the pipette position by two-photon visualization and, if necessary, correct for drifts.

35| Check dye loading by two-photon visualization. If, usually after 15–20 min, the contrast between dendrites and background is sufficient (>fivefold) in the 'green' channel, proceed to the next step.
▲ **CRITICAL STEP** It takes 20–40 min for the dye to reach full equilibrium in the dendrites of the cell, depending on the series resistance. If the imaging contrast is still not good enough after troubleshooting, restart from Step 16.
? TROUBLESHOOTING

Dendritic calcium imaging ● TIMING 40–120 min
36| Hyperpolarize the neuron below action potential threshold by holding a negative clamp current and continue as indicated in **Figure 2a**.
▲ **CRITICAL STEP** The required holding current may change over the course of recordings; therefore, adjust it such that the up-state membrane potential is just below action potential threshold (approximately −50 mV).

37| Search for a field of view with many dendrites (**Fig. 2b**).
▲ **CRITICAL STEP** The maximal time and the quality of imaging strongly depend on previous steps (Steps 7, 9, 20, 21 and 24). Within the time of whole-cell recording conditions, several focal planes can be imaged, depending on the purpose of the study. We recommend recording only one neuron per cortical region to avoid the overlap of dendrites belonging to different neurons.
? TROUBLESHOOTING

38| Trigger the visual stimuli presentation, whole-cell recording and two-photon calcium imaging simultaneously.
▲ **CRITICAL STEP** The laser power can be increased to optimize the optical signals.

39| Check and, if necessary, correct slow drifts of the focal plane, then repeat Step 38 for six to ten trials.

40| Move to another area (**Fig. 2c**) and repeat Steps 37–39.
▲ **CRITICAL STEP** Checking the pipette position regularly helps to maintain the quality of whole-cell recordings. Note that phototoxic damage is indicated by local swellings of the illuminated dendrites. We recommend stopping the loop of calcium imaging recordings after three or four cycles (Steps 37–40) and proceeding to the next step.

41| Acquire a *z*-stack of images of the entire neuron (**Fig. 2d**).
▲ **CRITICAL STEP** Do not retract the pipette before this step is completed, even if the whole-cell configuration is lost. Retraction of the pipette may damage the dendrite-containing tissue.

Analysis of dendritic calcium signals and identification of hotspots ● TIMING Hours to days
42| Create an image of ~500 consecutive frames (from OGB-1 'green' channel) and adjust the brightness and the contrast such that the dendrites can be clearly seen, as in **Figure 3a**.

43| Define ROIs that cover all dendrites in the focal plane. Note that **Figure 3b** only shows ROIs for a part of the dendrites.

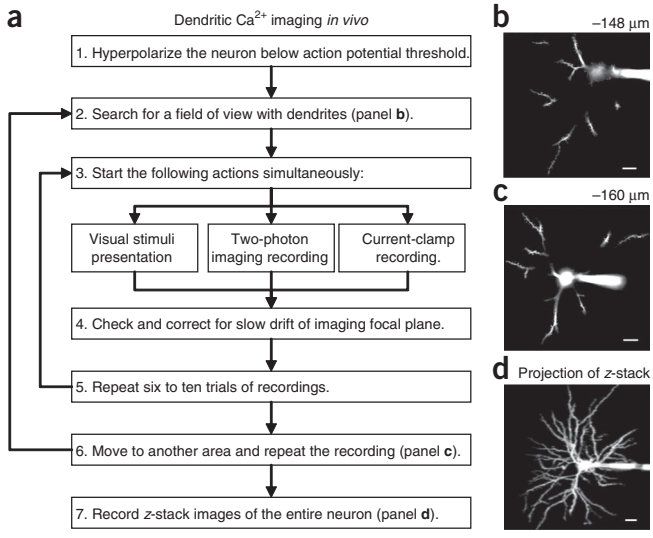

Figure 2 | *In vivo* two-photon imaging of visually evoked dendritic calcium signals. (**a**) Flow diagram showing the different steps of the procedure. (**b**,**c**) Two-photon images (each an average of 500 frames) of a layer 2/3 neuron obtained at different depths under the cortical surface, as indicated. Images were acquired in the 'green channel' for OGB-1 fluorescence. Note the patch pipette on the right side. (**d**) Projection of *z*-stack of two-photon images (Alexa Fluor 594 fluorescence) of the same neuron. Scale bars for **b**–**d**, 10 µm.

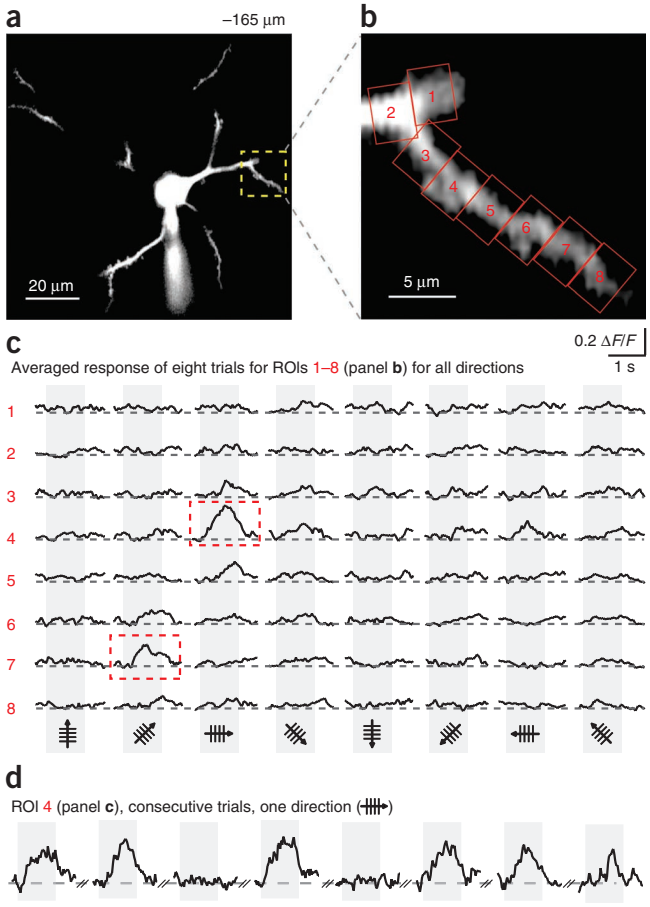

Figure 3 | Extraction of local dendritic calcium transients from two-photon images. (**a**) Image of a focal plane of layer 2/3 obtained at 165 µm below the cortical surface. The image (OGB-1 fluorescence, average of 500 frames) shows a two-photon section through the cell body and dendrites of a neuron, the recording patch pipette and a dashed frame containing a dendritic segment of interest. (**b**) Higher magnification image of the dendritic segment (indicated in panel **a**) covered by eight regions of interest (ROIs), each 3 × 4 µm, used to extract visually evoked local dendritic calcium transients. (**c**) Calcium transients (averages of eight consecutive trials) for all eight ROIs (marked in red) shown in **b**, recorded during the presentation of eight directions of drifting gratings. Two local dendritic calcium transients are highlighted by dashed red frames. The vertical gray bands indicate the time of visual stimulation by the directions schematically indicated at the bottom. (**d**) Consecutive single calcium transients (n = 8) evoked by one direction (as indicated) and recorded in ROI 4 (see **b** and **c**).

44| Calculate changes in fluorescence from each ROI. Refer to **Box 1** for a detailed algorithm.

45| Repeat Steps 42 and 44 for all trials recorded in a focal plane.

▲ **CRITICAL STEP** Use the same set of ROIs (as defined in Step 43) for all trials of a given imaged focal plane. In case of small intertrial image drifts, readjust the position of the ROIs. We recommend discarding trials with large image drifts (>1 µm).

46| Calculate the average calcium signal–corresponding changes in fluorescence from each ROI for each stimulus condition (each direction of drifting gratings) over all recorded trials. Averaged traces are shown in **Figure 3c**.

BOX 1 | CALCULATION OF CALCIUM SIGNALS ($\Delta F/F$) FROM A REGION OF INTEREST

1. Calculate the mean fluorescence $F(t)$ of a region of interest (ROI) for each time point t

   $F(t) = \frac{1}{N}\sum_{\mathrm{ROI}} f_i(t)$, where N is the number of pixels in the ROI, $f_i(t)$ is the value of pixel i at time t.

2. Calculate the time-dependent baseline $F_0(t)$

   For each time point t, taken as the minimum value of smoothed $F(t)$ during a time window before t.

   $F_0(t) = \{\min(\overline{F(x)}) \mid (t-\tau_2) < x < t)\}$

   where $\overline{F(x)} = \frac{1}{\tau_1}\int_{x-\tau_1/2}^{x+\tau_1/2} F(\tau)\mathrm{d}\tau$

3. Calculate the relative change of fluorescence signal $R(t)$ from $F(t)$ and $F_0(t)$

   $R(t) = \frac{F(t)-F_0(t)}{F_0(t)}$

4. Apply noise filtering (exponentially weighted moving average) to get final result $\Delta F/F(t)$

   $\Delta F/F(t) = \frac{\int_0^t R(t-\tau)\cdot w(\tau)\mathrm{d}\tau}{\int_0^t w(\tau)\mathrm{d}\tau}$

   where $w(\tau) = \exp\left\{-\frac{|\tau|}{\tau_0}\right\}$

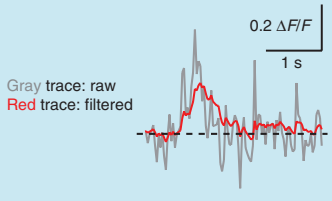

Notes:

1. Typically, effective filtering for 30 Hz imaging is achieved by the following parameters: τ_0 = 0.2 s, τ_1 = 0.75 s and τ_2 = 3 s.
2. This algorithm is robust against both the slow drifting of baseline signal and the fast oscillatory noise due to tissue pulsation, but it may alter the shape of calcium transient, depending largely on τ_0.

47| Identify the hotspots (outlined by red dashed boxes in **Fig. 3c**).
▲ **CRITICAL STEP** Hotspots need to be defined quantitatively (i.e., in terms of variation in signal amplitude) on the basis of the purpose of the study. We accepted a transient hotspot if its amplitude exceeded three times the standard deviation of the noise band.

48| Investigate detailed features of the hotspot signal. For example, determine the reliability of the response to visual stimuli (**Fig. 3d**) and the orientation and direction selectivity of the response[31].

49| Repeat Steps 42–48 for all the imaged focal planes.

? TROUBLESHOOTING

Troubleshooting advice can be found in **Table 1**.

TABLE 1 | Troubleshooting table.

Step	Problem	Possible reason	Solution
20	No spread of fluorescence	Pipette clogged	Retract the pipette from the dura and apply more pressure to the pipette or use a new pipette
21	Cannot see sharp shadows	A thick blood vessel is present above the imaged area	Navigate away from this area
		Too much dye is on the cortical surface (usually happens after many attempts)	Wait for ~30 min and start again from Step 16
24	Cannot achieve GΩ seal	Pipette tip is not clean	Use a new pipette. When navigating the pipette in the cortex, avoid large structures such as blood vessels or cell bodies
30, 35	Series resistance goes up (>40 MΩ)	Pipette tip is pushing too far into the cell body	First, correct the pipette position with two-photon imaging. If the resistance is still high, gently apply a transient negative pressure (10–50 mbar) in the pipette to open more of the patch membrane
	Whole-cell configuration lost after a short time (<1 h)	Movements of the cortical tissue, drift of the pipette	Restart from Step 16 to patch another cell
35	Background is too bright, dendrites cannot be clearly distinguished	Too much dye is spread out during the shadow-patching procedure (usually happens after many attempts)	Wait for a longer time before imaging. If the background is still not fading after ~30 min, start from Step 16 in another region
37	Motion artifacts, image is shaking too much	Proximity of big blood vessels, heartbeat pulsations	Choose dendrites that are far away from the blood vessels

● TIMING

Steps 1–9, Surgery: 60–80 min
Steps 10–15, Preparation for recording: 30–40 min
Steps 16–28, Shadow patching: 10–15 min
Steps 29–35, Dye loading and electrophysiology recording: 20–40 min
Steps 36–41, Dendritic calcium imaging: 40–120 min
Steps 42–49, Analysis: hours to days

ANTICIPATED RESULTS

Data analysis is required to reveal local dendritic calcium signals ('hotspots') evoked by drifting gratings. **Figure 3** illustrates the analysis procedure, as described in Steps 42–49 of the PROCEDURE.

The size and location of the ROIs can vary depending on the purpose of the study. Smaller ROIs give signals that have higher amplitude at the center of the hotspot and also greater noise. Here, we use 3 μm × 4 μm rectangular ROIs that were found to give the best signal-to-noise ratio in our recording conditions. The filtering algorithm (see **Box 1**) was used to reduce noise. Noise consists of normal Gaussian noise as well as a characteristic component at heartbeat frequency (~8 Hz).

The parameters for signal filtering (**Box 1**) were determined empirically to provide good signal preservation as well as effective noise suppression. However, if there is too much movement during imaging recordings (vibration amplitude > 1 μm), the motion artifacts will greatly interfere with the calcium signals and the filter will not help.

ACKNOWLEDGMENTS We are grateful to Y. Kovalchuk for his help in the initial experiments. This study was supported by grants from Deutsche Forschungsgemeinschaft (DFG) to A.K. and from the Friedrich Schiedel Foundation. A.K. is a Carl von Linde Senior Fellow of the Institute for Advanced Study of the Technische Universität München. H.J. and N.L.R. were supported by the DFG (IRTG 1373).

AUTHOR CONTRIBUTIONS H.J., N.L.R., X.C. and A.K. performed the experiments and the analysis. H.J. developed the program for data analysis. A.K. wrote the paper together with H.J., N.L.R. and X.C.

COMPETING FINANCIAL INTERESTS The authors declare no competing financial interests.

Published online at http://www.natureprotocols.com/.
Reprints and permissions information is available online at http://npg.nature.com/reprintsandpermissions/.

1. London, M. & Häusser, M. Dendritic computation. *Annu. Rev. Neurosci.* **28**, 503–532 (2005).
2. Johnston, D. & Narayanan, R. Active dendrites: colorful wings of the mysterious butterflies. *Trends. Neurosci.* **31**, 309–316 (2008).
3. Larkum, M.E. & Nevian, T. Synaptic clustering by dendritic signalling mechanisms. *Curr. Opin. Neurobiol.* **18**, 321–331 (2008).
4. Ohki, K. & Reid, R.C. Specificity and randomness in the visual cortex. *Curr. Opin. Neurobiol.* **17**, 401–407 (2007).
5. Bloodgood, B.L. & Sabatini, B.L. Ca^{2+} signaling in dendritic spines. *Curr. Opin. Neurobiol.* **17**, 345–351 (2007).
6. Yuste, R. & Denk, W. Dendritic spines as basic functional units of neuronal integration. *Nature* **375**, 682–684 (1995).
7. Müller, W. & Connor, J.A. Dendritic spines as individual neuronal compartments for synaptic Ca^{2+} responses. *Nature* **354**, 73–76 (1991).
8. Eilers, J., Augustine, G.J. & Konnerth, A. Subthreshold synaptic Ca^{2+} signalling in fine dendrites and spines of cerebellar Purkinje neurons. *Nature* **373**, 155–158 (1995).
9. Häusser, M. & Mel, B. Dendrites: bug or feature? *Curr. Opin. Neurobiol.* **13**, 372–383 (2003).
10. Svoboda, K., Denk, W., Kleinfeld, D. & Tank, D.W. *In vivo* dendritic calcium dynamics in neocortical pyramidal neurons. *Nature* **385**, 161–165 (1997).
11. Helmchen, F., Svoboda, K., Denk, W. & Tank, D.W. *In vivo* dendritic calcium dynamics in deep-layer cortical pyramidal neurons. *Nat. Neurosci.* **2**, 989–996 (1999).
12. Murayama, M. *et al.* Dendritic encoding of sensory stimuli controlled by deep cortical interneurons. *Nature* **457**, 1137–1141 (2009).
13. Waters, J., Larkum, M., Sakmann, B. & Helmchen, F. Supralinear Ca^{2+} influx into dendritic tufts of layer 2/3 neocortical pyramidal neurons *in vitro* and *in vivo*. *J. Neurosci.* **23**, 8558–8567 (2003).
14. Waters, J. & Helmchen, F. Boosting of action potential backpropagation by neocortical network activity *in vivo*. *J. Neurosci.* **24**, 11127–11136 (2004).
15. Svoboda, K., Helmchen, F., Denk, W. & Tank, D.W. Spread of dendritic excitation in layer 2/3 pyramidal neurons in rat barrel cortex *in vivo*. *Nat. Neurosci.* **2**, 65–73 (1999).
16. Helmchen, F. & Waters, J. Ca^{2+} imaging in the mammalian brain *in vivo*. *Eur. J. Pharmacol.* **447**, 119–129 (2002).
17. Jia, H., Rochefort, N.L., Chen, X. & Konnerth, A. Dendritic organization of sensory input to cortical neurons *in vivo*. *Nature* **464**, 1307–1312 (2010).
18. Kitamura, K., Judkewitz, B., Kano, M., Denk, W. & Häusser, M. Targeted patch-clamp recordings and single-cell electroporation of unlabeled neurons *in vivo*. *Nat. Methods* **5**, 61–67 (2008).
19. Bollmann, J.H. & Engert, F. Subcellular topography of visually driven dendritic activity in the vertebrate visual system. *Neuron* **61**, 895–905 (2009).
20. Margrie, T.W., Brecht, M. & Sakmann, B. *In vivo*, low-resistance, whole-cell recordings from neurons in the anaesthetized and awake mammalian brain. *Pflugers Arch.* **444**, 491–498 (2002).
21. Nevian, T. & Helmchen, F. Calcium indicator loading of neurons using single-cell electroporation. *Pflugers Arch.* **454**, 675–688 (2007).
22. Nagayama, S. *et al. In vivo* simultaneous tracing and Ca^{2+} imaging of local neuronal circuits. *Neuron* **53**, 789–803 (2007).
23. Theer, P., Hasan, M.T. & Denk, W. Two-photon imaging to a depth of 1000 microm in living brains by use of a Ti:Al2O3 regenerative amplifier. *Opt. Lett.* **28**, 1022–1024 (2003).
24. Jung, J.C. & Schnitzer, M.J. Multiphoton endoscopy. *Opt. Lett.* **28**, 902–904 (2003).
25. Mank, M. & Griesbeck, O. Genetically encoded calcium indicators. *Chem. Rev.* **108**, 1550–1564 (2008).
26. Hires, S.A., Tian, L. & Looger, L.L. Reporting neural activity with genetically encoded calcium indicators. *Brain Cell. Biol.* **36**, 69–86 (2008).
27. Miyawaki, A. Fluorescence imaging of physiological activity in complex systems using GFP-based probes. *Curr. Opin. Neurobiol.* **13**, 591–596 (2003).
28. Lutcke, H. *et al.* Optical recording of neuronal activity with a genetically-encoded calcium indicator in anesthetized and freely moving mice. *Front. Neural. Circuits* **4**, 9 (2010).
29. Tian, L. *et al.* Imaging neural activity in worms, flies and mice with improved GCaMP calcium indicators. *Nat. Methods* **6**, 875–881 (2009).
30. Rochefort, N.L. & Konnerth, A. Genetically encoded Ca^{2+} sensors come of age. *Nat. Methods* **5**, 761–762 (2008).
31. Niell, C.M. & Stryker, M.P. Highly selective receptive fields in mouse visual cortex. *J. Neurosci.* **28**, 7520–7536 (2008).

4 A deeper analysis: Dendritic coding of multiple sensory inputs in single cortical neurons *in vivo*

Background

The first finding of sensory evoked dendritic input sites in cortical neuron in vivo, as described in chapter 2, has attracted lots of interests and many open questions were raised. One important concern was that the mouse visual cortex is not organized in orientation-specific columns like higher mammals such as cats or primates. Therefore the finding of salt-&-pepper like organization of orientation-tuned inputs might simply have been due to the lack of topographical columnar structure. In the comment letter by Priebe and Ferster for the Nature article (Nature 464 (7293):1290-1), it has been conceived that in the orientation column of visual cortex of higher mammals, neurons may receive predominantly inputs of one orientation. Also, near the pinwheel center, inputs from multiple orientation columns may be arranged in topographical order.

However, such experiments in higher mammals had not been established yet. Therefore, to address the concern of columnar structures, Prof. Bert Sakmann suggested doing similar experiments on the mouse barrel cortex, which had been very well known for its barrel-like columns mapping the sensation of each individual whisker. The study was performed in collaboration with Zsuzsanna Varga on a newly built setup equipped with 12 kHz resonant scanner. A unique feature of this setup was that it had a custom-built intrinsic optical imaging system that is mounted on the same optical axis of the two-photon microscope, thus allowing accurately targeted patching in cortical column area mapped to specific whisker, as described in the “Text S1” part in the original manuscript. A novel theoretical model was devised and well combined with the analysis of experimental data, as presented in the “Text S2” part of the manuscript. In short, this work was an effort to combine the novel *in vivo* physiological experimental data at cellular and sub-cellular level with as well novel methods of machine learning, to achieve a more comprehensive understanding of cortical neuronal information processing.

Biological Sciences / Neuroscience

Dendritic coding of multiple sensory inputs in single cortical neurons in vivo

Zsuzsanna Varga[1], Hongbo Jia[1], Bert Sakmann and Arthur Konnerth[2]

Institute of Neuroscience and Institute for Advanced Study, Technical University Munich, Biedersteinerstr. 29, 80802, Munich, Germany

[1]These authors contributed equally to this work

[2]**Corresponding author:** Arthur Konnerth, Institute of Neuroscience, Technical University Munich, Biedersteinerstr. 29, 80802, Munich, Germany, Tel.: +49 - (0)89-4140 3351, Fax: +49 - (0)89-4140 3352, e-mail: arthur.konnerth@lrz.tu-muenchen.de

Author contributions: A. K and B.S. designed research, Z. V. and H. J. performed the experiments, Z. V. and H. J. analyzed data, A.K. wrote the paper with the help of other authors.

The authors declare no conflict of interest.

Abstract

Single cortical neurons in the mammalian brain receive signals arising from multiple sensory input channels. Dendritic integration of these afferent signals is critical in determining the amplitude and time course of the neurons' output signals. As of yet, little is known about the spatial and temporal organization of converging sensory inputs. Here, we combined in vivo two-photon imaging with whole-cell recordings in layer 2 neurons of the mouse vibrissal cortex as a means to analyze the spatial pattern of subthreshold dendritic calcium signals evoked by the stimulation of different whiskers. We demonstrate that the principal whisker and the surround whiskers can evoke dendritic calcium transients in the same neuron. Distance-dependent attenuation of dendritic calcium transients and the corresponding subthreshold depolarization suggest feedforward activation. We found that stimulation of different whiskers produced multiple calcium hotspots on the same dendrite. Individual hotspots were activated with low probability in a stochastic manner. We demonstrate that these hotspots are generated by calcium signals arising in dendritic spines. Some spines were activated uniquely by single whiskers, but many spines were activated by multiple whiskers. These shared spines indicate the existence of presynaptic 'feeder' neurons that integrate and transmit activity arising from multiple whiskers. Despite the dendritic overlap of whisker-specific and shared inputs, different whiskers are represented by a unique set of activation patterns within the dendritic field of each neuron.

Introduction

Cortical function relies on the network properties of connected neurons. In addition to conventional (1) and modern (2-4) structural reconstructions, electrophysiological (5, 6) and optical tools (7-10) are commonly applied to probe the functional connectivity among neurons. Recent advances in two-photon calcium imaging enabled an in vivo analysis of the dendritic organization of sensory inputs to layer 2/3 neurons in the mouse visual cortex (11). The sensory input sites were represented by local dendritic calcium influx via NMDA receptors, called hotspots. The fine structure of the hotspots, whether they represented individual spines or small spino-dendritic segments, was not determined. A major finding was that synaptic inputs sharing the same orientation preference are widely distributed throughout the dendritic field, and, importantly, inputs with different orientation preference are interspersed. An important open question is whether the presence of such inputs with multiple orientations is related to the fact that, in the mouse visual cortex, neurons selective to different orientations are interspersed (12) rather than being organized into cortical columns. It has been suggested that in the cat and in primates the input connection scheme would be differently organized (13), because neurons with different orientation preferences are quite strictly clustered into orientation columns (14). It is thus unclear how in vivo inputs are organized on the dendrites of single cortical neurons residing in a columnarly structured region.

A study on dendritic organization of inputs in the mouse visual cortex by Jia et al. (11) had focused on the signals arising through a single input channel, i.e., a single eye. However, sensory systems generally integrate information from multiple peripheral anatomical input channels (15). For example, the rodent vibrissal cortex integrates information arising from multiple whiskers. It is a widely used model system for studying the function of cortical columns due to the precise relation between barrels, which are easily visualized through histological staining, and the functional representation of single whiskers (16). However, the representation of whiskers by single barrels is not exclusive. In fact, neurons in a single barrel column can have a subthreshold receptive field comprising several whiskers (17-26). For example, layer 2/3 neurons respond to the stimulation of the principle whisker (PW) and multiple surround whiskers (SW) (27). In addition, stimulation of a single whisker results in a spread of activation through large areas of the barrel cortex (28, 29).

In this study we investigated how inputs reaching layer 2/3 through two different cortical columns are represented on the dendrites of single layer 2 neurons. We analyzed the distance dependence of changes in subthreshold membrane potential and global dendritic calcium signaling upon SW stimulation. We compared the number, spatial distribution, and response probability of input sites activated by stimulation of PW and SW. We applied a similarity-based classifier to distinguish the activation patterns of each trial. Furthermore, we used high-resolution imaging on short dendritic segments to study the fine structure of dendritic input sites down to the single spine level.

Results

Spatial and temporal organization of dendritic hotspots. We investigated the functional properties of layer 2 neurons with combined whole-cell recordings and two-photon dendritic calcium imaging in the vibrissal cortex of mice in vivo (Fig. 1A). Two whiskers in different configurations (C2 and either E2, D2, C4 or C1) were spared while all others were acutely trimmed. The topographically related cortical columns for the spared whiskers were located by intrinsic signal optical imaging (30) (Fig. 1B). We made targeted whole-cell recordings from neurons in the C2 whisker-related column. Thus, with reference to the neuron, C2 was denoted as the PW and the other whisker was denoted as the SW. For each recorded neuron, two-photon calcium imaging was performed in 6-11 focal planes (Fig. 1C, see also ref (31), covering a substantial fraction of dendrites (up to 20-30 % of the dendritic tree, Fig. 1D). During combined two-photon calcium imaging and recordings of subthreshold responses, neurons were prevented from action potential firing, if necessary, by slightly hyperpolarizing the membrane potential (about 2-10 mV). Importantly, even with the hyperpolarization, the membrane potentials were in the normal range of resting potentials that are encountered in neurons of layer 2/3 in the rodent barrel cortex (-85 to -60 mV, see ref (32)).

In neurons located either proximal or more distal to the SW-related column (Fig. 1E), we found that both PW and SW stimulation evoked subthreshold membrane potential depolarization (Fig. 1F) and dendritic calcium transients (Fig. 1G). To compare whisker-evoked depolarization with the set of inputs arriving at a single neuron, we calculated the global subthreshold dendritic calcium signal from all trials at all focal planes for each whisker (Fig. 1H). This global calcium signal represents an integration of dendritic hotspot signals that are activated by sensory stimulation and is a measure of the afferent synaptic input (11). A ‘distant’ SW evoked a smaller depolarization and smaller global dendritic calcium signal compared to the PW, while the responses evoked by a ‘proximal’ SW were similar to those of the PW. This suggests that the distance-dependent weakening of SW responses is due to the gradual reduction in afferent input. To test the generality of this trend, we calculated the relative differences between PW and SW evoked depolarizations and dendritic calcium signals for 12 neurons (Fig.1 I-J). All variables (distance, depolarization and dendritic calcium signal) showed significant pairwise correlation (Pearson correlation): depolarization versus distance ($r=0.66$, $p=0.03$), dendritic calcium versus distance ($r=0.62$, $p=0.04$), depolarization versus dendritic calcium ($r=0.62$, $p=0.03$). Overall, these results suggest an inverse relationship between the SW-to-PW distance and the strength of SW input to the PW column.

Next, we characterized the individual local dendritic calcium signals (i.e., hotspots, see also (11)) evoked by whisker stimulation. Typically, several dendrites were visible in one focal plane (Fig. 2A), and multiple hotspots were encountered on one dendrite (Fig. 2B). To test the response probability of individual hotspots, we examined the same dendritic region repeatedly (Fig 2C). The individual hotspot sites were activated at low probabilities (temporal stochasticity) (Fig 2D, E) and with different patterns of hotspot distribution across trials (spatial stochasticity). We found that the response probability distributions for PW- and SW-evoked hotspots were similar (Fig. 2F).

To compare the PW- and SW-evoked patterns, we mapped all hotspot sites weighted with their response probabilities in each focal plane for PW and SW trials separately (Fig. 3A-B). Then, the PW- and SW-evoked patterns were superimposed, so that PW-specific and SW-specific hotspot sites were distinguished. Surprisingly, a large fraction of hotspot sites were shared (activated by both whiskers) (Fig. 3C), especially when the SW column was located at a short distance from the recorded neuron (Fig. 3D, E).The whisker-specific and shared hotspot sites were intermingled. However, the number of both SW-specific and shared hotspot sites decreased with the distance between the neuron and the SW-related column center (Fig. 3D, E, the Pearson correlation coefficients for number of hotspots versus distance were as follows: PW-specific, r=0.26, p=0.42, SW-specific, r=-0.72, p=0.008, shared, r = -0.72, p=0.009).

Distinct sets of input patterns of different whiskers in single neurons. In view of the low probability and stochastic activation pattern of specific and shared input sites, we wondered whether PW or SW stimulation produced whisker-specific input patterns during each single trial. To address this issue, we devised a simple classifier to compare dendritic activation patterns without bias. For this purpose, the raw two-photon images were convolved with spatial and temporal filters, transformed into a new sequence of Δf/f images representing the relative fluorescence change of each pixel (see Text S1 section 7). A threshold-based event detector screened the Δf/f images, registered the hotspot events and projected the pixels onto one binary image defining the activation pattern of this trial. Using normalized image cross-correlation we then calculated the correlation coefficient between any two trials of the same focal plane (Fig. S1A, Text S1 section 7). We refer to this coefficient as the similarity index, in line with the terminology used in automated pattern recognition (33). Fig. 3F illustrates the results obtained from a single neuron and shows that the similarity indices among trials of the same whisker were higher (33.6±0.3%, n=1620) than among trials of different whiskers (28.3±0.3%, n=900, unpaired t-test $p<0.0001$). Similar results were obtained for all 12 neurons (Fig. 3G), regardless of their distance to the SW-barrel center (each shows a significant difference $p<0.0001$). For a given trial, the “Mean PW-similarity” and “Mean SW-similarity” was defined as the average of similarity indices between the trial and all other PW trials and SW trials, respectively. The classifier can distinguish between PW and SW trials by judging whether the mean PW-similarity value was higher or lower than the mean SW-similarity value. Such a correct judgment of a trial means that in Fig. 3F-G, a blue dot is above the diagonal line or a red dot is below the diagonal line. For many focal planes the classifier performed well above chance level (Fig. S1B) with a cumulative success rate of more than 90% over the whole dataset. These results indicate that different whiskers had distinct sets of dendritic activation patterns. In a detailed numerical model (see Text S2) we generalized this observation for an indefinite number of trials. The model also predicts that our limited number of trials (10 for each whisker) were sufficient for the classifier to correctly distinguish the two sets of dendritic activation patterns evoked by PW and SW stimulation.

Multiple input channels converge on single spines. What is the fine anatomical structure of the shared dendritic hotspots? We considered two alternative hypotheses: first, separate inputs from the PW and a SW may contact distinct nearby spines on the same dendrite or, second, the same spines may be activated by both the PW and at least one SW. While our initial procedure of in vivo dendritic imaging was useful for monitoring local signaling in larger dendritic fields (11, 31), it did not provide sufficient digital image resolution to resolve these issues. For higher resolution recordings of whisker stimulation evoked calcium transients, we used the low power temporal oversampling (LOTOS) procedure which involves imaging at high frame rates (200 Hz) and lower excitation intensity per frame (see Text S1 section 6, and ref (*34*)). With LOTOS, which helps to reduce photodamage when imaging at high zoom factors, we were able to image portions (10-20 µm) of spiny dendrites (Fig. 4A-C) and to record whisker stimulation-evoked calcium transients during repeated trials (Fig. 4D, E). The recordings revealed calcium transients in single spines, with small or absent signals in the parent dendritic shaft (Fig. 4D, E, S2). Importantly, the recordings demonstrated that, in addition to whisker-specific spines, some spines were reliably activated by both whiskers (Fig. 4E, F), providing direct support for our second hypothesis that the same spines can be activated by both PW and SW.

Discussion

In this study we combined two-photon calcium imaging and whole-cell recording in vivo to examine the dendritic activation patterns in single neurons of the vibrissal cortex when activating distinct whiskers. From previous studies it is known that the receptive field of single layer 2 neurons comprises not only the PW, but also multiple SWs (24). However, the electrical responses evoked by SW stimulation decrease as the distance between SW and PW increases (*27, 29*). When analyzing subthreshold dendritic calcium transients representing synaptic input sites, we also found that dendritic calcium responses evoked by SW stimulation decrease as the distance between SW and PW increases. Thus, our results suggest that the distance-dependent attenuation of electrical responsiveness is supported by a feed-forward connection scheme with a likely contribution of inhibitory inputs (35-37).

The whisker stimulation-evoked local dendritic calcium signals (hotspots) found in this study shared similarities with the previously reported dendritic hotspots found in visual cortex (11). In general, however, the density of hotspots on a dendrite that were activated by the stimulation of a whisker was substantially higher than in dendrites of visual cortex neurons when activated by a specific stimulus feature, such as a particular direction of a drifting grating stimulation. This difference may result from the difference in the mode of sensory stimulation. A remarkable feature of the dendritic organization of hotspots in the dendrites of layer 2 vibrissal cortex neurons was that most individual input sites were activated at low probability for both PW and SW stimulation. The resonant scanner-based two-photon imaging approach used in this study allowed the simultaneous imaging of hotspots in several dendrites

across a relatively large field of view. However, spine imaging requires high zoom factors and, furthermore, image acquisition at high frame rates (200 frames/s in our case) at a reduced excitation power (for details see LOTOS procedure in Methods and in ref. (34)). As the speed of the scanning laser beam cannot be increased in a resonant scanner-based system, this led to a further reduction of the effective field of view, such that in practice only segments of spiny dendrites of up to 10 – 20 um length were used for spine imaging. The whisker-evoked calcium transients recorded in such spiny dendrites demonstrated that the largest calcium transients occurred invariably in spines, with significantly smaller contributions in the adjacent dendritic shafts. In fact, in about 2/3 of the local response, calcium signaling was exclusively detected in the spines but not the adjacent dendrite (Fig. S2). These results do not provide support for the generation of local dendritic regenerative events like dendritic spikes (38). Instead, they indicate that the 'computational unit' (39) of dendrites are single active spines. These recordings, however, do not exclude the possibility that during other conditions of sensory activation (e.g. active whisking in awake animals) this and other types of cortical neurons, e.g., the large layer 5 pyramidal cells, have different signaling modes in their dendrites, especially in the remote apical tufts (40).

The results demonstrate that spines in the same neuron were activated either by the PW or by a SW. However, a surprising observation was that some of the spines were activated by both whiskers. The identification of such shared synaptic input sites strongly suggests the existence of intermediary 'feeder' neurons, capable of firing action potentials in response to both PW and SW stimulation. Based on previous anatomical studies (5, 41), it seems that layer 2/3 pyramidal neurons represent a major fraction of these feeder neurons (Fig 4L). Furthermore, action potential activity in layer 2/3 neurons is typically evoked by both PW and SW deflection (21, 27, 42). In fact, the number of action potentials evoked by proximal SW-deflection can be almost as high as that evoked by PW-deflection. Moreover, action potential numbers fall off gradually with deflection of the more distant SWs (27). Additional support for an involvement of layer 2/3 neurons, known to be strongly interconnected with each other (5, 6), comes from our own recordings showing that each recorded neuron received strong inputs from both the PW and the SW and, therefore, could act itself as a feeder neuron. Furthermore, smaller contributions may come from neurons, with multi-whisker receptive fields, that are located in other cortical layers. Such neurons have been found in layer 4 (17-22, 24), layer 5B and to a lesser extent layer 5A (23-25). For simplicity, in our model we considered only the presumably strongest input, which arises from layer 2/3 neurons.

In conclusion, in contrast to the topographically well-organized macroscopic cellular structure of 'barrel columns', we found that the dendritic organization of single spine synaptic inputs is surprisingly unstructured, with a salt-and-pepper like distribution of intermingled inputs from multiple whiskers impinging on the same dendrites. On a trial-by-trial basis, most of the functional input sites were activated randomly at low probabilities. However, when viewing the pool of dendritic inputs as an ensemble, the set of activation patterns were distinct for different whiskers. Taken together, our results provide basic

insights into the dendritic arrangement of sensory signals arising from different input channels onto single neurons of a columnarly organized cortical region.

Materials and methods

Animals. All experimental procedures were performed in accordance with institutional animal welfare guidelines and were approved by the state government of Bavaria, Germany. C57BL/6 mice (P28-38, n=16) were used for in vivo dendrite and spine imaging experiments. Animal preparation procedures were the same as those previously described (31), except for the treatment of whiskers. With the exception of 2 whiskers (C2 and either E2, D2, C4 or C1) on the right side, all other whiskers were plucked. The spared whiskers were shortened to 1 cm and were inserted into two glass capillaries which could be separately deflected by piezoelectric actuators to approximately 30˚ in rostrocaudal direction. A pulse stimulator (Model 2100, A-M systems) delivered for each trial a train of voltage pulses (10 pulses, 50 ms, 10 Hz) driving the piezoelectric actuators. In each trial only one whisker was stimulated.

Intrinsic signal optical imaging. The location of the barrel columns related to the spared whiskers was mapped on the cortex by intrinsic signal optical imaging through the intact skull. Images were acquired at 10 Hz by a custom-made system. Each image was spatially filtered by a Gaussian kernel of 5x5 pixels. Image acquisition protocol consisted of two 1s acquisition periods that were repeated 10 times. The first acquisition period was just after the offset of whisker stimulation, the second one (baseline) was at 16 s after the stimulation. Relative reflectance changes were calculated as the summed images acquired during stimulation divided by the summed baseline images. The two whiskers were mapped in consecutive sessions.

Whole-cell recording. Having the two whisker-related barrels mapped by intrinsic signal optical imaging, whole-cell configuration was established on a layer 2 neuron in one of the barrel columns (principal whisker (C2) - related barrel). Patch pipettes with resistances of 5-8 MΩ were pulled from borosilicate glass capillaries on a vertical puller (PC-10, Narishige). The pipette solution contained 112 mM K-gluconate, 10 mM HEPES, 8 mM KCl, 10 mM Na-phosphocreatine, 4 mM Mg-ATP, 0.3 mM Na_2-GTP , 100 µM Oregon Green 488 BAPTA-1 hexapotassium salt (denoted as “OGB1”), 25 µM Alexa Fluor 594 hydrazide sodium salt (denoted as “Alexa”). Current-clamp recordings were acquired with an EPC-9 HEKA amplifier using the software package Pulse. Signals were filtered at 3 kHz and digitized at 10 kHz. Series resistances ranged from 20-60 MΩ. The exact location of the neuron was determined post-hoc by epifluorescence imaging and marked on the map of barrels aligned on the blood vessels (Fig. 1E).

Two-photon calcium imaging of dendritic hotspots and spines. Two-photon calcium imaging was performed on a custom built setup which was similar to that used in a previous study (11). A resonant scanner unit (GSI Lumonics) including one fast axis of a 12 kHz resonant mirror and one slow axis of a

standard galvanometric mirror was mounted on upright microscope chassis (BX51, Olympus) with a long working distance water-immersion objective (Nikon 40x/0.8). Fluorescent excitation light was delivered by a pulsing infrared laser (wavelength 800 nm, pulse width 100 fs, repetition rate 80 MHz) equipped with a pre-chirper (model 'DeepSee", Spectra-Physics). Laser power under the objective was typically 30-40 mW and 15-25 mW, during dendritic hotspot and spine imaging, respectively. Full frame images consisted of 512 lines, and were scanned with a 40 Hz repetition rate. For dendritic hotspot imaging, neurons were imaged in 6-11 focal planes distributed across the whole depth of the dendritic tree. The actual width of the field-of-view, controlled by the amplitude of scanning mirror rotation, ranged between 80-250 µm, depending on the layout of dendrites in the focal plane. For spine imaging, we used the low power temporal oversampling (LOTOS) procedure (34). The scanner was configured for the following mode: the number of lines was reduced to 64, the number of pixels in each line reduced to 256, and the image repetition rate increased to 200 Hz. The width of the field-of-view was accordingly reduced to the range of 27-42 µm. Each focal plane was probed with 10 trials of PW and 10 trials of SW stimulation. Trials were interlaced (5 PW trials followed by 5 SW trials, repeated twice) with variable time intervals (10-20s) between two consecutive trials. For display purposes (Fig. 2C-E; and for spines, Fig.4D-E), the trials with the same whisker stimulation were grouped together. Z-stack images of the neurons were taken at the largest possible field-of-view (300 µm x 300 µm) with a step size 0.5 µm. Z-stack images of spines were taken with the reduced field-of-view and a step size 0.2 µm

Data analysis. The structural reconstruction was performed using the WCIF-ImageJ software (open-access from http://www.uhnresearch.ca/facilities/wcif/imagej/), the whole-cell recordings were analyzed in Igor (Igor Pro v5.0.1.0, Wavemetrics Inc.) and the calcium imaging recordings were analyzed by custom-written programs in LabVIEW (version 2009, National Instruments). Statistical tests were performed in SPSS (version 17.0, IBM). Z-stack images of spines were deconvolved in Huygens (version J27.14, Scientific Volume Imaging BV) and volume rendered in Amira (version 5.3.3, Visage Imaging Inc.). For a detailed description of the algorithms used in the data analysis, see online supporting materials.

Acknowledgements

We thank Jia Lou for excellent technical assistance with the figures. We thank Drs. Fitzpatrick, Schummers, Christie, Nelken and Hill for critically reading early versions of our manuscript. This work was supported by Deutsche Forschungsgemeinschaft (IRTG 1373), the ERA-Net Program, the Center for Integrated Protein Science Munich and the Schiedel Foundation.

References

1. Cajal, S. R. y. (1994) *Histology of the Nervous System of Man and Vertebrates* (Oxford University Press).
2. Lichtman, J. W., Livet, J., & Sanes, J. R. (2008) A technicolour approach to the connectome. *Nature reviews* **9,** 417-422.
3. Denk, W. & Horstmann, H. (2004) Serial block-face scanning electron microscopy to reconstruct three-dimensional tissue nanostructure. *PLoS biology* **2,** e329.
4. DeFalco, J., Tomishima, M., Liu, H., Zhao, C., Cai, X., Marth, J. D., Enquist, L., & Friedman, J. M. (2001) Virus-assisted mapping of neural inputs to a feeding center in the hypothalamus. *Science* **291,** 2608-2613.
5. Feldmeyer, D., Lubke, J., & Sakmann, B. (2006) Efficacy and connectivity of intracolumnar pairs of layer 2/3 pyramidal cells in the barrel cortex of juvenile rats. *The Journal of physiology* **575,** 583-602.
6. Lefort, S., Tomm, C., Floyd Sarria, J. C., & Petersen, C. C. (2009) The excitatory neuronal network of the C2 barrel column in mouse primary somatosensory cortex. *Neuron* **61,** 301-316.
7. Boyden, E. S., Zhang, F., Bamberg, E., Nagel, G., & Deisseroth, K. (2005) Millisecond-timescale, genetically targeted optical control of neural activity. *Nature neuroscience* **8,** 1263-1268.
8. Nikolenko, V., Poskanzer, K. E., & Yuste, R. (2007) Two-photon photostimulation and imaging of neural circuits. *Nature methods* **4,** 943-950.
9. Petreanu, L., Mao, T., Sternson, S. M., & Svoboda, K. (2009) The subcellular organization of neocortical excitatory connections. *Nature* **457,** 1142-1145.
10. Shepherd, G. M. & Svoboda, K. (2005) Laminar and columnar organization of ascending excitatory projections to layer 2/3 pyramidal neurons in rat barrel cortex. *J Neurosci* **25,** 5670-5679.
11. Jia, H., Rochefort, N. L., Chen, X., & Konnerth, A. (2010) Dendritic organization of sensory input to cortical neurons in vivo. *Nature* **464,** 1307-1312.
12. Ohki, K. & Reid, R. C. (2007) Specificity and randomness in the visual cortex. *Current opinion in neurobiology* **17,** 401-407.
13. Priebe, N. J. & Ferster, D. (2010) Neuroscience: Each synapse to its own. *Nature* **464,** 1290-1291.
14. Hubel, D. H. & Wiesel, T. N. (1962) Receptive fields, binocular interaction and functional architecture in the cat's visual cortex. *The Journal of physiology* **160,** 106-154.
15. Celikel, T. & Sakmann, B. (2007) Sensory integration across space and in time for decision making in the somatosensory system of rodents. *Proceedings of the National Academy of Sciences of the United States of America* **104,** 1395-1400.

16. Woolsey, T. A. & Van der Loos, H. (1970) The structural organization of layer IV in the somatosensory region (SI) of mouse cerebral cortex. The description of a cortical field composed of discrete cytoarchitectonic units. *Brain research* **17,** 205-242.
17. Armstrong-James, M. & Callahan, C. A. (1991) Thalamo-cortical processing of vibrissal information in the rat. II. spatiotemporal convergence in the thalamic ventroposterior medial nucleus (VPm) and its relevance to generation of receptive fields of S1 cortical "barrel" neurones. *The Journal of comparative neurology* **303,** 211-224.
18. Armstrong-James, M., Callahan, C. A., & Friedman, M. A. (1991) Thalamo-cortical processing of vibrissal information in the rat. I. Intracortical origins of surround but not centre-receptive fields of layer IV neurones in the rat S1 barrel field cortex. *The Journal of comparative neurology* **303,** 193-210.
19. Armstrong-James, M., Fox, K., & Das-Gupta, A. (1992) Flow of excitation within rat barrel cortex on striking a single vibrissa. *Journal of neurophysiology* **68,** 1345-1358.
20. Brecht, M. & Sakmann, B. (2002) Dynamic representation of whisker deflection by synaptic potentials in spiny stellate and pyramidal cells in the barrels and septa of layer 4 rat somatosensory cortex. *The Journal of physiology* **543,** 49-70.
21. de Kock, C. P., Bruno, R. M., Spors, H., & Sakmann, B. (2007) Layer- and cell-type-specific suprathreshold stimulus representation in rat primary somatosensory cortex. *The Journal of physiology* **581,** 139-154.
22. Hirata, A. & Castro-Alamancos, M. A. (2008) Cortical transformation of wide-field (multiwhisker) sensory responses. *Journal of neurophysiology* **100,** 358-370.
23. Manns, I. D., Sakmann, B., & Brecht, M. (2004) Sub- and suprathreshold receptive field properties of pyramidal neurones in layers 5A and 5B of rat somatosensory barrel cortex. *The Journal of physiology* **556,** 601-622.
24. Moore, C. I. & Nelson, S. B. (1998) Spatio-temporal subthreshold receptive fields in the vibrissa representation of rat primary somatosensory cortex. *Journal of neurophysiology* **80,** 2882-2892.
25. Wright, N. & Fox, K. (2010) Origins of cortical layer V surround receptive fields in the rat barrel cortex. *Journal of neurophysiology* **103,** 709-724.
26. Zhu, J. J. & Connors, B. W. (1999) Intrinsic firing patterns and whisker-evoked synaptic responses of neurons in the rat barrel cortex. *Journal of neurophysiology* **81,** 1171-1183.
27. Brecht, M., Roth, A., & Sakmann, B. (2003) Dynamic receptive fields of reconstructed pyramidal cells in layers 3 and 2 of rat somatosensory barrel cortex. *The Journal of physiology* **553,** 243-265.
28. Kleinfeld, D. & Delaney, K. R. (1996) Distributed representation of vibrissa movement in the upper layers of somatosensory cortex revealed with voltage-sensitive dyes. *The Journal of comparative neurology* **375,** 89-108.
29. Petersen, C. C., Grinvald, A., & Sakmann, B. (2003) Spatiotemporal dynamics of sensory responses in layer 2/3 of rat barrel cortex measured in vivo by voltage-sensitive dye imaging

combined with whole-cell voltage recordings and neuron reconstructions. *J Neurosci* **23,** 1298-1309.

30. Grinvald, A., Lieke, E., Frostig, R. D., Gilbert, C. D., & Wiesel, T. N. (1986) Functional architecture of cortex revealed by optical imaging of intrinsic signals. *Nature* **324,** 361-364.
31. Jia, H., Rochefort, N. L., Chen, X., & Konnerth, A. (2011) In vivo two-photon imaging of sensory-evoked dendritic calcium signals in cortical neurons. *Nature protocols* **6,** 28-35.
32. Svoboda, K., Helmchen, F., Denk, W., & Tank, D. W. (1999) Spread of dendritic excitation in layer 2/3 pyramidal neurons in rat barrel cortex in vivo. *Nature neuroscience* **2,** 65-73.
33. Theodoridis, S. & Koutroumbas, K. (2006) *Pattern Recognition* (Elsevier).
34. Chen, X., Leischner, U., Rochefort, N. L., Nelken, I., & Konnerth, A. (2011) Functional mapping of single spines in cortical neurons in vivo. *Nature* **doi: 10.1038**.
35. Adesnik, H. & Scanziani, M. (2010) Lateral competition for cortical space by layer-specific horizontal circuits. *Nature* **464,** 1155-1160.
36. Derdikman, D., Hildesheim, R., Ahissar, E., Arieli, A., & Grinvald, A. (2003) Imaging spatiotemporal dynamics of surround inhibition in the barrels somatosensory cortex. *J Neurosci* **23,** 3100-3105.
37. Fino, E. & Yuste, R. (2011) Dense inhibitory connectivity in neocortex. *Neuron* **69,** 1188-1203.
38. Schiller, J., Major, G., Koester, H. J., & Schiller, Y. (2000) NMDA spikes in basal dendrites of cortical pyramidal neurons. *Nature* **404,** 285-289.
39. Branco, T. & Hausser, M. (2010) The single dendritic branch as a fundamental functional unit in the nervous system. *Current opinion in neurobiology* **20,** 494-502.
40. Larkum, M. E., Nevian, T., Sandler, M., Polsky, A., & Schiller, J. (2009) Synaptic integration in tuft dendrites of layer 5 pyramidal neurons: a new unifying principle. *Science (New York, N.Y* **325,** 756-760.
41. Lubke, J., Roth, A., Feldmeyer, D., & Sakmann, B. (2003) Morphometric analysis of the columnar innervation domain of neurons connecting layer 4 and layer 2/3 of juvenile rat barrel cortex. *Cereb Cortex* **13,** 1051-1063.
42. Kerr, J. N., de Kock, C. P., Greenberg, D. S., Bruno, R. M., Sakmann, B., & Helmchen, F. (2007) Spatial organization of neuronal population responses in layer 2/3 of rat barrel cortex. *J Neurosci* **27,** 13316-13328.

Fig. 1. In vivo two-photon imaging of whisker stimulation-evoked subthreshold dendritic calcium signals.

(A) Overview of the experiment design. **(B)** Intrinsic signal optical imaging to locate whisker-related columns. The map is a montage of two intrinsic optical images. **(C)** Side view of a L2/3 neuron. Black lines indicate dendrites recorded with calcium imaging, dashed lines indicate depth of focal planes. **(D)** Top view of the same neuron in panel C. **(E)** Example neurons with different distances from the SW-column center. Red/blue circles represent PW-/SW-columns, respectively; green dot indicates neuron, white line (d) indicates the distance between neuron and SW-column. **(F)** Whisker stimulation-evoked average (n=100) subthreshold depolarization normalized to the average value of PW response (absolute mean amplitude for 'proximal' 3.9 mV and for 'distant' 4.2 mV). Red/blue traces represent PW-/SW-evoked responses, respectively; gray shades indicate stimulation time window. Traces are from the same neurons as in panel E. Same notations apply for panels G-H. **(G)** Examples of PW- and SW- evoked dendritic calcium signals. Arrows indicate calcium signaling sites, dashed lines indicate dendritic portions out of the focal plane. **(H)** Normalized global dendritic calcium signals of neurons shown in panel E. Note that corresponding recordings in (F) and (H) were obtained simultaneously; both recorded neurons were hyperpolarized by 2 mV to prevent action potential firing. **(I)** Normalized SW-evoked depolarization amplitude plotted against distance. Each point represents one neuron. Dashed line represents linear fitting. **(J)** Normalized SW-evoked global dendritic calcium signal amplitude plotted against distance. Notations are same as in panel I.

Fig. 2. Spatial and temporal organization of dendritic calcium hotspots.

(A) Two-photon image of a layer 2 neuron (Alexa-channel, average of 280 frames). Yellow dashed lines represent dendrites out of focus, green dashed box indicates dendrite shown in panel B. **(B)** Upper panel: pseudo-color image of the relative fluorescent change in the OGB1-channel of the dendrite marked in panel A (projection of 1 s). Middle panel: average grayscale image of 280 frames in OGB1-channel. Yellow dashed boxes are regions of interest (ROIs) on the dendrite. Lower panel: calcium transients calculated from the ROIs indicated in the middle panel. Red asterisks indicate ROIs activated by stimulation, gray shades represent stimulation time window. **(C)** Examples of dendritic hotspot activation patterns for 3-3 trials evoked by PW and SW stimulation. Red/blue dots highlighted by arrows represent hotspot sites activated by PW/SW, respectively. **(D)** Graph of the active hotspot sites in the same focal plane as panel C. Red/blue dots indicate hotspots sites activated by PW/SW, respectively. **(E)** Example of whisker evoked calcium signals in consecutive trials. Red/blue traces represent calcium transients evoked by PW/SW, respectively; gray shades represent stimulation time window **(F)** Histograms of the response probability for all hotspots sites in all neurons.

Fig. 3. Distinct dendritic representation of multiple whiskers through specific and shared hotspot sites.

(A), (B) Weighted mapping of PW- (panel A) and SW- (panel B) evoked hotspot sites in the same focal plane. Color coded peaks and valleys represent the response probability of hotspot sites for PW and SW stimulation, respectively. **(C)** Merged mapping of PW-specific (red), SW-specific (blue), and shared (green) hotspot sites. **(D),(E)** The number of SW-specific (panel D) and shared (panel E) hotspot sites depends on the distance between the neuron and the SW-column. Each point represents one neuron. Blue/green dashed lines are linear fitting of the number of SW- specific/shared hotspot sites versus distance, respectively. Red dashed line represents the average number of PW-specific hotspot sites (the correlation between number of PW-specific hotspot sites and distance was not significant). **(F),(G)** Inter-trial pattern correlation for all focal planes in one neuron (panel F) and in all 12 neurons (panel G). Each point represents one trial, where the x-coordinate is the average of pattern correlation value to all the other PW trials of the same focal plane, and the y-coordinate is that to all the other SW trials. Dashed line represents the criterion of judgment for the classifier.

Fig. 4. Multiple peripheral sensory input channels converge on single shared spines

(**A**), Two-photon image of a layer 2 neuron, recorded in full frame at 40 Hz, averaging 280 frames. Yellow dashed lines represent dendrites out of focus, green dashed box indicates the portion of dendrite shown in panel B. (**B**), Two-photon image of a dendrite portion (average 1400 frames) recorded in partial frame at 200 Hz (see methods). Green boxes with dots and orange dots indicate dendritic segments and spines from which calcium signals were calculated, respectively. (**C**), Top view of the volume rendering of the same dendrite. (**D**), Calcium signals from single spines and dendritic segments as marked in panel B. Red/blue traces represent identified calcium transients in spines evoked by PW/SW, respectively; gray shades represent stimulation time window. (**E**), Spine activation patterns in consecutive trials. Red/blue dots indicate spines activated by PW/SW, respectively; green arrows indicate spines activated by both whiskers. (**F**), Categorization of spines in panel E. Red: PW-specific, blue: SW-specific, green: shared. (**G**), Number of responsive spines per dendrite length. (**H-K**), Histograms of the response probability of spines in different categories. (**L**), Scheme of the candidate presynaptic sources of PW-specific, SW-specific and shared inputs.

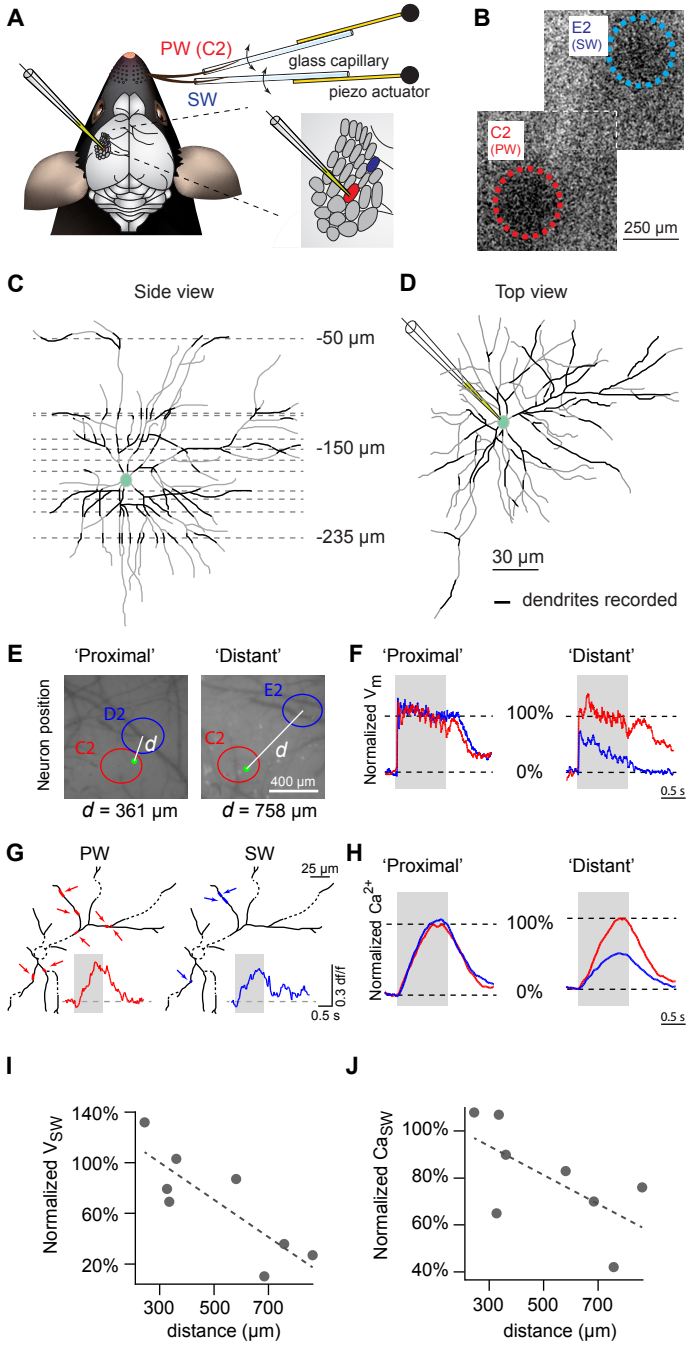

Fig. 1. In vivo two-photon imaging of whisker stimulation-evoked subthreshold dendritic calcium signals

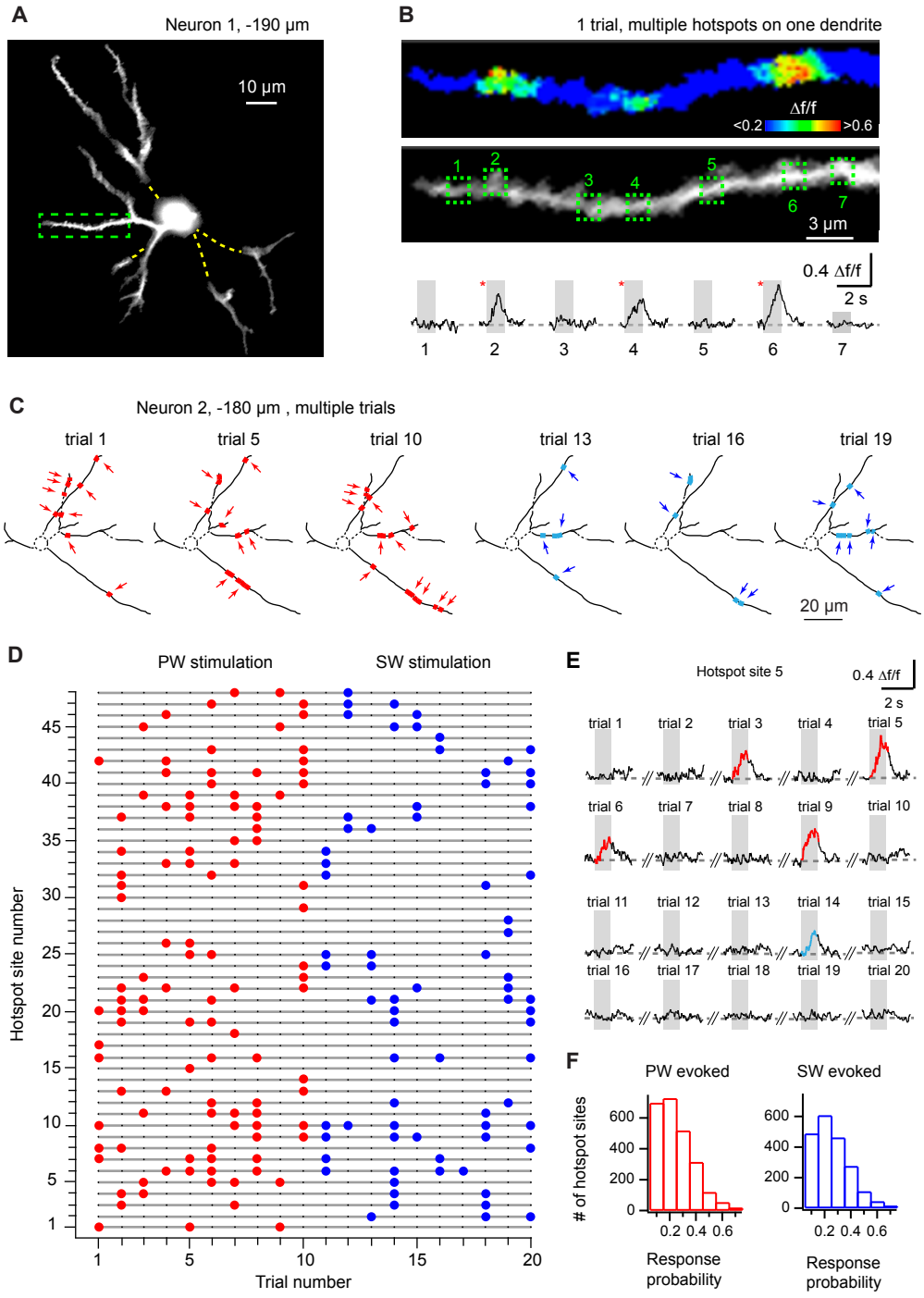

Fig. 2. Spatial and temporal organization of dendritic calcium hotspots

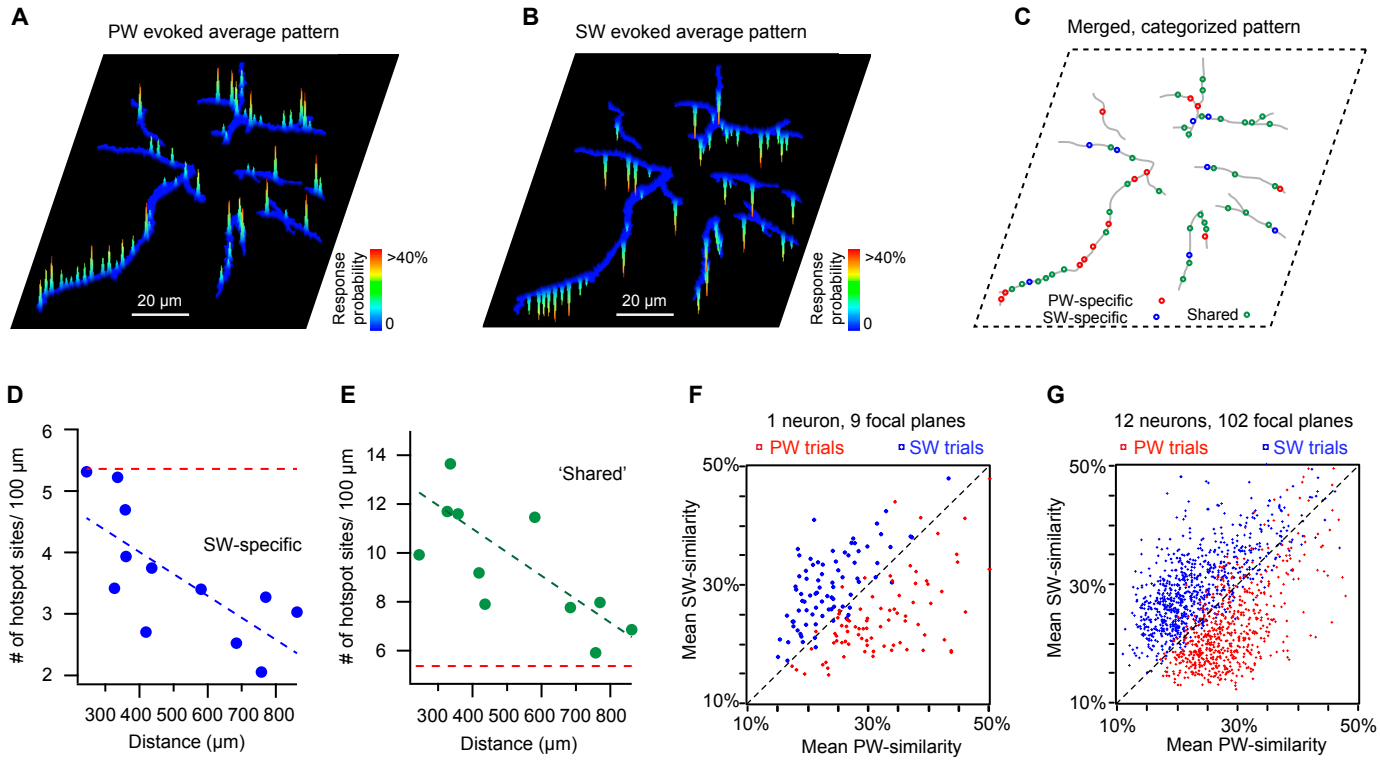

Fig. 3. Distinct dendritic representation of multiple whiskers through specific and shared hotspot sites

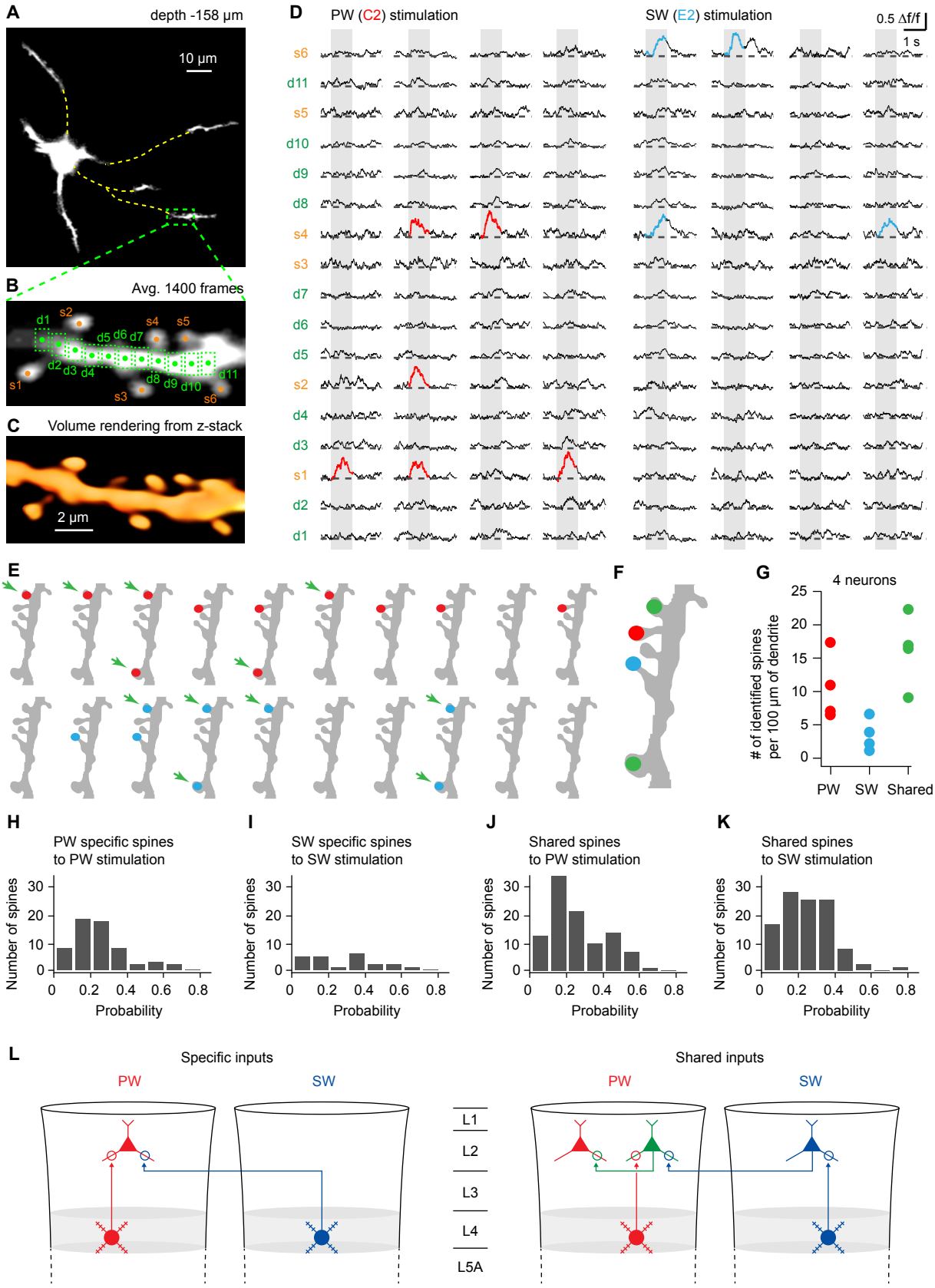

Fig. 4. Multiple peripheral sensory input channels converge on single ‘shared’ spines

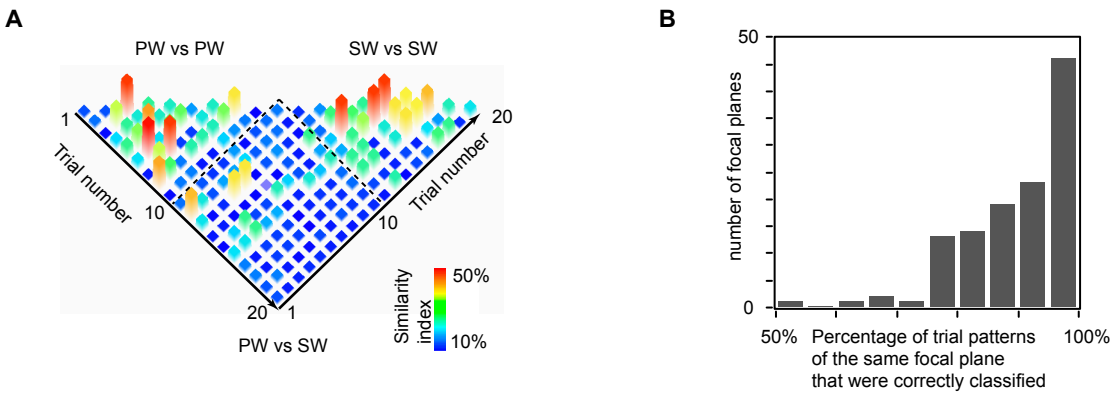

Fig. S1. Algorithm illustration and overall performance of classifier for distinguishing dendritic activation patterns

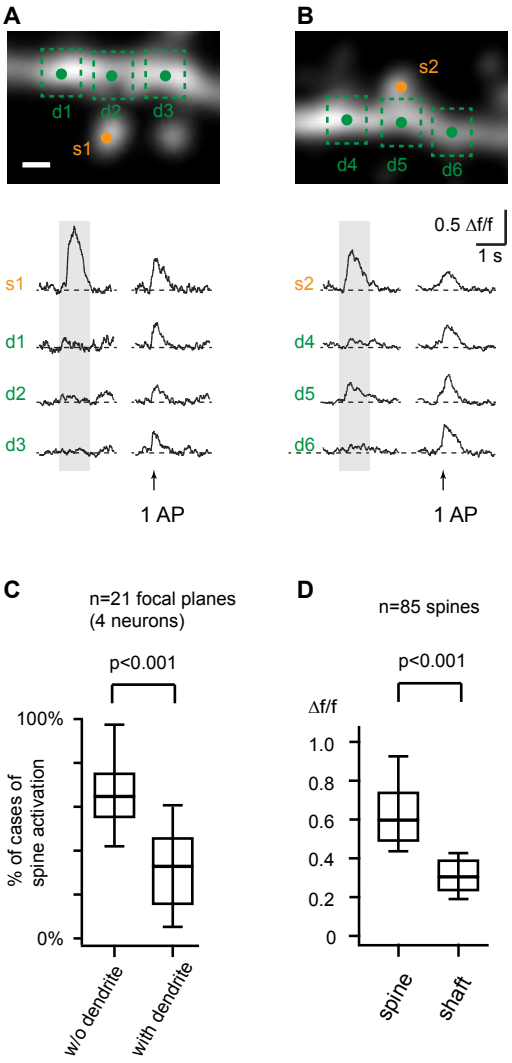

Fig. S2. Spine origin of subthreshold dendritic calcium signals.

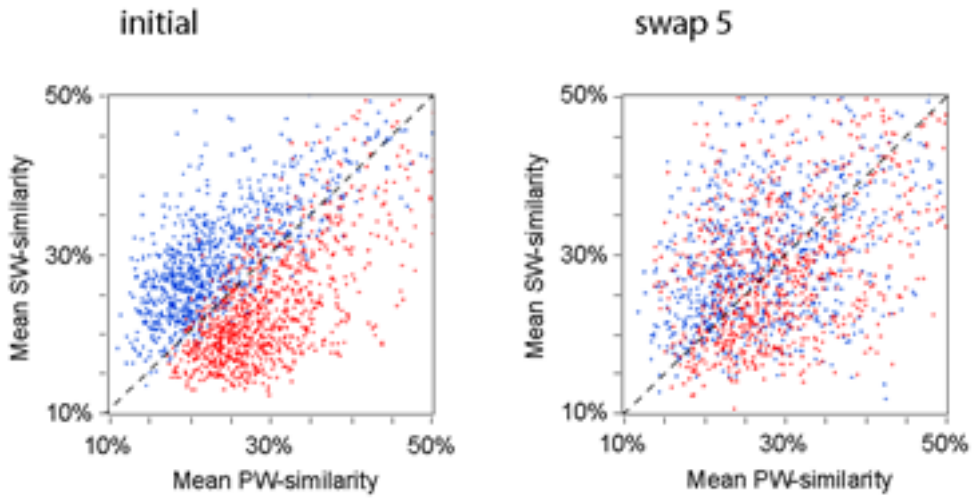

Fig. S3. Output of the classifier for randomly shuffled input dataset

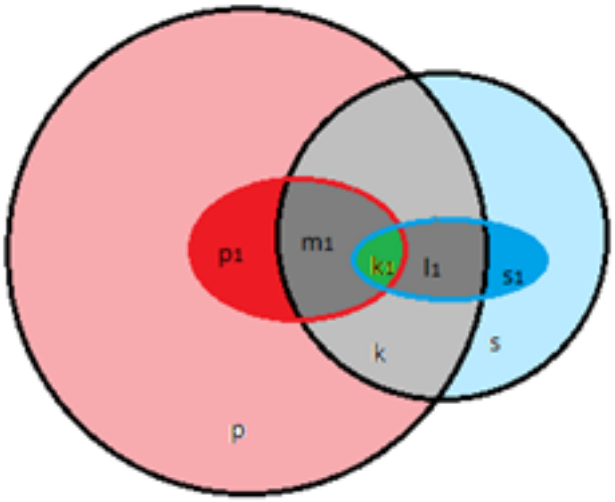

Fig. S4. Possible configurations of activated input sites for PW-SW pattern pairs

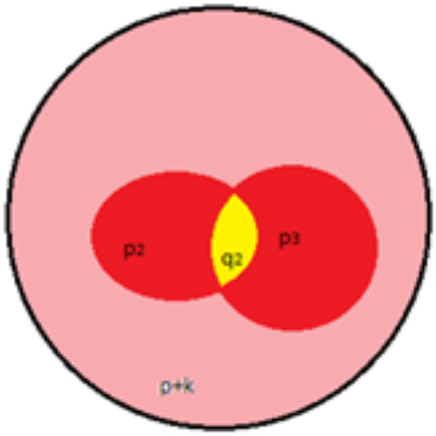

Fig. S5. Possible configurations of activated input sites for PW-PW pattern pairs

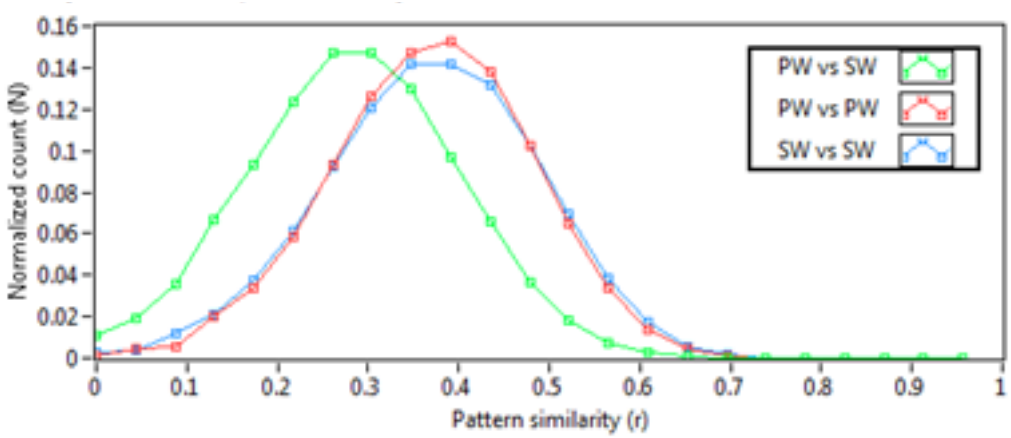

Fig. S6. Probability distribution function of pattern similarity

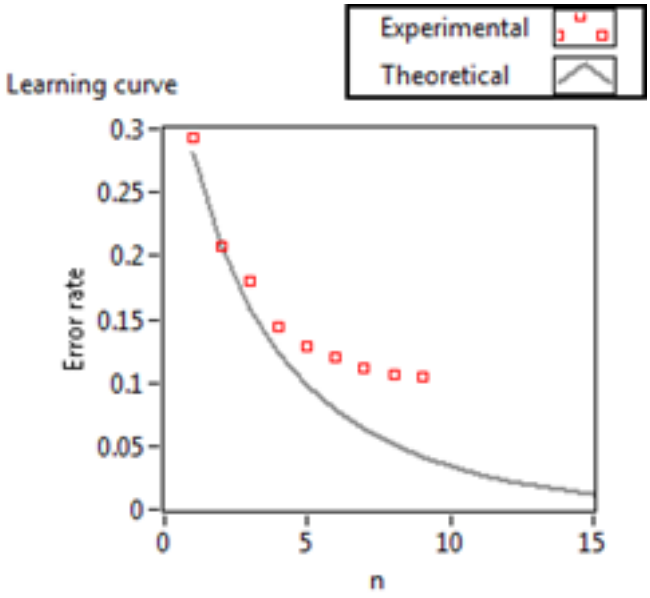

Fig. S7. Learning curve of the classifier

Fig. S1. Algorithm illustration and overall performance of classifier for distinguishing dendritic activation patterns.

(A) Simliarity indices for one focal plane of dendritic imaging. Trial numbers 1-10 are PW trials and 11-20 are SW trials. Each color bar represents the similarity index between the two trials as given its coordinates in the plot. (B) Performance of the classifier. One focal plane had 20 trials (10 PW and 10 SW), if all 20 trials were correctly classified, it adds one count to the bar at 100% in the histogram. If 1 trial was incorrectly classified while other 19 were correct, it adds one count to the bar at 95%, and so on.

Fig. S2. Spine origin of subthreshold dendritic calcium signals.

(A), (B), Upper panel: two-photon image (maximum projection of z-stack) of a dendrite and spines of a layer 2 neuron. Green boxes with dots indicate ROIs on dendritic shaft segments, orange dots indicate single spines, gray shades represent whisker stimulation. Lower panel: calcium signals from ROIs marked in upper panels. Scale bar: 1 μm. (C), The proportion of spine activation events without or with dendritic shaft activation. Middle bar: median value, boxes: 25-75 percentile, error bars: 10-90 # percentile. Statistical test: Wilcoxon ranked test. (D), The amplitude of calcium transient of spine and dendritic shaft in cases of shaft activation. Same notations as panel C.

Fig. S3. Output of the classifier for randomly shuffled input dataset.

Left panel: classifying results on initial dataset before shuffling, right panel: classifying results on shuffled dataset, for each 10 trials of PW, 5 were randomly chosen to swap with 5 trials randomly chosen from the corresponding SW trials in the same focal plane. Notations same as main Fig. 3 F,G.

Fig. S4. Possible configurations of activated input sites for PW-SW pattern pairs.

p_1 : the number of PW-specific input sites that were activated in the PW pattern, s_1 : the number of SW-specific input sites that were activated in the SW pattern, m_1 : the number of shared input sites that were activated only in the PW pattern, l_1 : the number of shared input sites that were activated only in the SW pattern, k_1 : the number of shared input sites that were activated in both patterns.

Fig. S5. Possible configurations of activated input sites for PW-PW pattern pairs.

q_2 : the number of same input sites activated in both patterns. p_2 and p_3 : the number of input sites being activated in only one of the two patterns, respectively.

Fig. S6. Probability distribution functions of pattern similarity.

Green curve: distribution function of pattern similarity indices for PW-SW pairs. Red curve: distribution function of pattern similarity indices for PW-PW pairs. Blue curve: distribution function of pattern similarity indices for SW-SW pairs.

Fig. S7. Learning curve of the classifier.

Gray curve represent the theoretically calculated learning curve, red dots represent the actual learning curve derived from experimental dataset.

Supporting texts and figure legends of supporting figures

Text S1 Materials and Methods

All experimental procedures were performed in accordance with institutional animal welfare guidelines and were approved by the state government of Bavaria, Germany.

1. Animal preparation

Animal preparation procedures were the same as those previously described (31), except for the treatment of whiskers. With the exception of 2 whiskers (C2 and either E2, D2, C4 or C1) on the right side, all other whiskers were plucked. The spared whiskers were shortened to 1 cm and were inserted into two glass capillaries which could be separately deflected by piezoelectric actuators. The position of the barrel columns related to the spared whiskers was determined using intrinsic signal optical imaging (see below). C57BL/6 mice (P28-38, n=16) were used for in vivo dendrite and spine imaging experiments.

2. Whisker stimulation

The same whisker stimulation protocol was use during intrinsic signal optical and two-photon calcium imaging experiments. Whiskers were inserted into glass capillaries attached to piezoelectric actuators and deflected by approximately 30˚ in rostrocaudal direction. A pulse stimulator (Model 2100, A-M systems) delivered for each trial a train of voltage pulses (10 pulses, 50 ms, 10 Hz) driving the piezoelectric actuators. In each trial only one whisker was stimulated.

3. Intrinsic signal optical imaging

The location of the barrel columns related to the spared whiskers was mapped on the cortex by intrinsic signal optical imaging through the intact skull. The intrinsic signal optical imaging setup was combined with the two-photon microscope. During intrinsic signal imaging, one of the oculars was replaced by a camera (National Instruments smart camera NI-1744, pixel resolution cropped to 1024x1024), and the microscope objective was replaced by a camera lens (Olympus, 50mm/f3.5) inversely oriented (back focal plane on the cortex). The field of view was 1.1 x 1.1 mm. Illumination was provided by a green (515-530 nm) or a red (620-625 nm) LED-array attached to the camera lens. Green light was used to acquire the blood vessel map of the cortical surface; red light was used to record the functional map of the barrels. Images were acquired at 10 Hz by a custom-made acquisition program. Each image was spatially filtered by a Gaussian kernel of 5x5 pixels. Image acquisition protocol consisted of two 1s acquisition periods that were repeated 10 times. The first acquisition period was just after the offset of whisker stimulation, the second one (baseline) was at 16 s after the stimulation. Relative reflectance changes were calculated as the summed images acquired during stimulation divided by the summed baseline images. The two whiskers were mapped in consecutive sessions.

4. Whole-cell recording

Having the two whisker-related barrels mapped by intrinsic signal optical imaging, whole-cell configuration was established on a layer 2 neuron in one of the barrel columns (principal barrel, C2). Patch pipettes with resistances of 5-8 MΩ were pulled from borosilicate glass capillaries on a vertical puller (PC-10, Narishige). The pipette solution contained 112 mM K-gluconate, 10 mM HEPES, 8 mM KCl, 10 mM Na-phosphocreatine, 4 mM Mg-ATP, 0.3 mM Na_2-GTP , 100 μM Oregon Green 488 BAPTA-1 hexapotassium salt (denoted as "OGB1"), 25 μM Alexa Fluor 594 hydrazide sodium salt (denoted as "Alexa"). Current-clamp recordings were acquired with an EPC-9 HEKA amplifier through software Pulse. Signals were filtered at 3 kHz and digitized at 10 kHz. Series resistances ranged from 20-60 MΩ. During the combined subthreshold recording and two-photon calcium imaging, neurons were slightly hyperpolarized to prevent AP firing. For this purpose, negative current was injected through the patch pipette in steps of -10 pA, until AP firing vanished. Over the course of the recording, the injected current level was adapted to the condition of the neurons and, if necessary, more negative current was injected. However, neurons were not hyperpolarized below -85 mV. For further verification, the exact location of each neuron was post-hoc documented by epifluorescence imaging and marked on the map of barrels aligned by the blood vessel map (Fig. 1E).

5. Two-photon calcium imaging of dendritic hotspots

Two-photon calcium imaging was performed on a custom built setup which was similar to that used in previous study (11). A resonant scanner unit (GSI Lumonics) including one fast axis of 12 kHz resonant mirror and one slow axis of standard galvanometric mirror was mounted on upright microscope chassis (BX51, Olympus) with long working distance water-immersion objective (Nikon 40x/0.8). Fluorescent excitation light was delivered by pulsing infrared laser (wavelength 800 nm, pulse width 100 fs, repetition rate 80 MHz) equipped with pre-chirper (model 'DeepSee", Spectra-Physics). Laser power under the objective was typically 30-40 mW. Emitted fluorescent photons were separated by a beamsplitter mirror at 570 nm (F33-572, AHF Analysentechnik) and detected by high-sensitivity photomultiplier tubes (H-7224, Hamamatsu) and analog current amplifiers (DHPCA-100, FEMTO Messtechnik). The laser scanning, image acquisition and stimulation triggering were controlled by a real-time PXI computer (PXIe-1082, National Instruments) equipped with FPGA I/O board (PXI-7831R) and high-speed digitizer (PXI-5122). The user interface software was developed in LabVIEW (v2009) on an 8-core PC connected to the PXI computer. Full frame images consisted of 512 lines, and were scanned with 40 Hz repetition rate. Each line had 1041 raw pixels that were digitized at 25 MHz (100 MHz internal sampling rate) and reconfigured into 512 pixels according to the sinusoidal trajectory of the resonant mirror.

Neurons were imaged in 6-11 focal planes distributed across the whole depth of the dendritic tree. The actual width of the field-of-view (controlled by the amplitude of scanning mirror rotation) ranged between 100-200 μm, depending on the layout of dendrites in the focal plane. Each focal plane was

probed with 10 trials of PW and 10 trials of SW stimulation. Trials were interlaced (5 PW trials followed by 5 SW trials, repeated twice) with variable time intervals (10-20s) between two consecutive trials. For display purposes (Fig. 2C-E; and for spines, Fig.4D-E), the trials with the same whisker stimulation were grouped together. Z-stack images were taken at the largest possible field-of-view (300 µm x 300 µm) with a step size 0.5 µm.

6. Two-photon calcium imaging of spines

The same two-photon imaging setup was used for the imaging of single spines. For the implementation of the low power temporal oversampling (LOTOS) procedure (34), the scanner was configured for the following mode: the number of lines was reduced to 64, the number of pixels in each line resampled to 256, and the image repetition speed increased to 200 Hz. The width of field-of-view was accordingly reduced to the range of 27-42 µm. All together, the spatial oversampling was 2x2 fold and temporal oversampling was 5 fold, compared to the mode for dendritic imaging as described above. Laser power was reduced to 15-25 mW during spine imaging. Recording protocol for the spine imaging was the same as for the dendritic imaging, except that only C2-E2 whisker configuration was used. Z-stack images of the spines were taken with step size 0.2 µm.

7. Data analysis

The structural reconstruction was performed using the WCIF-ImageJ software (open-access from http://www.uhnresearch.ca/facilities/wcif/imagej/), the whole-cell recordings were analyzed in Igor (Igor Pro v5.0.1.0, Wavemetrics Inc.) and the calcium imaging recordings were analyzed by custom-written programs in LabVIEW (version 2009, National Instruments). Statistical tests were performed in SPSS (version 17.0, IBM). Z-stack images of spines were deconvolved in Huygens (version J27.14, Scientific Volume Imaging BV) and volume rendered in Amira (version 5.3.3, Visage Imaging Inc.).

7.1. Reconstruction of dendritic trees. The projections for top-views and side-views were generated from the z-stack images from the Alexa-channel of the two-photon microscope. The lengths of dendrites for each recorded focal plane were measured by the internal scale function in ImageJ.

7.2. Calculation of whisker-evoked subthreshold membrane potential depolarization. For each neuron and each whisker, 100 trials of subthreshold membrane potential recordings were averaged and aligned to the baseline of 0.2 s before stimulation onset. The stimulation evoked depolarization was defined as the mean value of membrane potential of the 1s of stimulation time window subtracting the mean value of the baseline. To compare the result among neurons, the SW-evoked depolarization was normalized to the maximum value of PW-evoked depolarization.

7.3. Spatial-temporal filtering of calcium imaging data and transformation into Δf/f image sequences. First, each image from the OGB1-channel was convolved with a Gaussian spatial filter kernel (size: 1 µm). The temporal sequence of images was processed with exponentially-weighted averaging, and transformed into a new temporal sequence of Δf/f images representing the time-dependent relative

change of each pixel. This calculation was similar as described previously (31) except that it was performed for every pixel instead of manually chosen regions-of-interest. Static color-coded images in Fig. 2 were taken as the maximum projections of Δf/f image sequence for the stimulation time window and rendered by a color lookup table. For display purpose in figures, we used square ROIs to indicate the location of active hotspot sites.

7.4. Calculation of global dendritic calcium signals. For each trial, the Δf/f image temporal sequence was projected for the entire stimulation time window and thresholded at the Δf/f value of 0.3. All pixels above threshold appeared as isolated patches of dendrites, and were taken together as one region-of-interest (ROI). The Δf/f trace of this ROI was calculated by the same algorithm as in point 7.3. To normalize the Δf/f trace of all trials for the same whisker for one neuron, each trace was multiplied by the number of above-threshold pixels in the corresponding hotspot and then summed. The peak value of the summed trace for PW trials was taken as 100% for normalization.

7.5. Detection and categorization of dendritic hotspot sites. For each stimulation (1s duration), every 4 frames (100 ms duration) of the Δf/f image temporal sequence were maximum-projected as one image. These projected Δf/f images were thresholded at the value of 0.3. Patches with above-threshold pixels were registered to separate ROIs according to the position of the pixels. The time course of Δf/f for these ROIs was re-calculated for 8 seconds (including 3 s before stimulation onset and 4 s after stimulation offset). If the peak amplitude of Δf/f trace in the stimulation time window was greater than 4 times standard deviation of the trace in the non-stimulation time window, the signal was considered as a response event. Hotspot sites were defined by overlaying response events over all trials. The response probability for hotspot sites was defined as the number of response events occurred at one site divided by the total number of trials. A hotspot site is defined as PW-specific if the PW-response probability is 3 times higher than SW-response probability, and vice versa as for SW-specific hotspot site. If the response probabilities to both whiskers are non-zero and to neither whisker is 3 times higher than to the other whisker, the hotspot site is defined as shared.

7.6. Simple classifier for distinguishing PW and SW patterns

7.6.1. Calculation of similarity index. For each trial, an image was created by assigning value 1 to the pixels of all detected hotspot events (without categorizing the hotspots) and value 0 to all the other pixels. Between any two trials of the same focal plane, the “similarity index” was defined as the maximum value of the normalized cross-correlation between the two pattern images, as described in the following formulae (adapted from the open-access online document “NI-vision concepts manual” , page 12-7 to 12-8.
http://digital.ni.com/manuals.nsf/websearch/E1F8EB3E2E28AE34862570AC005CC736. See also ref (43)).

Consider two images (matrices) $w_1(x,y)$ and $w_2(x,y)$, both of $M \times N$ size, each of them have a few pixels with value 1 and most pixels with value 0. Let the second image shift pixel by pixel and calculate

the normalized cross product with the first image for each shifting step. These calculations result also in an image (matrix) of the same size, namely, the normalized cross-correlation image $R(i,j)$,

$$R(i,j) = \sum_{x=0}^{M-1}\sum_{y=0}^{N-1} w_1(x,y)\cdot w_2(x+i,y+j) \Big/ \sqrt{W_1 \cdot W_2}$$

where

$$W_1 = \sum_{x=0}^{M-1}\sum_{y=0}^{N-1} w_1(x,y) \text{ and } W_2 = \sum_{x=0}^{M-1}\sum_{y=0}^{N-1} w_2(x,y)$$

are the sum of all pixel values in each image.

The maximum value in $R(i,j)$ describes how well the two images are correlated, thus being defined as the "similarity index" $R_{1,2}$ for image 1 and 2 (trial 1 and 2):

$$R_{1,2} = \max_{i,j}\{R(i,j)\}$$

7.6.2. Mean whisker similarity. For a given trial, the "Mean PW-similarity" and "Mean SW-similarity" was defined as the average of similarity indices between the trial and all other PW trials and SW trials, respectively. Denote $P_1, P_2 \ldots, P_{10}$ to be PW trials, and $S_1, S_2 \ldots, S_{10}$ to be SW trials. For any trial T, the "Mean PW-similarity" $\overline{R_P}$ was defined as

$$\overline{R_P} = \sum_{P_i \neq T} R_{T,P_i} \Big/ \sum_{P_i \neq T} 1$$

Correspondingly, the "Mean SW-similarity" $\overline{R_S}$ was defined as

$$\overline{R_S} = \sum_{S_i \neq T} R_{T,S_i} \Big/ \sum_{S_i \neq T} 1$$

For each point in Figure 3 F,G, the x-coordinate is $\overline{R_P}$ and the y-coordinate is $\overline{R_S}$.

7.6.3. Readout of the classifier. For each trial, if $\overline{R_P} \geq \overline{R_S}$, this trial was determined to correspond to PW, otherwise to SW.

7.6.4. Verification of the classifier. For each dataset, 5 PW trials were randomly chosen and swapped with 5 randomly chosen SW trials. The classifier re-calculated from step 7.6.1 to step 7.6.3, without the information about which trials were swapped. The result that we obtained is illustrated in Figure S3. In contrast to the clear separation PW and SW trial derived values shown in main Figure 3, we find that the swapping of half of the PW and SW patterns produced an intermingling of the classifier's output data and a loss of any obvious order.

7.7. Calculation of calcium signals of individual spines (applies to 200 Hz spine imaging only). For each focal plane, the dendritic shaft was segmented with consecutive square box-like ROIs (about 1 µm) and, in addition, ROIs were drawn for each discernable spine. The calcium signals of the ROIs were calculated as indicated above. The categorization in whisker-specific and shared spines was the same as that for the dendritic hotspot sites.

Text S2

Theoretical verification for the uniqueness of the sets of dendritic input activation patterns

Figure 3F, G indicates that PW and SW stimulation produce distinct sets of activation patterns, respectively. These results were obtained, because of unavoidable experimental limitations, from a limited number of trials and focal planes. In order to test that our classifier is generally valid, we devised a numerical model.

Let us start from a very simple model based on set theory. Define $H = \{1,2,3, \dots h\}$ be the set of all functional input sites, $P \subseteq H$ is a subset of H which is the set of all active input sites for the principle whisker, $S \subseteq H$ is a subset of H which is the set of all active input sites for the surround whisker. No other input sites are considered, therefore the union of P and S makes up exactly H. i.e. $H = P \cup S$.

Denote "cardinality" $|H|$ of set H to be the total number of elements in H. According to the inclusion-exclusion principle we have $|P \cup S| = |P| + |S| - |P \cap S|$

Denote "powerset" 2^H of set H to be the set of all subsets of H, including the empty set $\emptyset$ and H itself. For example, $H = \{1,2,3\}$, then $2^H = \{\emptyset, \{1\}, \{2\}, \{3\}, \{1,2\}, \{1,3\}, \{2,3\}, \{1,2,3\}\}$. We can calculate that the cardinality of 2^H is 2 raised to the power |H|, where |H| is the cardinality of H. i.e., $|2^H| = 2^{|H|}$. (44)

We denote by 2^P the set of all possible activation patterns for PW, by 2^S the set of all possible activation patterns for SW, and by $2^P \cap 2^S$ the set of all activation patterns that can be activated by either whisker. Note that $2^P \cap 2^S = 2^{P \cap S}$. (44).

The question is, what is the probability p_{ps} for PW stimulation to activate a pattern that can be also activated by SW, and vice versa, what is the probability p_{sp} for SW stimulation to activate a pattern that can be also activated by PW?

Let us assume that all possible activation patterns could occur with equal probability (The validity of this assumption will be discussed later on). Specifically, any PW trial randomly picks one element (activation pattern) from 2^P, and any SW trial picks one element from 2^S. Then, p_{ps} is the conditional probability of the activation pattern to be in $2^P \cap 2^S$ given that it is in 2^P. Therefore p_{ps} can be calculated as:

$$p_{ps} = \frac{|2^P \cap 2^S|}{|2^P|} = \frac{|2^{P \cap S}|}{|2^P|} = \frac{2^{|P \cap S|}}{2^{|P|}} \quad (1a)$$

In the same way we can calculate p_{sp}:

$$p_{sp} = \frac{|2^P \cap 2^S|}{|2^S|} = \frac{|2^{P\cap S}|}{|2^S|} = \frac{2^{|P\cap S|}}{2^{|S|}} \quad (1b)$$

For an intuitive understanding we can use some numbers that are in the range of an actual measurement, for example, $|H| = 55$, $|P| = 45$, $|S| = 40$, $|P \cap S| = 30$, then we get

$$p_{ps} = \frac{2^{30}}{2^{45}} = 2^{-15} \approx 3 \times 10^{-5}, p_{sp} = \frac{2^{30}}{2^{40}} = 2^{-10} \approx 10^{-3}$$

These are very small probabilities, taking into consideration the fact that the number of shared input sites $|P \cap S|$ is more than half of the number of all functional input sites $|H|$. In this example we used numbers that were derived from recordings in one focal plane. If we extrapolate the numbers to 10 focal planes (see Fig 1C, D), assuming $|H| = 550$ and keeping the relative ratio of input site numbers, then we get

$$p_{ps} = 2^{-150} \approx 7 \times 10^{-46}\ ,\ p_{sp} = 2^{-100} \approx 8 \times 10^{-31}$$

Therefore, despite the relatively high proportion of **shared input sites** among all input sites, the proportion of **shared activation patterns** among all possible activation patterns is very low.

The simple model above demonstrated that the PW-activation pattern set and the SW-activation pattern set are highly distinct. However, we should reconsider the assumption that all patterns could occur at equal probability. This assumption is correct when every input site is randomly activated at probability of $Pr_0 = 0.5$ on each appropriate activation (by PW or SW). However, experimental data suggest $Pr_0 \approx 0.2$ (Fig 2F). Therefore the theoretical predictions are conservative since p_{ps} and p_{sp} can be even smaller when $Pr_0 < 0.5$.

We should also carefully consider the practical interpretation of those small probabilities p_{ps} and p_{sp}. In this idealized model, two activation patterns are considered to be same only if both contain exactly the same input sites. Therefore, the small values of p_{ps} and p_{sp} actually indicate that in most probable cases, two activation patterns contain a small proportion of input sites in common. We adapt the definition of "pattern similarity" from the analysis of 2D dendritic imaging data (see Materials and Methods 7.6.1). Here, we define "pattern similarity" r for a pair of patterns to be the number of activated input sites common in both patterns divided by the geometric mean of the number of activated input sites in each pattern. Denote A_1 by the number of activated input sites in pattern 1, A_2 by the number of activated input sites in pattern 2, and A_{12} by the number of activated input sites common in pattern 1 and 2. Therefore, r is defined as

$$r = \frac{A_{12}}{\sqrt{\mathrm{A}_1 \times A_2}}$$

When two patterns are identical, $r = 1$; when two patterns contain no common input site, $r = 0$; in other cases $0 < r < 1$. We expect $r < 1$ for pairs of patterns from PW and SW stimulations. But because the patterns are rather sparse (Pr_0 is low), we expect also $r < 1$ for pairs of patterns from two different stimulations of PW. We will therefore calculate the probability distribution function of r for PW-SW pairs, but also for PW-PW pairs and SW-SW pairs. We will show that the expected value of r for PW-SW pairs is measurably smaller than for PW-PW and SW-SW pairs.

We start by calculating r for pairs of PW-SW patterns. Denote $p = |P| - |P \cap S|$ to be the number of PW-specific input sites, $s = |S| - |P \cap S|$ to be the number of SW-specific input sites, $k = |P \cap S|$ to be the number of shared input sites. See the Venn's Diagram in Figure S4. Consider a PW pattern and a SW pattern, denote:

p_1 : the number of PW-specific input sites that were activated in the PW pattern,

s_1 : the number of SW-specific input sites that were activated in the SW pattern,

m_1 : the number of shared input sites that were activated only in the PW pattern,

l_1 : the number of shared input sites that were activated only in the SW pattern,

k_1 : the number of shared input sites that were activated in both patterns.

We have the following numerical conditions on these numbers:

$0 \le p_1 \le p$

$0 \le s_1 \le s$

$0 \le (m_1 + l_1 + k_1) \le k$

Since $Pr_0 \neq 0.5$, the probabilities for observing each of these numbers follow the binomial distribution. Define $f(p_1, p, Pr_0)$ to be the probability to have exactly p_1 out of p inputs being activated when the probability of each input to be activated is Pr_0.

$$f(p_1, p, Pr_0) = \frac{p!}{p_1!\,(p - p_1)!} \cdot (Pr_0)^{p_1}(1 - Pr_0)^{p - p_1}$$

We can then express the probability $N(p_1, s_1, m_1, l_1, k_1)$ for observing the configuration of five variable numbers $(p_1, s_1, m_1, l_1, k_1)$:

$$N(p_1, s_1, m_1, l_1, k_1) = f(p_1, p, Pr_0) \cdot f(s_1, s, Pr_0) \cdot f(m_1, k, Pr_0) \cdot f(n_1, k - m_1, Pr_0) \cdot f(k_1, k - m_1 - l_1, Pr_0) \quad (2)$$

For such configurations the "pattern similarity" r as a function of $(p_1, s_1, m_1, l_1, k_1)$ is

$$r(p_1, s_1, m_1, n_1, k_1) = \frac{k_1}{\sqrt{(p_1 + m_1 + k_1) \times (s_1 + l_1 + k_1)}} \quad (3)$$

Next, we want to calculate r for PW-PW patterns. The configurations become simpler (Figure S5) and we use here three variable numbers:

q_2 : the number of same input sites activated in both patterns

p_2 and p_3 : the number of input sites being activated in only one of the two patterns, respectively.

And we get

$$N(p_2, p_3, q_2) = f(p_2, p+k, Pr_0) \cdot f(p_3, p+k-p_2, Pr_0) \cdot f(q_2, p+k-p_2-p_3, Pr_0) \quad (4)$$

$$r(p_2, p_3, q_2) = \frac{q_2}{\sqrt{(p_2+q_2) \times (p_3+q_2)}} \quad (5)$$

We can also apply equation (4) and (5) for SW-SW pairs, just replacing every symbol p by s.

We numerically calculated the distribution $N(r)$ by enumerating all possible combinations of the variable numbers $(p_1, s_1, m_1, l_1, k_1)$ and (p_2, p_3, q_2). We used the same numbers of input sites as we did for equation (1), so that $p = 15, s = 10, k = 30$. We used $Pr_0 = 0.245$, which is the median (non-rounded value) of the activation probabilities of single input sites. The binned distribution $N(r)$ for the three conditions (PW-SW, PW-PW and SW-SW) is shown in Figure S6.

If we fit the probability distribution function to Gaussian in our numerical calculation as above, the mean values (expected values) are: $\bar{r}_{P-S} = 0.284$, $\bar{r}_{P-P} = \bar{r}_{S-S} = 0.374$ .They correspond well with the values derived from our data ($\bar{r}_{P-S} = 0.283$, $\bar{r}_{P-P} = \bar{r}_{S-S} = 0.336$).

The performance of our classifier relies on those probability distribution functions (Figure S6, red versus green plot, or blue versus green plot). For a new pattern to be classified, the pattern similarity between this pattern and other patterns in the two existing learning sets are calculated, resulting in S_P samples of one distribution and S_S samples of another distribution. Denote $\overline{S_P}$ by the mean value of the S_P samples, $\overline{S_S}$ by the mean value of the S_S samples, and $\Delta_{PS} = \overline{S_P} - \overline{S_S}$ by the differences between them. Error of the classifier means either of the following case: the new pattern is PW while $\Delta_{PS} < 0$; or the new pattern is SW while $\Delta_{PS} > 0$. Since these two cases are equivalent, we just consider the former one. Therefore $\overline{S_P}$ is the mean of the PW-PW pattern similarity distribution (red Gaussian function in Figure S6), and $\overline{S_S}$ is the mean of PW-SW pattern similarity distribution (green Gaussian function in Figure S6). Δ_{PS} also subjects to a Gaussian distribution, which has the mean $ì_\Delta$ as

$$ì_\Delta = \bar{r}_{P-P} - \bar{r}_{P-S} \quad (6)$$

and the standard deviation $ó_\Delta$ as

$$ó_\Delta = \sqrt{\frac{1}{n}(ó_{P-P}^2 + ó_{P-S}^2)} \quad (7)$$

where n is the number of samples (in the learning pool), $ó_{P-P}$ and $ó_{P-S}$ are the fitted standard deviation of the red and green Gaussian function in Figure S6, respectively.

The error rate of the classifier is the probability when $\Delta_{PS} < 0$, denoted by $Prob\{\Delta_{PS} < 0\}$. It can be calculated as the area below the $\Delta_{PS} < 0$ part of the Gaussian curve.
(see also http://en.wikipedia.org/wiki/Cumulative_distribution_function)

$$Prob\{\Delta_{PS} < 0\} = \frac{1}{2}\left[1 + erf\left(\frac{0 - \lambda_{\Delta}}{\sigma_{\Delta} \cdot \sqrt{2}}\right)\right] \quad (8)$$

where

$$erf(x) = \frac{2}{\sqrt{\pi}} \int_0^x e^{-t^2} dt$$

is the commonly used “error function” (http://en.wikipedia.org/wiki/Error_function)

We note that, the calculation process of the classifier involves one fix pattern (the test pattern) and other variable patterns (learning pool). Theoretically, except that the learning pool is infinitely large, the pattern similarity distribution functions for different whisker pairs are not strictly Gaussian. A detailed numerical analysis would require Monte-Carlo methods, but it is not necessary here because our experimental data rejected the hypothesis that distributions of r_{P-P}, r_{P-S} and r_{S-S} are not Gaussian.

An interesting finding of our theoretical calculations is that the error rate of classifier decreases in sigmoidal manner with the number of samples, n. From Figure S6 we get $\bar{r}_{P-P} = 0.284$ $\bar{r}_{P-S} = 0.374$, $\sigma_{P-P} = \sigma_{P-S} = 0.11$, then we calculated $\lambda_{\Delta} = 0.090$. Keep λ_{Δ}, σ_{P-P} and σ_{P-S} unchanged, we can calculate the relation between $Prob\{\Delta_{PS} < 0\}$ and n, namely, the “learning curve”. For experimental data, we can also test the error rate of the classifier by providing subsets of learning trials. For example, to test $n = 4$, we use the first 4 trials for the learning patterns and the other 6 for testing patterns. Note that maximum $n = 9$ for experimental data because at least one pattern needs to serve as test pattern. The theoretical and experimental results are shown in Figure S7. The actual error rates of the classifier derived from all recorded neurons generally follow the theoretical curve but deviates more by larger n, these differences could be as well attributed to experimental factors.

In summary, our numerical model provides strong support for the conclusions that were derived from our experimental data by showing that our classifier is generally valid. Thus, despite the fact that a large proportion of input sites are shared, the dendritic activation pattern sets of PW and SW stimulation are distinct. In practice, we conclude that 10 trials for each whisker are sufficient for our simple classifier to correctly distinguish the two activation pattern sets of PW and SW stimulation.

References

43. M. A. Treiber, An Introduction to Object Recognition: Selected Algorithms for a Wide Variety of Applications (Springer-Verlag, 2010)
44. T.S. Blyth, Set Theory and Abstract Algebra (Prentice Hall Press, 1975)

5 Calcium imaging in the living brain: prospects for molecular medicine

Background

In 2008 we were invited to write and review article about calcium imaging *in vivo* on the journal "Trends in Molecular Medicine". The purpose of this review was to introduce the methods of *in vivo* cellular-level calcium imaging to the general audience of medical researchers, and to explain why and how calcium imaging can be a useful method for medical studies. Note that, at that time, my research project was in the early stage of the two-photon calcium imaging of dendritic signals in electroporated cortical neurons *in vivo*. Due to their relevance, some of these preliminary experimental results were demonstrated in the review article as a panel of figure therein (Fig. 3d-e).

Review

Cell PRESS

Calcium imaging in the living brain: prospects for molecular medicine

Nathalie L. Rochefort, Hongbo Jia and Arthur Konnerth

Institute of Neuroscience, Technical University Munich, Biedersteiner Str. 29, 80802 Munich, Germany

Calcium imaging has revolutionized the approaches for functional analyses in the living brain of animal experimental models. Changes in intracellular calcium concentration are strictly linked to the electrical activity in neurons and produce signals that are effectively detected by optical methods. Distinctive features of fluorescence-based calcium imaging are its high temporal resolution in the millisecond range and its high spatial resolution in the micrometer range. Recent progress includes the development of fluorometric calcium sensors, new approaches for targeted labeling with these sensors and the implementation of powerful imaging techniques, especially two-photon microscopy. An important and rapidly evolving field of current research is the use of calcium imaging for the analysis of *in vivo* mouse models for various brain diseases, such as Alzheimer's disease, stroke and epilepsy.

Introduction

Imaging the brain at the cellular level provides essential information about its anatomy, function and pathology. Ever since the groundbreaking work of Golgi and Ramón y Cajal more than a century ago [1], many approaches have been developed for the labeling and visualization of nerve cells. Using specific labeling molecules in brain tissue, images can be obtained via illumination, magnetization, radiation or other physical processes. Changes in intracellular calcium ion concentrations $[Ca^{2+}]_i$, for example, have been extensively studied in brain tissue over the past two decades. Ca^{2+} is an intracellular messenger involved in many cellular functions, such as contraction, secretion, excitability and neuronal plasticity. Because calcium fluxes are tightly linked to neuronal electrical activity, recordings of intracellular free calcium dynamics are used to indirectly monitor the electrical activity of individual neurons.

By combining calcium indicators with appropriate optical imaging techniques, calcium fluxes can be monitored *in vitro*, in neuronal cultures or in brain slices, as well as *in vivo*, in the brain of animal models. In this review, we present recent technical developments in the fields of calcium indicators and *in vivo* optical imaging. These new technical advances make calcium imaging a powerful approach for functional studies of neuronal populations in the intact and diseased brain. We present some applications of calcium imaging for the *in vivo* study of neuronal populations with cellular resolution and of calcium signaling in dendritic compartments. Finally, we show that calcium imaging is an extremely valuable approach for the investigation of brain diseases in mouse models of neurodegenerative pathologies, seizures and stroke.

Corresponding author: Konnerth, A. (arthur.konnerth@lrz.tum.de).

The development of calcium indicators

The development of calcium indicators for fluorometric microscopy has opened up a wide field of research in calcium signaling. The fluorescent calcium indicators most commonly used for imaging are listed in Table 1. Originally, Roger Tsien and colleagues developed small synthetic molecules, such as fura-2 and fluo-3, which were rapidly adopted by many laboratories worldwide and which are still intensively used [2]. The introduction of fluorescent proteins, such as green fluorescent protein (GFP) [3], allowed the tagging of specific cell types or subcellular compartments at high resolution by non-invasive delivery techniques. Recently, genetically engineered fluorescent proteins have been combined with calcium-sensitive proteins to target calcium indicators directly in defined cell populations [4–6]. An advantage of genetically encoded calcium indicators compared to synthetic dyes is the possibility of performing long-term calcium imaging *in vivo*, not only at the cellular level but also in specific subcellular compartments [7]. Some genetically encoded calcium indicators contain a single fluorescent protein, whereas others have been engineered based on changes in fluorescence resonance energy transfer (FRET) efficiency between two different mutants of GFP [8,9], a technique that had previously been widely applied for the imaging of protein–protein interactions.

Techniques for *in vivo* imaging

Evidence for brain calcium signals was initially obtained from the *in vitro* analysis of either neuronal cell cultures or slices prepared from animal experimental models, mostly rodents [10,11]. The first *in vivo* calcium-imaging experiments were performed in insects and zebrafish (reviews [12,13]). By combining the injection of calcium dyes with confocal or charge-coupled device (CCD) camera imaging, various sensory systems have been investigated in the non-mammalian brain *in vivo*, such as the olfactory system of honeybee [14], *Drosophila* [15] and turtle [16], as well as the cricket auditory neuron [17]. The choice of *in vitro* and non-mammalian models has been mainly guided by the limited depth penetration of conventional imaging techniques. In the mammalian brain, light scattering prevents the use of wide-field and confocal microscopy for imaging cells of interest located deeper in the tissue.

1471-4914/$ – see front matter doi:10.1016/j.molmed.2008.07.005 Available online 12 August 2008

Table 1. Most commonly used fluorometric calcium indicators

Name of fluorophore	Examples of *in vivo* applications	Refs
Synthetic dyes		
Oregon Green BAPTA-1	Mouse neocortex (neuron somata)	[25,29,40,79]
	Mouse neocortex (neuron somata and dendrites)	[54,55,85,101]
	Rat cerebellar cortex	[37]
	Cat visual cortex	[34]
	Ferret visual cortex	[35]
Calcium Green-1, -2, -5N	Honeybee olfactory sytem	[14]
	Turtle olfactory bulb	[16]
	Zebrafish embryo	[102]
	Mouse olfactory bulb	[49]
Fura-2, -PE3[a]	Zebrafish spinal cord	[103]
	Mouse neocortex (neurons)	[40]
	Cricket auditory neuron	[17]
Indo-1	Mouse neocortex (neurons)	[40]
Fluo-4	Mouse neocortex (astrocytes)	[64,67,96]
Rhod-2	Mouse neocortex (astrocytes)	[66]
Genetically encoded sensors		
G-CaMP[b], -1.3, -1.6, -2	*Drosophila*	[104]
	Mouse cerebellum	[6,36]
Camgaroo -1, -2; Pericam	Mouse olfactory bulb	[105]
YC[c]-2, -3, -6.1 (FRET[d])	Mouse olfactory bulb	[105]
Troponin C (FRET[d])	Mouse neocortex (neuron somata and dendrites)	[9,56]

[a]Fura-PE3: fura-2-related ratiometric Ca^{2+} indicator dye [106].
[b]Fluorescent calcium indicator using the calcium-binding protein Calmodulin (see Ref. [6]).
[c]YC, Yellow Cameleon (review in [107]).
[d]Fluorescence resonance energy transfer between two different mutants of fluorescent proteins.

The implementation of two-photon laser scanning microscopy has proven to be a powerful tool in achieving cellular and subcellular resolution in the highly scattering mammalian brain *in vivo* (see reviews [18,19]). Initiated by Denk *et al.* [20] in 1990, two-photon microscopy has quickly become popular among neuroscientists, and it continuously undergoes technical developments. Its main advantage is that it provides a depth penetration of several hundred microns in intact tissue, enabling high-resolution functional imaging in living animals. Novel scanning and

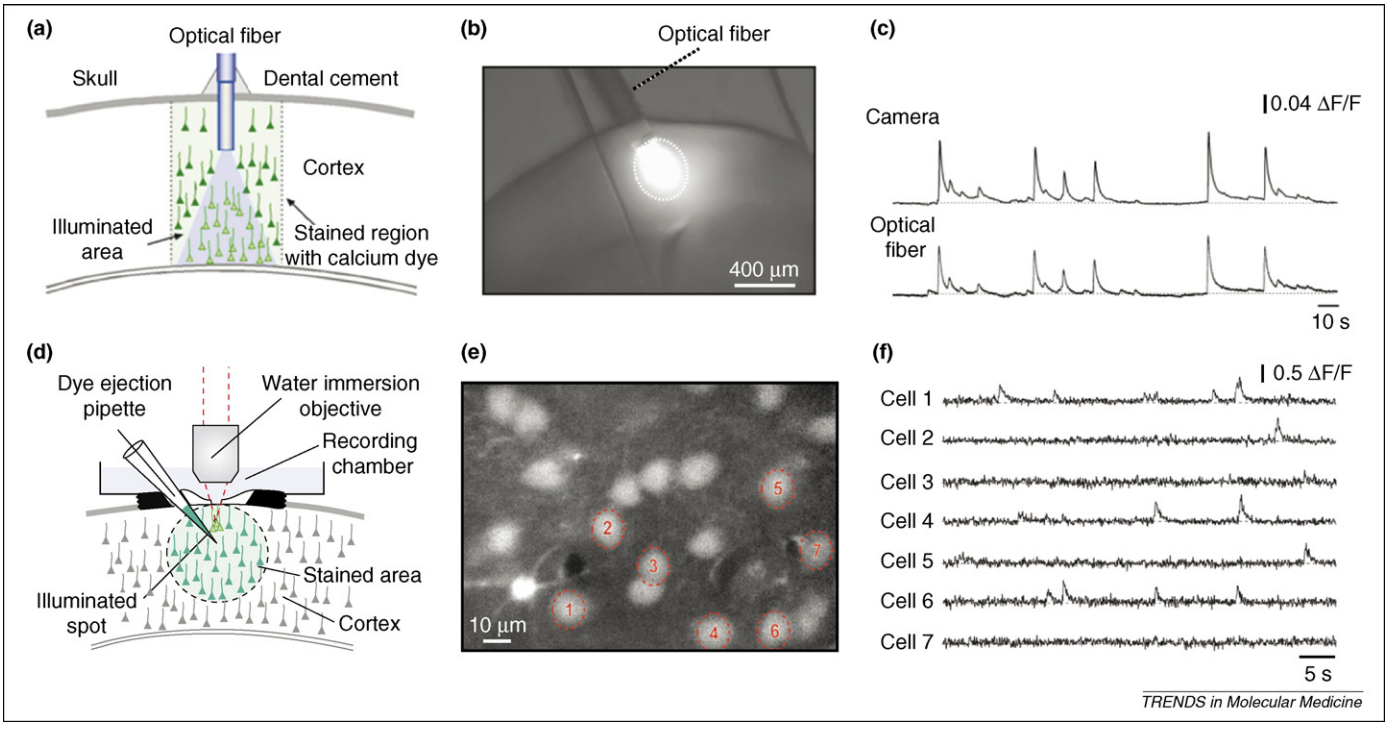

Figure 1. *In vivo* detection of neural calcium signals. **(a)** Experimental arrangement for fiber-optic-based calcium recordings. The optical fiber is used for both the excitation of the calcium indicator and the collection of the emitted light. **(b)** Excitation of calcium indicator with light delivered by an optical fiber in a mouse cortical slice. **(c)** Spontaneous calcium transients recorded simultaneously with a CCD camera and an optical fiber from the small cortical region, delimited by a dashed circle in panel (b). (Panels (a–c) reprinted by permission from Macmillan Publishers Ltd: *Nature Neuroscience*, adapted from Ref. [25] (courtesy of H. Adelsberger *et al.*), © Nature Publishing Group (2005)). **(d)** Schematic illustration of the targeted *in vivo* delivery of calcium dyes to the cortex. (Reprinted, with permission, from Ref. [40], © 1993–2008 by The National Academy of Sciences of the USA.) **(e)** *In vivo* two-photon calcium-imaging experiment of layer 2/3 cortical neurons stained with the calcium indicator OGB-1. **(f)** Spontaneously occurring calcium transients in the neurons marked in panel (e). (Panels (e) and (f) reprinted by permission from Macmillan Publishers Ltd: *Nature Protocols*, from Ref. [29] (courtesy of O. Garaschuk *et al.*), © 2006.).

acquisition techniques are being developed for fast time-resolved imaging covering large fields of view and in the 3D space [21–23]. The most commonly used stage-mounted microscopes for *in vivo* studies require the head of the animal to be fixed to minimize motion artifacts. Until recently, all imaging studies were performed in head-fixed and anesthetized animals. But a new technique has been reported for two-photon fluorescence imaging with cellular resolution in awake, behaving head-fixed mice [24], allowing the study of brain functions in non-anesthetized animals. Another approach for monitoring brain functions in awake animals involves the use of fiber-optic-based micro-endoscopes (Figure 1a–c). Contrary to head-fixed set-ups, this latter approach permits imaging in freely moving animals. Such endoscopes can be used for signal detection in deep brain structures, but they have a restricted field of view and low spatial resolution [25]. However, this form of imaging has a high temporal resolution and reports a compound calcium signal resulting from the synchronous activity of small neuronal circuits. Such recordings can be performed in any brain region of anesthetized and non-anesthetized animals [25]. An important goal is the achievement of imaging with cellular resolution through such a microendoscope. One approach is based on the use of micro-electro-mechanical scanners (MEMS) coupled with gradient-index (GRIN) lenses on the optical fibers [26,27]. Another approach involves the use of a fiber bundle combined with conventional scanning devices [28]. To date, however, none of these fiber-optic-based microendoscopy systems have been able to achieve an optical image quality that is comparable to that of stage-mounted microscopes and conventional lenses. An improvement in fiber-optic-based imaging is strongly needed, given that imaging in freely moving animals is ultimately required in order to address many physiological questions in *in vivo* studies.

Imaging neuronal populations activity with cellular resolution

Imaging a neuronal population allows the simultaneous mapping of spontaneous and evoked responses of numerous cells, from which the function of neuronal circuits can be inferred. A simple and effective method called multi-cell bolus loading (MCBL) has been developed to deliver a calcium indicator to a large population of intact cortical neurons [18,29]. A concentrated solution of a membrane-permeable acetoxymethyl ester (AM)-form calcium dye, for example Oregon-Green 488 BAPTA-1 (OGB-1), is injected by a micropipette into the desired imaging area through a small skull opening (Figure 1d). After diffusing into the cells, the dye is hydrolyzed by intracellular esterases, making it membrane-impermeable and causing it to remain in the cell while the extracellular dye is washed out (Figure 1e). Calcium signals from multiple cells can then be imaged with two-photon microscopy (Figure 1f). This method allows the simultaneous recording of large clusters of neurons and has been successfully applied to the imaging of calcium signals during spontaneous [25] or evoked activity in various brain areas, including the olfactory bulb [30–32] (Figure 2a), the visual cortex [33–35] (Figure 2b), the cerebellum [36,37] (Figure 2c) and the somatosensory cortex [38–40] (Figure 2d,e). In the visual cortex of higher mammals, conventional *in vivo* optical imaging (optical imaging of intrinsic signals or with voltage-sensitive dyes) first demonstrated the existence of an orderly map of preferred stimulus orientations and the arrangement of orientation domains around 'orientation pinwheels' [41]. However, the technique lacked the spatial resolution to determine the response properties and arrangement of cells near pinwheel centers. Two-photon calcium imaging revealed with single-cell resolution the highly ordered microstructure of pinwheel centers in cat visual cortex [34] (Figure 2b).

The zebrafish is a particularly suitable model for the study of the development of sensory systems with *in vivo* calcium imaging because the larvae are transparent and develop rapidly. Two-photon imaging revealed that the development of retinal ganglion cell axon arbors in the optic tectum of zebrafish depends on an activity-based competition between neighboring axons [42]. In another study, two-photon imaging of tectal neurons loaded with a fluorescent calcium indicator indicated that soon after the dendritic outgrowth and synaptogenesis, most visual properties in the tectum were already established. The development of these properties did not require patterned visual experience [43]. Two-photon calcium imaging in the visual cortex, as well as in the olfactory bulb [31,44,45], of the zebrafish is thus a useful approach for the establishment of the functional topology of neuronal activity patterns and the analysis of the role of activity in circuit development and function.

One limitation of the multi-cell bolus loading method is that it results in a non-specific labeling of all cells, including all neuronal and glial cells in the stained region. This limitation can be partially overcome by using additional specific indicators in parallel. For example, calcium signaling has been studied in cortical astrocytes labeled with the fluorescent dye sulforhodamine 101 [46] and in GABAergic interneurons expressing enhanced GFP (EGFP) [47]. Another method of labeling a specific neuronal population is to inject into axon bundles a dextran-conjugated form of dye, which will then be anterogradely and retrogradely transported over hours or days [48]. This method has been fruitfully used in the olfactory bulb [49] and in the olivary-cerebellar system [50]. In a study combining *in vivo* calcium imaging and retrograde dye labeling [51], a high variability was revealed in odorant-receptor maps in the olfactory bulb of individual mice (an example of an odorant-receptor map is shown in Figure 2a). Interestingly, odorant-receptor-defined glomeruli exhibited different ligand spectra and far higher sensitivity *in vivo* than in the corresponding *in vitro* studies [49]. Finally, the problem of imaging specific cell types can be solved by using genetic targeting of fluorescent protein calcium sensors, because the source of the optical signal is specified by the targeting [6]. For example, transgenic mice expressing the fluorescent protein calcium indicator GCaMP2 were used to investigate presynaptic calcium signaling at cerebellar parallel fiber–Purkinje cell synapses *in vivo* [36]. An example of two-photon fluorescence imaging of parallel fiber calcium transients is shown in Figure 2c. Despite this progress in the use of genetically encoded

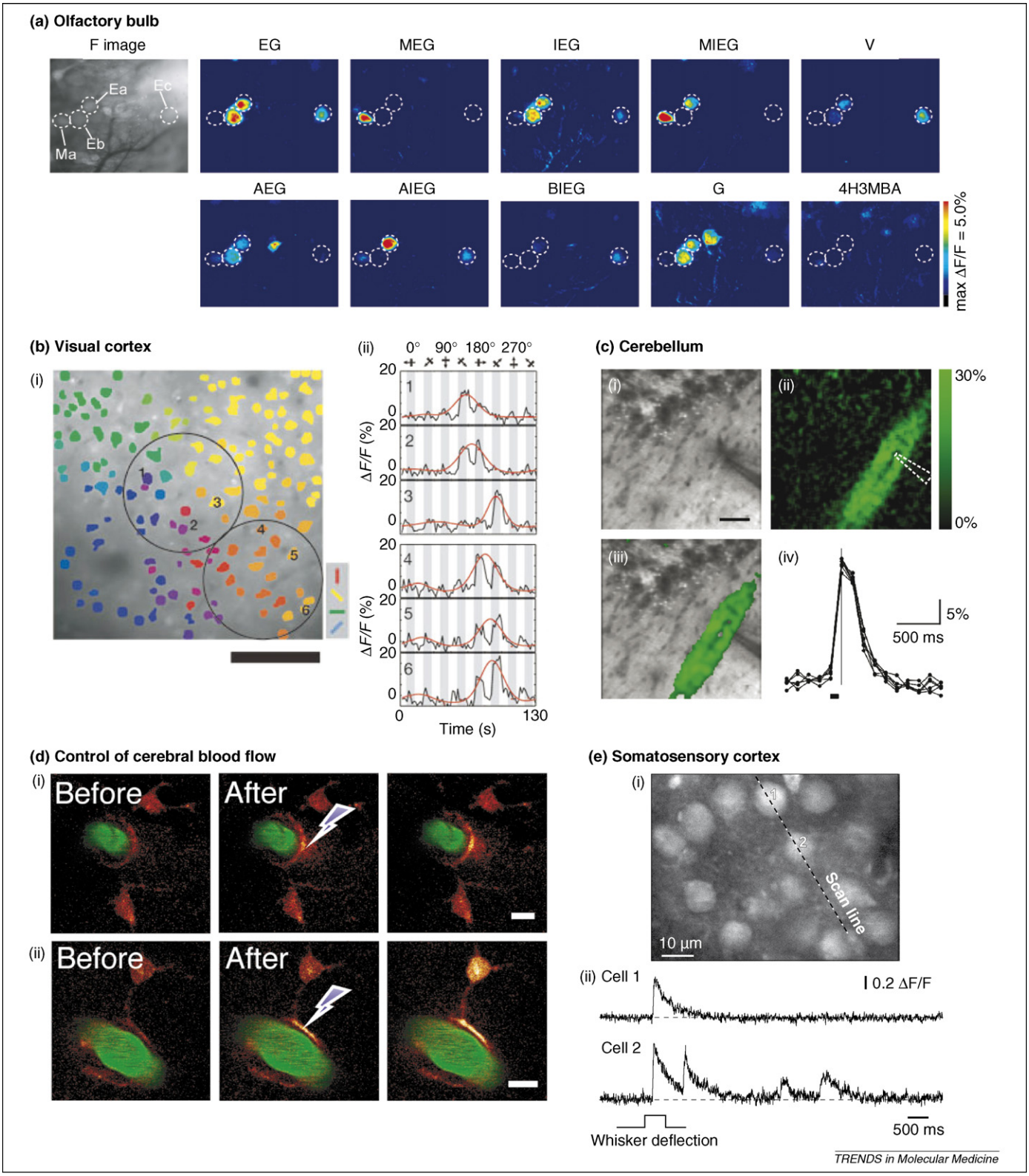

Figure 2. Examples of *in vivo* calcium imaging in different brain areas. **(a)** Calcium imaging of odorant-evoked responses in odorant-receptor-defined glomeruli (Ea, Eb, Ec and Ma) in the mouse olfactory bulb. 'F image' is the reference image of the brain's surface. The other images are pseudo-colored representations in which red corresponds to the largest odor-evoked response. The odorants used are indicated at the top of the images: eugenol (EG), methyl EG (MEG), isoeugenol (IEG), methyl IEG (MIEG), vanillin (V), acetyl EG (AEG), acetyl IEG (AIEG), benzyl IEG (BIEG), guaiacol (G), 4-hydroxy 3-methyl benzaldehyde (4H3MBA). (Reprinted from Ref. [49] (courtesy of K. Touhara), © 2006 Elsevier Inc., with permission of Elsevier.) **(b)** (i): Cell-based orientation map in the cat visual cortex obtained with two-photon calcium imaging. Scale bar represents 100 μm. (ii): Time course of the calcium signals evoked by visual stimulation in three selective cells (1–3) in the pinwheel centre and three selective cells (4–6) in the iso-orientation domain. Grey bars indicate periods of visual stimulation. (Reprinted by permission from Macmillan Publishers Ltd: *Nature*, adapted from Ref. [34], © 2006 Nature Publishing Group.) **(c)** Two-photon imaging of parallel fiber calcium transients in the cerebellum of a living GCaMP2 mouse. (i): Image of basal fluorescence, scale bar represents 50 μm. (ii): Fluorescence signal in response to electrical stimulation via the electrode (indicated as dashed line shape). Green color corresponds to the largest response (ΔF/F = 30%). (iii): Composite image of panels (i) and (ii) showing ΔF/F values. (iv): Time course of the fluorescence response (ΔF/F). (Reprinted from Ref. [36] (courtesy of T. Knöpfel), © 2007 Elsevier Inc., with permission of Elsevier.) **(d)** Astrocyte-mediated control of cerebral blood flow in the somatosensory cortex. (i): Two-photon images of a vascular astrocyte (labeled with calcium indicator rhod-2, red) showing calcium increases (yellow) restricted to the endfeet after photolysis of caged

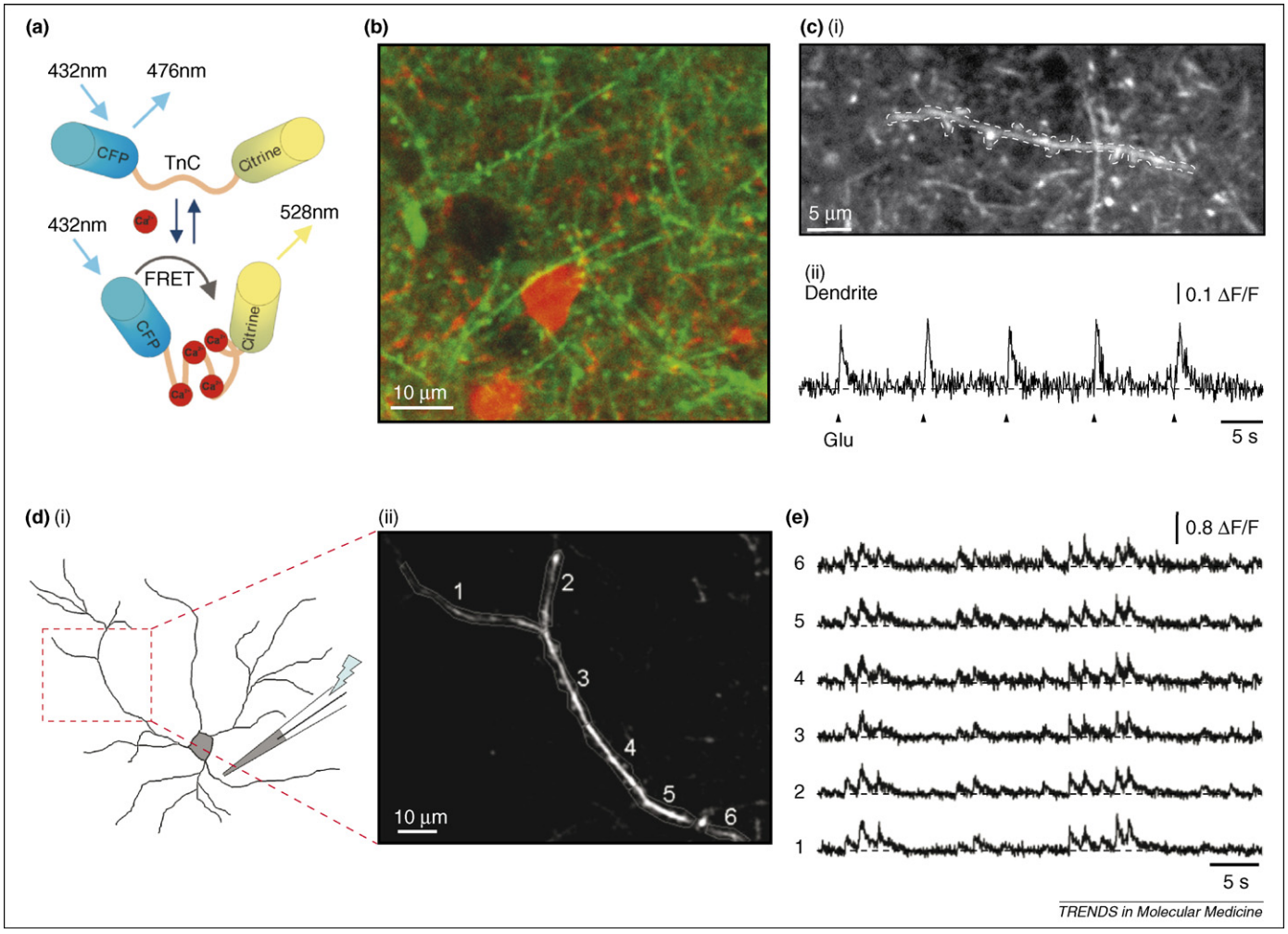

Figure 3. Calcium imaging of neuronal dendrites. **(a)** Schematic representation of the Troponin-C (TnC)-based fluorescence resonance energy transfer (FRET) calcium indicator CerTN-L15. This genetically encoded calcium indicator is based on changes in FRET efficiency between two different mutants of GFP [8,9]. Abbreviations: CFP, cyan fluorescent protein; Citrine, citrine-yellow fluorescent protein. **(b)** *In vivo* two-photon imaging of neuronal dendrites expressing the genetically encoded calcium indicator CerTN-L15 (green). Astrocytes were stained with the selective marker sulforhodamine 101 (red). **(c)** Imaging of a spiny dendrite (i) and FRET calcium signals evoked by local glutamate application (ii). (Panels (a) and (b) reprinted by permission from Macmillan Publishers Ltd: *Cell Calcium*, from Ref. [9], © Nature Publishing Group (2007). Panel (c) reprinted from Ref. [56], © Elsevier Ltd (2007), with permission of Elsevier.) **(d)** (i) Reconstruction of a cortical neuron labeled by *in vivo* electroporation with the calcium dye OGB1-hexapotassium salt. (ii) Imaging of a portion of dendrite indicated by the red square in (i). **(e)** *In vivo* two-photon imaging of spontaneous calcium signals in the dendritic segments indicated in panel (d).

calcium indicators, the results obtained *in vivo* in mice were much less impressive than those obtained in fly and fish (e.g. see Ref. [9]). New sensors [52] and, perhaps, other delivery methods, for example viral transfection, could soon lead to improved *in vivo* brain calcium imaging in mammals.

Calcium signaling in dendritic compartments

The bulk loading approach of calcium indicators (MCBL method) is well suited for the analysis of somatic activity in neural circuits. It has limitations when it comes to the imaging of subcellular compartments, such as dendrites, because the image contrast is reduced due to the staining of many fine processes in the surrounding neuropil. Furthermore, the dye concentration in MCBL-loaded cells is lower than in cells stained using a microelectrode [40,53]. These limitations also reduce the depth resolution of the recordings to 200–300 μm under the cortical surface as compared with a depth of more than 500 μm when imaging cell dendrites of microelectrode-loaded cells [53].

For the detection of calcium signals from dendrites and spines, alternative labeling methods have been used, such as dye delivery through patch-clamp pipettes [54,55], genetically encoded calcium indicators [56] (Figure 3a–c) and electroporation [57] (Figure 3d,e). These methods, combined with two-photon microscopy, provided the first images of dendritic signals *in vivo*. One application of this is, for example, the imaging of the propagation of somatic action potentials back into the dendritic tree in the living brain [54,55,58], a process that has previously been extensively studied in brain slices [59]. By using both calcium imaging and electrophysiological recordings, the relation-

(Figure 2 continued) calcium, at the position indicated by the arrow. The vasculature was stained with FITC-dextran (green). (ii): An astrocyte showing an increase in both endfoot and somatic calcium signals. Scale bar represents 10 μm. (Reprinted by permission from Macmillan Publishers Ltd: *Nature Neuroscience*, adapted from Ref. [66] (courtesy of T. Takano), © 2006 Nature Publishing Group.) **(e)** *In vivo* cortical recordings of calcium transients evoked by whisker deflection. (i): Image of layer 2/3 neurons in the mouse barrel cortex. (ii): Two-photon line-scan recordings of calcium transients evoked in two neurons by whisker deflection. (Reprinted, with permission, from Ref. [40], © 1993–2008 by The National Academy of Sciences of the USA.).

ship between dendritic calcium dynamics and electrical activities was characterized in the mouse brain *in vivo* [55]. However, until recently, single-action potential detection was unreliable with imaging approaches, although the estimation of action potential activity from calcium signals remains a key issue in the study of neuronal networks with calcium imaging [60,61]. It has recently been shown that it is possible to infer electrical activity with single-cell and single-action potential resolution from calcium transients measured in bulk-loaded neuronal populations [38,39,44] (see also Box 1 in [61]). Under favorable conditions, spike rates can be estimated from the fluorescence signal by a deconvolution-based method (e.g. see Ref. [44]).

Dendritic compartments represent key elements for synaptic signal integration [62], but their analysis poses major challenges. One difficulty is related to the fact that the orientation of the dendrites is mostly not within the usual horizontal XY imaging plane. This problem has recently been solved by the implementation of a novel approach that allows scanning in user-defined imaging planes [63]. Further improvements are needed to study the dendritic integration of sensory-evoked signals with a higher efficiency. For example, an important next step might be an approach that facilitates the identification of dendritic spines that are activated by sensory stimulation.

In vivo calcium imaging in disease models

For a long time, calcium imaging has been widely applied for the study of various neuronal diseases in animal models *in vitro*, mostly in cell cultures and in brain slices. In recent years, novel imaging techniques with cellular resolution have been increasingly used for the investigation of disease models *in vivo* with the goal of a detailed characterization of patho-physiological mechanisms. Because of depth-penetration limitations, optical imaging techniques are more suitable for studying pathological modifications in neuronal layers near the cortical surface (e.g. in the case of Alzheimer's disease) than in deeper brain regions (e.g. in the case of Parkinson's disease) and in the grey matter rather than in the white matter. Studies of impaired brain functions also greatly benefit from the development of a large array of genetic tools. A wide range of transgenic mice is now available, including models of neurological diseases and/or mice with specific cell types or cellular compartments labeled.

Two-photon calcium imaging is a powerful technique not only for studying neuronal activity but also for studying electrically non-excitable glial cells, for example astrocytes, *in vivo* [64]. Astrocytes are involved in many normal and pathological brain functions and represent a promising target for therapeutic treatments. Recent *in vivo* studies indicated that astrocytes show rapid increase in calcium upon sensory stimulation [35,65], have a role in regulating arterial blood flow [66] and are implicated in epilepsy [67,68], stroke and Alzheimer's disease [69]. Astrocytes can be readily labeled *in vivo* by the red fluorescent indicator sulforhodamine 101 [70], as well as by various transgenic labels [71]. In addition to the imaging of neuronal and glial activity, two-photon microscopy also offers the possibility to image the development of pathological protein aggregates, such as tangles and senile plaques in Alzheimer's disease, and to follow how they react to therapeutic treatments.

Alzheimer's disease, aging and degeneration

Alzheimer's disease is a degenerative and terminal disease for which there is currently no known cure. It is considered to be the most common cause of adult dementia. The cause and progression of Alzheimer's disease is not well understood but is associated with senile plaques [extracellular deposits of amyloid β (Aβ) peptide] and neurofibrillary tangles (intracellular accumulations of a hyperphosphorylated form of microtubule-associated tau protein) in the brain [72]. Several mouse models of Alzheimer's disease exist [73,74] in which Aβ plaques can be labeled *in vivo* via: (i) fluorescent dyes, such as thioflavin-S; (ii) fluorescently labeled antibodies against Aβ [75]; or (iii) intravenous (or even intraperitoneal) injection of a lipophilic Congo red derivative (Methoxy-X04) that can cross the blood–brain barrier and stain cerebrovascular as well as plaque-bound Aβ [76,77]. By imaging both plaques and neurons *in vivo* with two-photon microscopy, it is then possible to explore how Aβ plaques contribute to neuronal damage. One way is to perform morphological studies using transgenic mice with cells that are stained with fluorescent proteins. A recent longitudinal *in vivo* two-photon microscopy study showed the rapid appearance and local toxicity of Aβ plaques within only a few days, leading to increasingly dysmorphic neurites [77]. This fast timing was not expected because predictions were based on *in vitro* studies in which the appearance of Aβ aggregations was more protracted and followed a relatively slow nucleation-dependent polymerization process.

Glial cells are also believed to be strongly involved in the development of Alzheimer's disease pathology and can also be studied *in vivo*. For example, it was shown that one or two days after a new plaque's appearance, microglia are activated and recruited to the site [77]. Two-photon *in vivo* imaging of astrocytic calcium signaling in experimental mouse models of Alzheimer's disease revealed that abnormal astrocytic activity and instability in the microcirculation occurs in early stages of the disease preceding Aβ deposition and neuronal loss [69].

In such disease models, to study the impairment of local neuronal functions and their potential recovery after therapeutic treatments, functional recordings are required, either by electrophysiology [78] or by calcium imaging. Recently, it has been shown that calcium signals can be recorded from neurons around plaques in transgenic Alzheimer's disease mice [79]. The combination of the multi-cell bolus loading method and multicolor *in vivo* two-photon imaging allows the simultaneous studying of neurons, glial cells and senile plaques in the cortex of aged (up to two years old) mice [79] (see Figure 4a). The presence of lipofuscin and a lower imaging contrast make quantitative calcium measurements in aged tissue more difficult than in young mice, but recordings are still possible. In fact, *in vivo* calcium imaging in aged tissue is by far superior to any other type of registration because of the rapid degradation of this tissue under *in vitro* conditions.

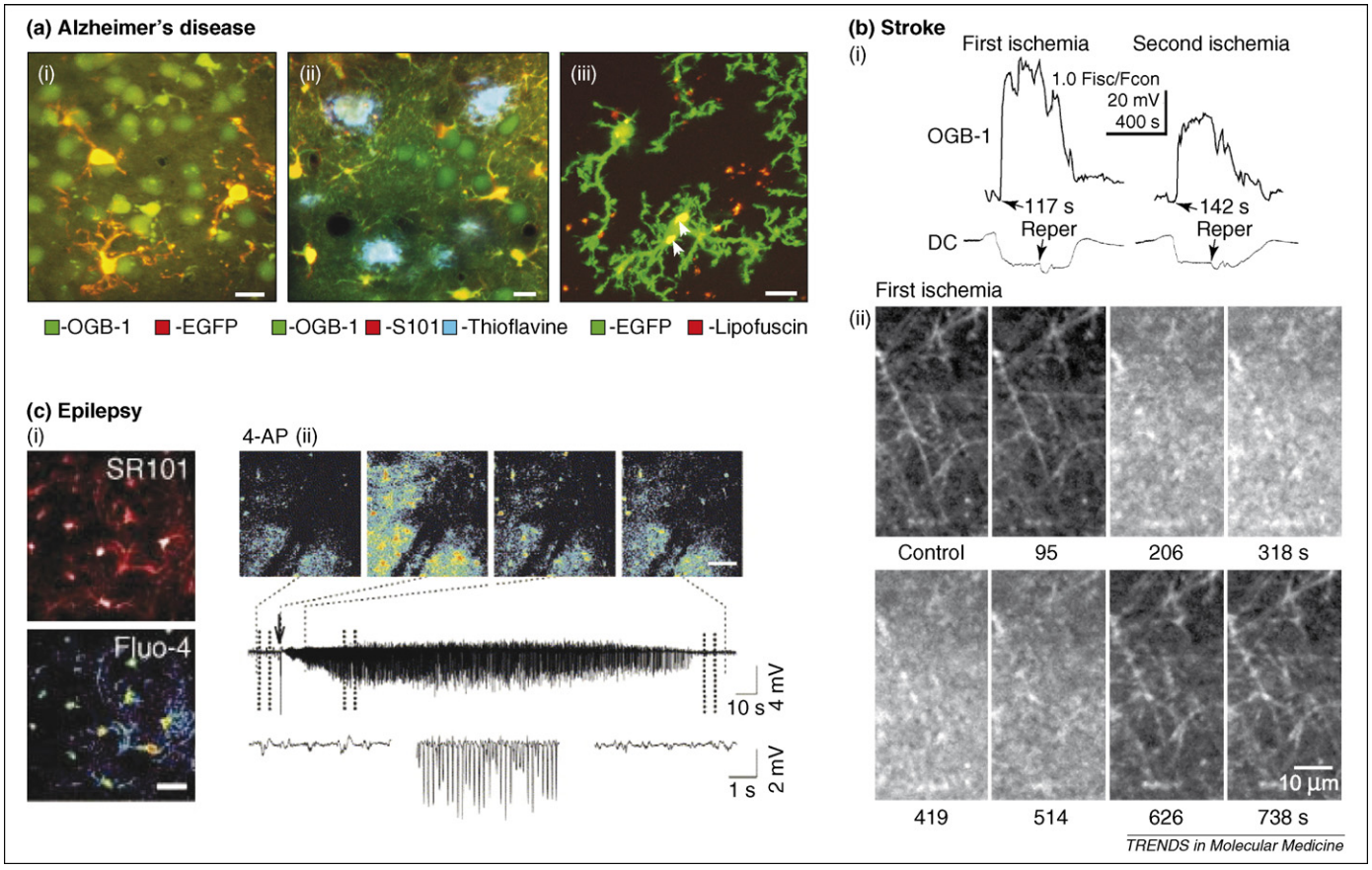

Figure 4. Examples of *in vivo* calcium imaging in brain disease models. **(a)** (i): *In vivo* two-photon imaging of neurons stained with OGB-1 (green) in the cortical layer 2/3 of a 15-month-old transgenic mouse expressing EGFP in microglial cells (red). (ii): Triple staining of cortical layer 2/3 cells with OGB-1 (green), thioflavine-S (Aβ plaques, cyan) and sulforhodamine 101 (astrocytes, red). (iii): Imaging of lipofuscin autofluorescence (red) in a transgenic mouse expressing EGFP in microglial cells (green). Note large lipofuscin deposits within the microglia cell body (arrowheads). Scale bars represent 10 μm. (Adapted from Ref. [79] (courtesy of O. Garaschuk *et al.*) with kind permission from Springer Science+Business Media, © Springer-Verlag 2007.) **(b)** Changes in intracellular calcium levels *in vivo* during transient ischemia coincide with slow electroencephalogram (DC EEG) activity and dendritic beading. (i): Change in normalized OGB-1 fluorescence taken from the neuropil in cortical layer I and cortical DC EEG recording of an animal subjected to bilateral common carotid artery ligation and reperfusion (Reper). (ii): GFP-labeled dendrites surrounded by diffuse OGB-1-labeled layer I neuropil from the same animal. At 206 s after ischemic onset, the layer I neuropil shows a large increase in OGB-1 fluorescence, indicating a sudden rise in intracellular calcium. The dendrites have become severely blebbed. At 2 min after reperfusion (514 s after ischemic onset), neuropil OGB-1 fluorescence levels are already beginning to decline, and 13 min (738 s) after ischemia the dendritic structure is nearly fully restored. (Adapted from Ref. [85] (courtesy of T.H. Murphy) with permission of © 2008 Society for Neuroscience.) **(c)** Experimental epileptic seizures in adult mice. (i): The primary somatosensory cortex was loaded with the astrocyte-specific dye sulforhodamine 101 (SR101) and the calcium indicator fluo-4 AM. Note that fluo-4 AM was preferentially taken up by astrocytes. Scale bar represents 25 μm. (ii): *In vivo* two-photon imaging showed abnormal calcium signaling (increase in fluo-4 emission in second image from left) preceding epileptiform discharges induced by the delivery of 4-aminopyridine (4-AP). The field potential recording showed an epileptiform event induced by 4-AP. Lower traces correspond to expanded recordings during the periods indicated by dotted lines. (Reprinted by permission from Macmillan Publishers Ltd: *Nature Medicine*, adapted from Ref. [67] (courtesy of G.F. Tian), ©2005 Nature Publishing Group.).

Amyotrophic lateral sclerosis (ALS) is another progressive neurodegenerative disease that could be studied by calcium imaging in a mouse model. The disease is characterized by a substantial loss of motor neurons in the spinal cord, brain stem and motor cortex. *In vivo* microscopy revealed early pathological changes of synaptic transmission in an ALS mouse model with transgenic yellow fluorescent protein expressed in all or subsets of motor neurons [80]. *In vitro* calcium imaging was performed in cultured spinal cord motor neurons of an ALS mouse model [81]. The implementation of two-photon calcium imaging *in vivo* is feasible and should decisively advance the investigation of the pathophysiological mechanisms underlying this disease.

Stroke, ischemia and hypoxia

Stroke is the rapid loss of brain functions in response to a cerebrovascular dysfunction. This dysfunction can be caused by either hemorrhage or ischemia (lack of blood supply) due to thrombosis or embolism. By using *in vivo* two-photon imaging, blood vessels can be visualized by intravenous injection of fluorescent dextran conjugates (Figure 2d) and blood flow can be measured by imaging the negative contrast of erythrocytes that exclude the dextran. Visualization of stimulus-induced changes in capillary flow was one of the first applications of two-photon microscopy *in vivo* [82]. Because ischemia can be easily induced in animals, this approach has subsequently been used to study animal models of ischemic stroke. By using GFP-expressing transgenic mice, it was observed that severe ischemia leads to rapid dendritic spine loss and alterations that could be substantially recovered if reperfusion occurred within 20–60 min [83]. The extent of the functional recovery after restoration of normal blood flow was studied with the same approach combined with optical imaging of intrinsic signals [84]. The mouse model

of ischemia has been further improved to alternate rapidly between the initiation of ischemia and reperfusion. Two-photon calcium imaging and optical imaging of intrinsic signals were used in this improved model to study functionally the initial reversible events associated with ischemia [85]. The new approach revealed that the apical dendritic structure of layer V neurons in the mouse somatosensory cortex was dramatically degraded by global ischemia. A key factor of this impairment was a propagating, spreading-depression-like ischemic depolarization that enveloped the cortex 2–3 min after ischemic onset and that occurred independently of ionotropic glutamate receptors [85]. Increases in intracellular calcium levels occurred during the wave of ischemic depolarization and were coincident with the loss of dendritic structure (see Figure 4b). After reperfusion, the dendritic structure, the intracellular calcium levels and the somatosensory functions largely recovered to the same status as before these brief periods of ischemia (6–8 min).

Spreading depression is a neural dysfunction that is often associated with migraine and with progressive neuronal injury after stroke and head trauma [86,87]. Two-photon calcium imaging showed that spreading depression was correlated with neuronal and astrocytic calcium waves and with the constriction of intracortical arterioles that could arrest capillary perfusion [86]. *In vivo* two-photon microscopy was used in a similar model of spreading depression to perform quantitative metabolic imaging. This was achieved by imaging, instead of calcium, the reduced form of nicotinamide adenine dinucleotide (NADH), a coenzyme found in all living cells. Intrinsic NADH tissue fluorescence served as a sensitive indicator of the cellular redox state *in vivo*. This study showed that spreading depression is associated with severe hypoxia and neuronal swelling [87].

The control of cerebral blood flow was also investigated in non-pathological conditions. The mechanism by which local electrical activity is translated into increases in blood flow remains poorly understood, although many *in vivo* functional imaging methods, such as functional magnetic resonance imaging (fMRI), are based on this coupling. The role of astrocytes in vasoregulation was studied *in vitro*, but conflicting results were obtained in different studies [88,89]. An *in vivo* approach was clearly needed to study regulation of cerebral blood flow because there is no blood circulation in brain slices. Two-photon *in vivo* calcium imaging in combination with local uncaging of caged calcium revealed a critical role of astrocytes in the control of local microcirculation (see Figure 2d) [66]. In addition, the relationship between neuronal activity and local cerebral blood flow was recently investigated in the rodent olfactory bulb [90].

Epilepsy

Epilepsy is a common neurological disorder that is characterized by recurrent seizures caused by bursts of synchronous, rhythmic neuronal hyperactivity. The problems of the initiation and propagation of the seizures as well as the injuries caused by these seizures on neuronal functions are still not entirely understood. The standard methods for monitoring epileptic activity – surface electrophysiological recordings or functional imaging techniques, such as fMRI and positron-emission tomography – generally lack either the spatial or temporal resolution to study seizure activity and neuronal impairments at the cellular level. The first *in vivo* studies used imaging of intrinsic optical signals to monitor neuronal activity during and after epileptic events [91]. After establishing the technique in an animal model (ferret), this approach was used to generate maps of epileptiform or physiological activity in the human cortex [92]. However, imaging of intrinsic optical signals does not allow analysis at the cellular level. Thus, two-photon imaging was used in models of epileptic seizures, first *in vitro*, in brain slices [93], and then *in vivo* in combination with the use of GFP-expressing transgenic mice [94]. With this approach, acute dendritic injury caused by kainate seizures could be studied *in vivo* [95].

Calcium imaging *in vivo* was used for the investigation of astrocytic activity during epileptic events. *In vivo* two-photon imaging showed that astrocytic calcium events were strongly correlated with the epileptogenic neuronal bursting activity induced by the administration of 4-aminopyridine (a potassium channel blocker that induces seizure activity in experimental models) [67,96] (see Figure 4c). Furthermore, anti-epileptic drugs, such as valproate, gabapentin and phenytoin, reduced both the amplitude of neuronal discharges and astrocytic calcium signaling induced by 4-aminopyridine [67]. These results suggest that epileptic discharges are secondary to the glial pathology and that astrocytes might represent a promising new target for treatments of epilepsy. *In vivo* two-photon calcium imaging can thus be an effective tool for the identification of unknown cellular elements involved in brain pathologies and can help reveal new therapeutic targets. A recent study introduced an *in vivo* model of developmental seizures within the intact unanesthetized brain of the transparent albino *Xenopus laevis* tadpole [97]. Pentylenetetrazol-induced seizures were characterized using *in vivo* two-photon calcium imaging of neuronal dynamics in this simple animal model preparation [97].

Conclusions

Calcium imaging in the living brain, especially two-photon imaging in the mouse brain, is increasingly being used for the analysis of various animal disease models. In particular, neurodegenerative-disease research benefits from *in vivo* investigations because many previous *in vitro* studies with nervous tissue from old animals did not provide satisfactory results. It is important to remember that even in healthy animals, good quality *in vitro* brain slices are mostly obtained at relatively early developmental stages. By contrast, *in vivo* two-photon calcium imaging experiments are feasible and produce good results in both young and aged mice (e.g. Ref [79]).

Although two-photon microscopy provides a better depth penetration than wide-field and confocal microscopy [19], *in vivo* two-photon imaging experiments are still mostly restricted to the exploration of superficial brain layers in the neocortex [18,39], cerebellum [36,37] and olfactory bulb [30–32] (Box 1). Recordings in deeper brain structures will require different technologies. New and promising approaches for microendoscopical recordings

Box 1. Outstanding questions that can be addressed with *in vivo* calcium imaging

- In the brain of Alzheimer's disease animal models, what are the functional changes of neuron activity in plaque-rich regions?
- How do neurons function in the aged brain? How do the functions of neural circuits change with age?
- How does neuronal plasticity underlying learning and memory change during the development of the brain?
- What is the function of genetically defined classes of neurons (e.g. parvalbumin-containing inhibitory neurons) in the normal and diseased (epileptic) brain?
- How do antiepileptic drugs affect the function of specific types of neurons (excitatory vs inhibitory) of the same cortical micro-circuit?
- How does the cell-specific genetic modification of neurons (e.g. that of Purkinje neurons in the cerebellum) affect the function of the neural circuit and cause disease (e.g. ataxia)?

are under way. These include single fiber volumetric recordings [25], fiber-bundle-based confocal imaging [98] and two-photon imaging using the GRIN lens technology [99,100]. With these new methods, the exploration of diseases, such as Parkinson's disease and Huntington's disease, that are caused by impairments in deeper brain areas will soon be possible in *in vivo* animal models.

Acknowledgements

Supported by the Deutsche Forschungsgemeinschaft (IRTG 1373) and the Schiedel Foundation. A.K. is a Carl-von-Linde Senior Fellow of the Institute for Advanced Study of the TUM.

References

1 Ramón y Cajal, S. (1909, 1911) *Histologie du Système Nerveux de l'Homme et des Vertébrés* (French edition reviewed and updated by the author, translated from Spanish by L. Azoulay), Maloine, Paris [published in English in 1995 as *Histology of the Nervous System of Man and Vertebrates* (translated by N. Swanson and L.W. Swanson), Oxford University Press]
2 Tsien, R.Y. (1989) Fluorescent probes of cell signaling. *Annu. Rev. Neurosci.* 12, 227–253
3 Tsien, R.Y. (1998) The green fluorescent protein. *Annu. Rev. Biochem.* 67, 509–544
4 Miyawaki, A. (2005) Innovations in the imaging of brain functions using fluorescent proteins. *Neuron* 48, 189–199
5 Mao, T. *et al.* (2008) Characterization and subcellular targeting of GCaMP-type genetically-encoded calcium indicators. *PLoS ONE* 3, e1796
6 Knopfel, T. *et al.* (2006) Optical probing of neuronal circuit dynamics: genetically encoded versus classical fluorescent sensors. *Trends Neurosci.* 29, 160–166
7 Kotlikoff, M.I. (2007) Genetically encoded Ca^{2+} indicators: using genetics and molecular design to understand complex physiology. *J. Physiol.* 578, 55–67
8 Shimozono, S. and Miyawaki, A. (2008) Engineering FRET constructs using CFP and YFP. *Methods Cell Biol.* 85, 381–393
9 Garaschuk, O. *et al.* (2007) Troponin C-based biosensors: a new family of genetically encoded indicators for *in vivo* calcium imaging in the nervous system. *Cell Calcium* 42, 351–361
10 Connor, J.A. (1986) Digital imaging of free calcium changes and of spatial gradients in growing processes in single, mammalian central nervous system cells. *Proc. Natl. Acad. Sci. U. S. A.* 83, 6179–6183
11 Tank, D.W. *et al.* (1988) Spatially resolved calcium dynamics of mammalian Purkinje cells in cerebellar slice. *Science* 242, 773–777
12 Egelhaaf, M. *et al.* (2002) Neural encoding of behaviourally relevant visual-motion information in the fly. *Trends Neurosci.* 25, 96–102
13 Helmchen, F. and Waters, J. (2002) Ca^{2+} imaging in the mammalian brain *in vivo*. *Eur. J. Pharmacol.* 447, 119–129
14 Galizia, C.G. *et al.* (1999) The glomerular code for odor representation is species specific in the honeybee *Apis mellifera*. *Nat. Neurosci.* 2, 473–478
15 Wang, Y. *et al.* (2001) Genetic manipulation of the odor-evoked distributed neural activity in the *Drosophila* mushroom body. *Neuron* 29, 267–276
16 Wachowiak, M. *et al.* (2002) Distributed and concentration-invariant spatial representations of odorants by receptor neuron input to the turtle olfactory bulb. *J. Neurophysiol.* 87, 1035–1045
17 Sobel, E.C. and Tank, D.W. (1994) *In vivo* Ca^{2+} dynamics in a cricket auditory neuron: an example of chemical computation. *Science* 263, 823–826
18 Garaschuk, O. *et al.* (2006) Optical monitoring of brain function *in vivo*: from neurons to networks. *Pflugers Arch.* 453, 385–396
19 Helmchen, F. and Denk, W. (2005) Deep tissue two-photon microscopy. *Nat. Methods* 2, 932–940
20 Denk, W. *et al.* (1990) Two-photon laser scanning fluorescence microscopy. *Science* 248, 73–76
21 Duemani Reddy, G. *et al.* (2008) Three-dimensional random access multiphoton microscopy for functional imaging of neuronal activity. *Nat. Neurosci.* 11, 713–720
22 Gobel, W. *et al.* (2007) Imaging cellular network dynamics in three dimensions using fast 3D laser scanning. *Nat. Methods* 4, 73–79
23 Salome, R. *et al.* (2006) Ultrafast random-access scanning in two-photon microscopy using acousto-optic deflectors. *J. Neurosci. Methods* 154, 161–174
24 Dombeck, D.A. *et al.* (2007) Imaging large-scale neural activity with cellular resolution in awake, mobile mice. *Neuron* 56, 43–57
25 Adelsberger, H. *et al.* (2005) Cortical calcium waves in resting newborn mice. *Nat. Neurosci.* 8, 988–990
26 Flusberg, B.A. *et al.* (2005) *In vivo* brain imaging using a portable 3.9 gram two-photon fluorescence microendoscope. *Opt. Lett.* 30, 2272–2274
27 Mehta, A.D. *et al.* (2004) Fiber optic *in vivo* imaging in the mammalian nervous system. *Curr. Opin. Neurobiol.* 14, 617–628
28 Gobel, W. *et al.* (2004) Miniaturized two-photon microscope based on a flexible coherent fiber bundle and a gradient-index lens objective. *Opt. Lett.* 29, 2521–2523
29 Garaschuk, O. *et al.* (2006) Targeted bulk-loading of fluorescent indicators for two-photon brain imaging *in vivo*. *Nat Protoc.* 1, 380–386
30 Tabor, R. *et al.* (2004) Processing of odor mixtures in the zebrafish olfactory bulb. *J. Neurosci.* 24, 6611–6620
31 Wachowiak, M. *et al.* (2004) Functional organization of sensory input to the olfactory bulb glomerulus analyzed by two-photon calcium imaging. *Proc. Natl. Acad. Sci. U. S. A.* 101, 9097–9102
32 Charpak, S. *et al.* (2001) Odor-evoked calcium signals in dendrites of rat mitral cells. *Proc. Natl. Acad. Sci. U. S. A.* 98, 1230–1234
33 Mrsic-Flogel, T.D. *et al.* (2007) Homeostatic regulation of eye-specific responses in visual cortex during ocular dominance plasticity. *Neuron* 54, 961–972
34 Ohki, K. *et al.* (2006) Highly ordered arrangement of single neurons in orientation pinwheels. *Nature* 442, 925–928
35 Schummers, J. *et al.* (2008) Tuned responses of astrocytes and their influence on hemodynamic signals in the visual cortex. *Science* 320, 1638–1643
36 Diez-Garcia, J. *et al.* (2007) *In vivo* calcium imaging from genetically specified target cells in mouse cerebellum. *Neuroimage* 34, 859–869
37 Sullivan, M.R. *et al.* (2005) *In vivo* calcium imaging of circuit activity in cerebellar cortex. *J. Neurophysiol.* 94, 1636–1644
38 Kerr, J.N. *et al.* (2007) Spatial organization of neuronal population responses in layer 2/3 of rat barrel cortex. *J. Neurosci.* 27, 13316–13328
39 Sato, T.R. *et al.* (2007) The functional microarchitecture of the mouse barrel cortex. *PLoS Biol.* 5, e189
40 Stosiek, C. *et al.* (2003) *In vivo* two-photon calcium imaging of neuronal networks. *Proc. Natl. Acad. Sci. U. S. A.* 100, 7319–7324
41 Bonhoeffer, T. and Grinvald, A. (1991) Iso-orientation domains in cat visual cortex are arranged in pinwheel-like patterns. *Nature* 353, 429–431
42 Hua, J.Y. *et al.* (2005) Regulation of axon growth *in vivo* by activity-based competition. *Nature* 434, 1022–1026

43 Niell, C.M. and Smith, S.J. (2005) Functional imaging reveals rapid development of visual response properties in the zebrafish tectum. *Neuron* 45, 941–951
44 Yaksi, E. and Friedrich, R.W. (2006) Reconstruction of firing rate changes across neuronal populations by temporally deconvolved Ca^{2+} imaging. *Nat. Methods* 3, 377–383
45 Yaksi, E. *et al.* (2007) Topological reorganization of odor representations in the olfactory bulb. *PLoS Biol.* 5, e178
46 Winship, I.R. *et al.* (2007) Rapid astrocyte calcium signals correlate with neuronal activity and onset of the hemodynamic response *in vivo*. *J. Neurosci.* 27, 6268–6272
47 Sohya, K. *et al.* (2007) GABAergic neurons are less selective to stimulus orientation than excitatory neurons in layer II/III of visual cortex, as revealed by *in vivo* functional Ca^{2+} imaging in transgenic mice. *J. Neurosci.* 27, 2145–2149
48 Hirase, H. *et al.* (2004) Two-photon imaging of brain pericytes *in vivo* using dextran-conjugated dyes. *Glia* 46, 95–100
49 Oka, Y. *et al.* (2006) Odorant receptor map in the mouse olfactory bulb: *in vivo* sensitivity and specificity of receptor-defined glomeruli. *Neuron* 52, 857–869
50 Kreitzer, A.C. *et al.* (2000) Monitoring presynaptic calcium dynamics in projection fibers by *in vivo* loading of a novel calcium indicator. *Neuron* 27, 25–32
51 Durand, G.M. *et al.* (2006) Quantitative single-cell RT-PCR and Ca^{2+} imaging in brain slices. *Pflugers Arch.* 451, 716–726
52 Mank, M. and Griesbeck, O. (2008) Genetically encoded calcium indicators. *Chem. Rev.* 108, 1550–1564
53 Svoboda, K. *et al.* (1997) *In vivo* dendritic calcium dynamics in neocortical pyramidal neurons. *Nature* 385, 161–165
54 Helmchen, F. *et al.* (1999) *In vivo* dendritic calcium dynamics in deep-layer cortical pyramidal neurons. *Nat. Neurosci.* 2, 989–996
55 Svoboda, K. *et al.* (1999) Spread of dendritic excitation in layer 2/3 pyramidal neurons in rat barrel cortex *in vivo*. *Nat. Neurosci.* 2, 65–73
56 Heim, N. *et al.* (2007) Improved calcium imaging in transgenic mice expressing a troponin C-based biosensor. *Nat. Methods* 4, 127–129
57 Nagayama, S. *et al.* (2007) *In vivo* simultaneous tracing and Ca^{2+} imaging of local neuronal circuits. *Neuron* 53, 789–803
58 Waters, J. and Helmchen, F. (2004) Boosting of action potential backpropagation by neocortical network activity *in vivo*. *J. Neurosci.* 24, 11127–11136
59 Stuart, G. *et al.* (1997) Action potential initiation and backpropagation in neurons of the mammalian CNS. *Trends Neurosci.* 20, 125–131
60 Gobel, W. and Helmchen, F. (2007) *In vivo* calcium imaging of neural network function. *Physiology (Bethesda)* 22, 358–365
61 Kerr, J.N. and Denk, W. (2008) Imaging *in vivo*: watching the brain in action. *Nat. Rev. Neurosci.* 9, 195–205
62 Eilers, J. and Konnerth, A. (1997) Dendritic signal integration. *Curr. Opin. Neurobiol.* 7, 385–390
63 Gobel, W. and Helmchen, F. (2007) New angles on neuronal dendrites *in vivo*. *J. Neurophysiol.* 98, 3770–3779
64 Hirase, H. *et al.* (2004) Calcium dynamics of cortical astrocytic networks *in vivo*. *PLoS Biol.* 2, e96
65 Wang, X. *et al.* (2006) Astrocytic Ca^{2+} signaling evoked by sensory stimulation *in vivo*. *Nat. Neurosci.* 9, 816–823
66 Takano, T. *et al.* (2006) Astrocyte-mediated control of cerebral blood flow. *Nat. Neurosci.* 9, 260–267
67 Tian, G.F. *et al.* (2005) An astrocytic basis of epilepsy. *Nat. Med.* 11, 973–981
68 Oberheim, N.A. *et al.* (2008) Loss of astrocytic domain organization in the epileptic brain. *J. Neurosci.* 28, 3264–3276
69 Takano, T. *et al.* (2007) Two-photon imaging of astrocytic Ca2+ signaling and the microvasculature in experimental mice models of Alzheimer's disease. *Ann. N. Y. Acad. Sci.* 1097, 40–50
70 Nimmerjahn, A. *et al.* (2004) Sulforhodamine 101 as a specific marker of astroglia in the neocortex *in vivo*. *Nat. Methods* 1, 31–37
71 Nolte, C. *et al.* (2001) GFAP promoter-controlled EGFP-expressing transgenic mice: a tool to visualize astrocytes and astrogliosis in living brain tissue. *Glia* 33, 72–86
72 Haass, C. and Selkoe, D.J. (2007) Soluble protein oligomers in neurodegeneration: lessons from the Alzheimer's amyloid β-peptide. *Nat. Rev. Mol. Cell Biol.* 8, 101–112
73 Oddo, S. *et al.* (2003) Triple-transgenic model of Alzheimer's disease with plaques and tangles: intracellular Aβ and synaptic dysfunction. *Neuron* 39, 409–421
74 Sturchler-Pierrat, C. and Sommer, B. (1999) Transgenic animals in Alzheimer's disease research. *Rev. Neurosci.* 10, 15–24
75 Backskai, B.J. *et al.* (2001) Imaging of amyloid-β deposits in brains of living mice permits direct observation of clearance of plaques with immunotherapy. *Nat. Med.* 7, 369–372
76 Klunk, W.E. *et al.* (2002) Imaging Aβ plaques in living transgenic mice with multiphoton microscopy and methoxy-X04, a systemically administered Congo red derivative. *J. Neuropathol. Exp. Neurol.* 61, 797–805
77 Meyer-Luehmann, M. *et al.* (2008) Rapid appearance and local toxicity of amyloid-β plaques in a mouse model of Alzheimer's disease. *Nature* 451, 720–724
78 Stern, E.A. *et al.* (2004) Cortical synaptic integration *in vivo* is disrupted by amyloid-β plaques. *J. Neurosci.* 24, 4535–4540
79 Eichhoff, G. *et al.* (2008) *In vivo* calcium imaging of the aging and diseased brain. *Eur. J. Nucl. Med. Mol. Imaging* 35 (Suppl. 1), S99–S106
80 Schaefer, A.M. *et al.* (2005) A compensatory subpopulation of motor neurons in a mouse model of amyotrophic lateral sclerosis. *J. Comp. Neurol.* 490, 209–219
81 Guatteo, E. *et al.* (2007) Altered calcium homeostasis in motor neurons following AMPA receptor but not voltage-dependent calcium channels' activation in a genetic model of amyotrophic lateral sclerosis. *Neurobiol. Dis.* 28, 90–100
82 Kleinfeld, D. *et al.* (1998) Fluctuations and stimulus-induced changes in blood flow observed in individual capillaries in layers 2 through 4 of rat neocortex. *Proc. Natl. Acad. Sci. U. S. A.* 95, 15741–15746
83 Zhang, S. *et al.* (2005) Rapid reversible changes in dendritic spine structure *in vivo* gated by the degree of ischemia. *J. Neurosci.* 25, 5333–5338
84 Zhang, S. and Murphy, T.H. (2007) Imaging the impact of cortical microcirculation on synaptic structure and sensory-evoked hemodynamic responses *in vivo*. *PLoS Biol.* 5, e119
85 Murphy, T.H. *et al.* (2008) Two-photon imaging of stroke onset *in vivo* reveals that NMDA-receptor independent ischemic depolarization is the major cause of rapid reversible damage to dendrites and spines. *J. Neurosci.* 28, 1756–1772
86 Chuquet, J. *et al.* (2007) High-resolution *in vivo* imaging of the neurovascular unit during spreading depression. *J. Neurosci.* 27, 4036–4044
87 Takano, T. *et al.* (2007) Cortical spreading depression causes and coincides with tissue hypoxia. *Nat. Neurosci.* 10, 754–762
88 Mulligan, S.J. and MacVicar, B.A. (2004) Calcium transients in astrocyte endfeet cause cerebrovascular constrictions. *Nature* 431, 195–199
89 Zonta, M. *et al.* (2003) Neuron-to-astrocyte signaling is central to the dynamic control of brain microcirculation. *Nat. Neurosci.* 6, 43–50
90 Chaigneau, E. *et al.* (2007) The relationship between blood flow and neuronal activity in the rodent olfactory bulb. *J. Neurosci.* 27, 6452–6460
91 Schwartz, T.H. and Bonhoeffer, T. (2001) *In vivo* optical mapping of epileptic foci and surround inhibition in ferret cerebral cortex. *Nat. Med.* 7, 1063–1067
92 Haglund, M.M. and Hochman, D.W. (2004) Optical imaging of epileptiform activity in human neocortex. *Epilepsia* 45 (Suppl. 4), 43–47
93 Badea, T. *et al.* (2001) Calcium imaging of epileptiform events with single-cell resolution. *J. Neurobiol.* 48, 215–227
94 Mizrahi, A. *et al.* (2004) High-resolution *in vivo* imaging of hippocampal dendrites and spines. *J. Neurosci.* 24, 3147–3151
95 Zeng, L.H. *et al.* (2007) Kainate seizures cause acute dendritic injury and actin depolymerization *in vivo*. *J. Neurosci.* 27, 11604–11613
96 Tian, G.F. *et al.* (2006) Imaging of cortical astrocytes using 2-photon laser scanning microscopy in the intact mouse brain. *Adv. Drug Deliv. Rev.* 58, 773–787
97 Hewapathirane, D.S. *et al.* (2008) *In vivo* imaging of seizure activity in a novel developmental seizure model. *Exp. Neurol.* 211, 480–488

98 Davenne, M. *et al.* (2005) *In vivo* imaging of migrating neurons in the mammalian forebrain. *Chem. Senses* 30 (Suppl. 1), i115–i116
99 Murayama, M. *et al.* (2007) Fiberoptic system for recording dendritic calcium signals in layer 5 neocortical pyramidal cells in freely moving rats. *J. Neurophysiol.* 98, 1791–1805
100 Flusberg, B.A. *et al.* (2005) Fiber-optic fluorescence imaging. *Nat. Methods* 2, 941–950
101 Nevian, T. and Helmchen, F. (2007) Calcium indicator loading of neurons using single-cell electroporation. *Pflugers Arch.* 454, 675–688
102 Ashworth, R. *et al.* (2001) Buffering intracellular calcium disrupts motoneuron development in intact zebrafish embryos. *Brain Res. Dev. Brain Res.* 129, 169–179
103 Brustein, E. *et al.* (2003) *In vivo* monitoring of neuronal network activity in zebrafish by two-photon Ca^{2+} imaging. *Pflugers Arch.* 446, 766–773
104 Marella, S. *et al.* (2006) Imaging taste responses in the fly brain reveals a functional map of taste category and behavior. *Neuron* 49, 285–295
105 Hasan, M.T. *et al.* (2004) Functional fluorescent Ca^{2+} indicator proteins in transgenic mice under TET control. *PLoS Biol.* 2, e163
106 Vorndran, C. *et al.* (1995) New fluorescent calcium indicators designed for cytosolic retention or measuring calcium near membranes. *Biophys. J.* 69, 2112–2124
107 Palmer, A.E. and Tsien, R.Y. (2006) Measuring calcium signaling using genetically targetable fluorescent indicators. *Nat. Protoc.* 1, 1057–1065

6 Other activities: Custom built video-rate two-photon microscopy setup

The studies of sensory evoked dendritic input sites *in vivo* as shown in previous chapters 2-4 had employed the combined method of two-photon calcium imaging and whole-cell recording. While techniques of whole-cell recording have been since long well established (1), techniques of two-photon imaging still have great potentials to be explored. One important issue of two-photon microscopy is the laser scanning (2), i.e., the laser beam must be steered such that the trajectory of focus points covering the desired field within the optical focal plane. The scanning can involve either galvanic mirror or AOD-based scanners. In either case the focus point is driven simultaneously along two orthogonal axes. Typically, the driving along the horizontal axis is fast, while the driving along the vertical axis is slower and uniformly spreads the horizontal lines into a square frame.

In order to acquire an image with sufficient digital resolution, a minimum number of horizontal lines must be scanned; therefore the repetition rate of image is largely dependent on the repetition rate of horizontal lines. The most commonly used scanner in confocal and multi-photon imaging is the linear galvanometric mirror, which can rotate to angles linearly with the command voltage. The cycling frequency can typically achieve up to 1 kHz, which means 2 kHz repetition rate of horizontal scan lines, since one cycle consists of forward and backward lines and both can be used for image formation. This means that when using 400 lines for the acquisition of an image, the image repetition rate is maximally 5 frames/s. However, for the detection of biological signals it is often necessary to use higher sampling rates. For example, even the accurate imaging of the fine structure of dendrites *in vivo* may require significantly higher frame rates, because of the noise resulting from the heart beat-mediated pulsations of around 8 Hz (for mice). According to the Nyquist-Shannon sampling theorem (3), in order to be able to acquire information of this noise and numerically filter it, the imaging speed should be above two-fold of it, i.e., 16 frames/s for the case of imaging dendrites located near a pulsating blood vessel.

One solution for increasing the imaging frame rate is to replace the linear galvanometric mirror by a resonant mirror for the horizontal axis (4). The cycling frequency of resonant mirror is typically 8 kHz so the gain of frame rate is about 8-fold. For example as shown in chapter 2, a configuration of 400 lines x 30 frames/s were used for recording visually evoked hotspots in multiple (2-8) dendritic portions (10-80 µm length each) of single layer 2 neuron in mouse visual cortex. Furthermore, I have implemented a 12 kHz resonant scanner (typically configured at 512 lines x 40 frames/s) which was successfully used for imaging dendritic spines in cortical neurons of the vibrissal cortex *in vivo*, as having been shown in chapter 4.

Fig. 6.1 shows the basic scheme of two-photon imaging of the 12 kHz resonant scanner setup, whereas the earlier built setup equipped with 8 kHz resonant scanner had as similar design.

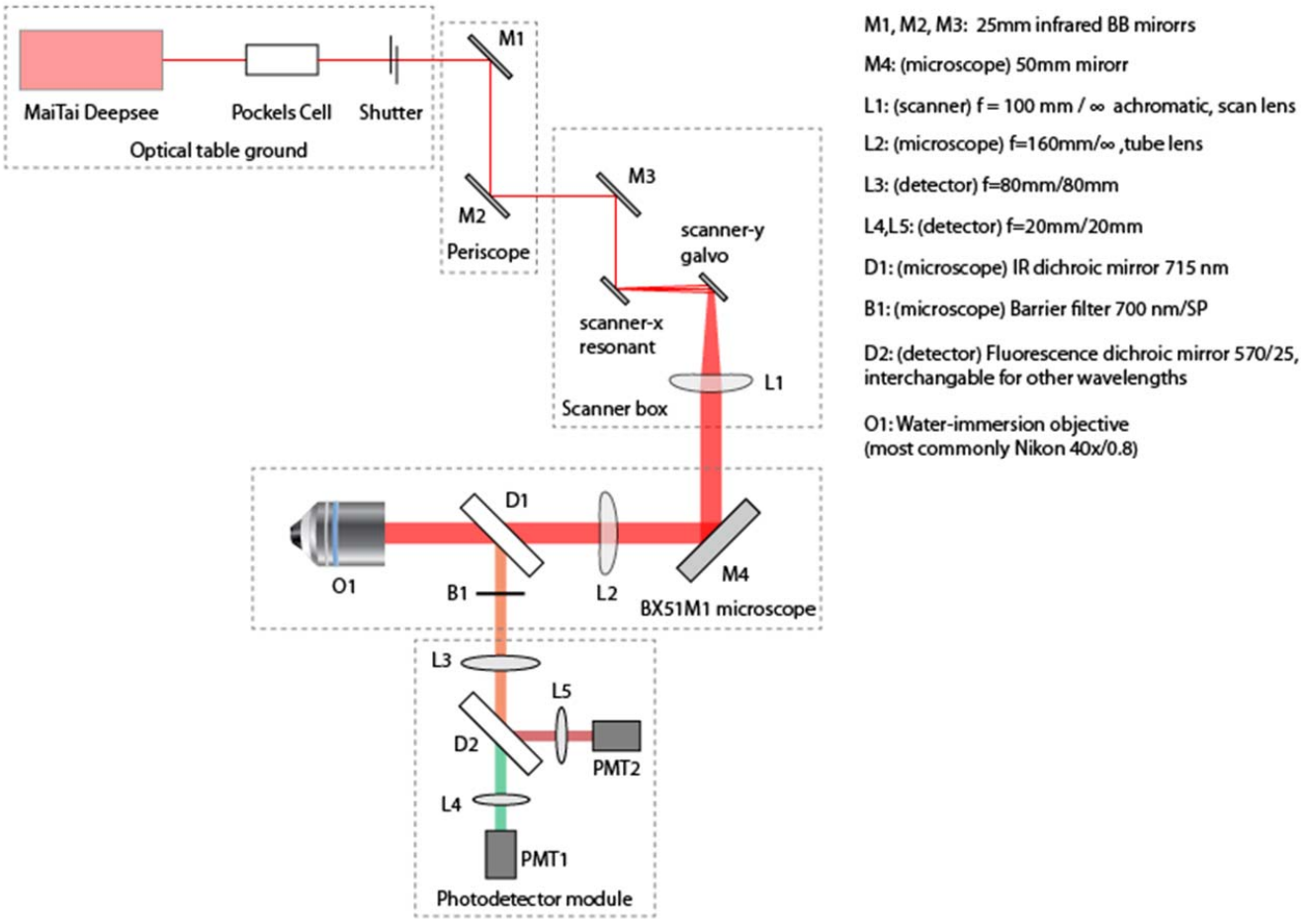

Fig. 6.1 Basic scheme of resonant-scanner based two-photon microscopy setup.

A unique feature of these setups is that they have a subsidiary system of intrinsic optical signal imaging, which allows mapping of cortical areas to sensory modules before the single-cell experiments and provides accurate coordinates for targeted patching in specific cortical area. Technical descriptions of this system have been illustrated in the “Text S1” part of chapter 4, and here I show the practical arrangements of the camera, lens, and illumination LEDs, as in Fig. 6.2.

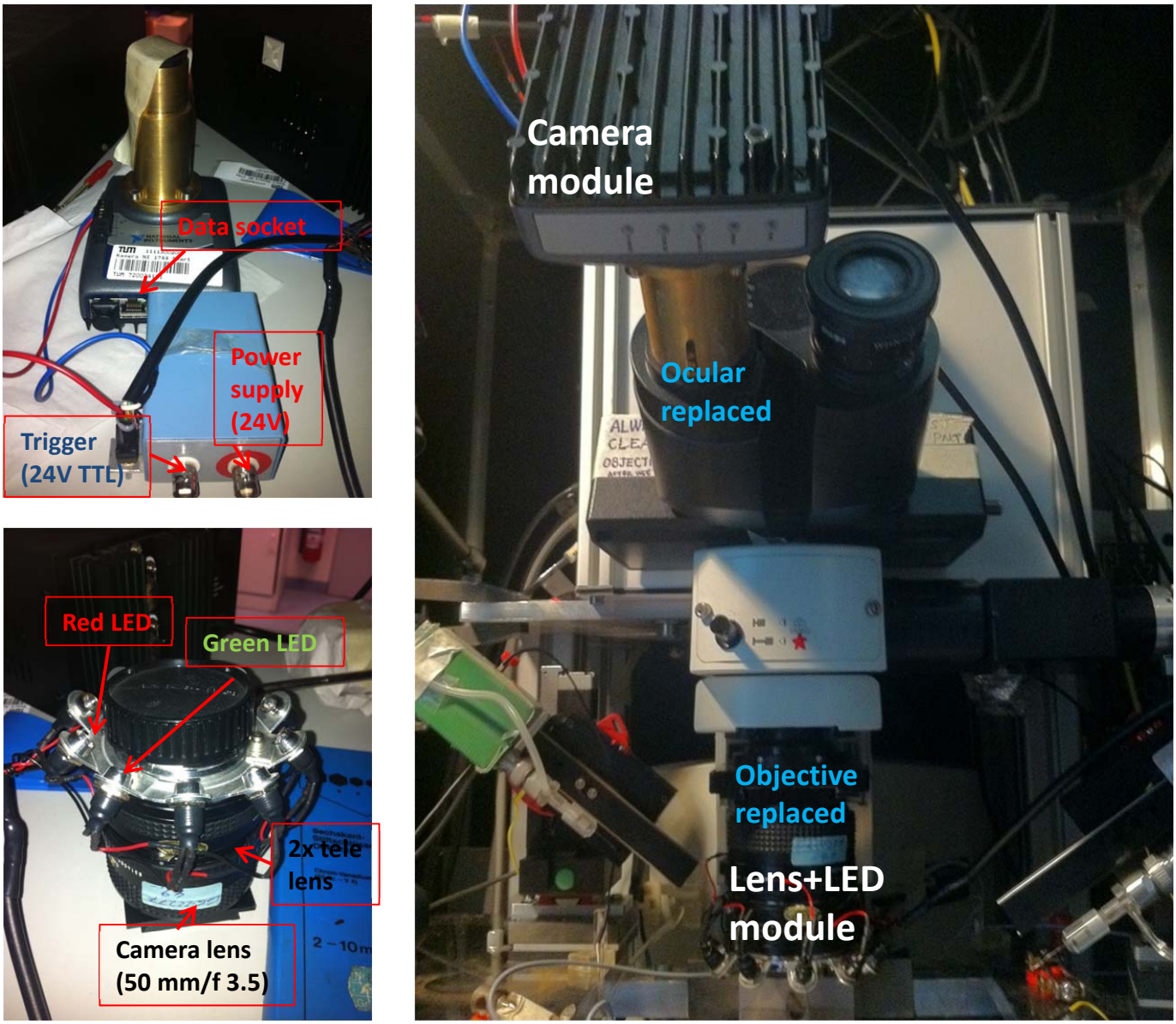

Fig. 6.2 Practical implementation of intrinsic optical signal imaging combined to two-photon microscopy setup

Overall, resonant scanner provides sufficient frame rate for imaging dendritic calcium signals of cortical neurons *in vivo*. Importantly, the practical design for two-photon imaging has been much simplified, thus allowing other subsidiary systems to be combined with, which are essential for various purposes of studies.

References

1. Sakmann B, Neher E (1995), *Single Channel Recording* (2nd ed, Plenum Press)
2. Denk W, Strickler JH, Webb WW. (1990) Two-photon laser scanning fluorescence microscopy, *Science* 248(4951):73-6.
3. Shannon CE (1949), Communication in the presence of noise, *Proc. Institute of Radio Engineers*, 37 (1) :10–21
4. Fan GY et al (1999), Video-rate scanning two-photon excitation fluorescence microscopy and ratio imaging with cameleons. *Biophys J.* 76(5):2412-20.

7 Summary and specification of contributions to published articles

The combination with whole-cell recording has enabled the identification of sensory stimulation activated dendritic input sites in cortical neurons *in vivo*, as demonstrated in chapter 2 and 3. Major findings in these studies include that, in layer 2/3 of mouse visual cortex, each neuron received multiple dendritic inputs that are tuned to various orientations; moreover, input sites with different orientation preferences were interspersed.

The further study in the barrel cortex by using such same experimental methods revealed a similar picture, that inputs of two whiskers were intermingled throughout the dendritic tree (chapter 4). Importantly, a single spine could be activated by both whiskers, i.e., "shared". Beyond the analysis of individual synaptic inputs, this study also provided additional important insights for both single neuron integration and network organization. First, the substantial proportion of recorded dendritic tree allowed the quantification of the integration of individual input signals for both whiskers. Therefore the relative ratio of summed input signal of surround whisker versus principal whisker could be calculated, which is significantly decreasing with respect to the distance of the surround whisker related barrel. Second, despite that most individual input sites were shared and activated at low probability, a simple classifier could still distinguish patterns of different whiskers at very high accuracy from trial to trial. This analysis together with a theoretical model suggested that the whisker identity information is reliably conveyed to each neuron by the ensemble of synaptic inputs, i.e., the pool of presynaptic neurons.

Taken together, the combined method of two-photon calcium imaging and whole-cell recording has led to new avenues to characterize functional connectivity of cortical neurons *in vivo*. Be advised, one shall clearly see as well the limitations of this method. One principle issue is that calcium imaging can only measure a fraction of excitatory synapses which allows calcium influx upon activation. Current technical limits of two-photon microscopy still restrict the distance, depth, and resolution of synapses that can be identified. Nevertheless, this method is of great potential to address many questions at unprecedentedly fine scales, allowing more comprehensive understandings of single neuron signaling as well as network functions *in vivo*.

Modern scientific research requires more and more teamwork, so as no exception for this one. As a concluding part of this thesis, I hereby clarify my personal contributions for the papers/manuscripts presented in previous chapters, in chronological order. Note that all the works were instructed and supervised by Prof. Dr. Arthur Konnerth (A.K.), whereas Prof. Dr. Bert Sakmann had conceived the project of barrel cortex and provided important suggestions throughout the progress. Contributions of other colleagues are individually specified in the following. Abbreviated names: Y.K. – Dr. Yury Kovalchuk; N.R. – Dr. Nathalie Rochefort; X.C. – Xiaowei Chen; Z.V. – Zsuzsanna Varga.

a. Construction of a two-photon imaging setup based on 8 kHz resonant scanner system. The initially building progress by Y.K. reached the stage of rough positioning of optical and electronic devices, and I adjusted them into working status together with software interfaces in LabVIEW and visual stimulation devices. This setup was used for the study on visual cortex (chapter 2 and 3).

b. Composing the Matlab codes for the visual stimulation program that can present drifting gratings in different size, speed, direction and timing. The program was supported by an open-accessed toolbox of Matlab named “Psychtoolbox” which was developed by a community of psychologists. N.R. and Y.K. provided specific user-demands for the functionalities.

c. Together with N.R., assisting A.K. to compose the manuscript of the review paper (chapter 5) which was invited by the journal “Trends in Molecular Medicine”.

d. Performing experiments of single-cell electroporation and two-photon calcium imaging of dendrites of layer 2/3 neurons of mouse visual cortex. One example data was published as a panel of figure in the review paper (chapter 5, Fig.3 d,e). These experiments were continuations of works of N.R. in which multiple neurons were electroporated.

e. Performing all the experiments of combined two-photon calcium imaging and whole-cell recording of layer 2/3 neurons of mouse visual cortex (chapter 2 and 3). X.C. was assisting with whole-cell recording for about 30% of the published experiments. During these co-performed experiments I have acquired the skills of in vivo whole-cell recordings. My other skills of animal

preparation and visual stimulation were previously learnt from Y.K. and N.R. in independent teaching sessions.

f. Devising the data analysis software and performing all the data analysis for the experiment data of visual cortex (chapter 2 and 3). N.R. was involved throughout the discussions on data analysis and manuscript writing with A.K. The same software was also used in an independent project by X.C. on the auditory cortex.

g. Building a new two-photon imaging setup from basic parts. This setup is based on 12 kHz resonant scanner and uses newly devised electronic controls and software. Importantly, this setup has a coaxial system for intrinsic optical imaging, which was essential to identify whisker related cortical barrels for the barrel cortex project (chapter 4).

h. Providing technical support during the experiments on the barrel cortex (chapter 4). The main experimental procedures were performed by Z.V.

i. Implementing new analysis algorithms for the barrel cortex project, including an advanced version of the previously used software for the visual cortex project, as well as the automated pattern recognition. The main analysis procedures were executed by Z.V.

j. Devised a theoretical model (chapter 4, section “text S2”) to interpret and extend the scope of experimental data on barrel cortex. Prof. Isarel Nelken and Z.V. provided critical comments and revisions.

k. Together with V.Z., assisting A.K. to compose the manuscript for the barrel cortex project.

l. Largely independently composed a chapter for the book “In vivo dendritic mapping of sensory inputs in cortical neurons” (editors Fritjof Helmchen and Bruno Weber, scheduled release by Springer-Verlag in 2011-2012). A.K. revised the manuscript.

Acknowledgements

I sincerely thank Prof. Dr. Arthur Konnerth for very responsible and productive instructions throughout my thesis work, and thank Prof. Dr. Bert Sakmann for great inspirations and suggestions on all projects. I also thank these colleagues, the help from whom specifically mentioned in the ending of the summary section: Dr. Yury Kovalchuk, Dr. Nathalie Rochefort, Xiaowei Chen, and especially Zsuzsanna Varga. Additionally, since a lot of my work was about constructing experiment setups, I must thank the technicians who made basic components: Dietmar Beyer, Felix Beyer, Werner Zeitz and Andreas Fohr. All other colleagues and friends are to be sincerely thanked as well, for the time working or talking together. Finally, all of these that I have achieved shall be shared with my beloved parents and grandparents, who had given and raised my body and brain.